Tropical Convection, Clouds, and Climate: Lessons from Idealized Models of Radiative-Convective Equilibrium

Adam Sokol

A dissertation
submitted in partial fulfillment of the
requirements for the degree of

Doctor of Philosophy

University of Washington

2024

Reading Committee:
Dennis L Hartmann, Chair
Robert Wood
Kyle Armour

Program Authorized to Offer Degree:
Department of Atmospheric Sciences

University of Washington

Abstract

Tropical Convection, Clouds, and Climate: Lessons from Idealized Models of Radiative-Convective Equilibrium

Adam Sokol

Chair of the Supervisory Committee:
Dennis L Hartmann
Department of Atmospheric Sciences

The Tropics are home to a wide variety of atmospheric phenomena that play major roles in global weather and climate. Tropical convection and its associated clouds are notoriously difficult to represent in global climate models, and as a result many cloud- and convection-related processes remain sources of great uncertainty in our understanding of climate and projections of future change. In this dissertation, I explore four distinct but interrelated research projects, each using a variety of tools to address critical questions related to tropical anvil clouds, convection, circulation, and climate. The overarching theme of this work is the extraction of robust insights from idealized models of radiative-convective equilibrium (RCE), a conceptual framework of great historical importance in the study of tropical climate and one that remains instrumental to our understanding of complex phenomena.

Chapter 1 provides background and motivation for my key research questions. In Chapter 2, I use an energy balance framework to study how surface warming affects the amount of cloud ice the tropical troposphere. In Chapter 3, I examine anvil cloud radiative feedbacks in high-resolution models and consider the implications for climate change. In Chapter 4, I investigate the congestus mode of tropical convection and explains its variability across cloud-resolving models. Finally, in Chapter 5, I examine the coupled variability of deep convection, atmospheric circulation, and sea surface temperature in an idealized simulation.

TABLE OF CONTENTS

Page

List of Figures iii

List of Tables x

Chapter 1: Introduction 1

Chapter 2: Energy balance constraints on the amount of cloud ice in the tropical upper troposphere 6

2.1 Introduction 6

2.2 Cloud-Resolving Model Simulations 8

2.3 An Analytical Model for Latent Heating 16

2.4 Application to Model Simulations 17

2.5 Summary and Discussion 25

2.6 Supplementary Information 27

Chapter 3: The anvil cloud response to warming in RCE and its implications for climate sensitivity 30

3.1 Introduction 30

3.2 Model Simulations and Satellite Data 32

3.3 Convective clouds as a continuum of ice 33

3.4 Ice cloud thinning in response to warming 37

3.5 A positive opacity feedback 40

3.6 Implications for climate sensitivity 45

3.7 Discussion 47

3.8 Supplementary Information 50

Chapter 4: Convective aggregation and the congestus mode of tropical convection 54

4.1 Introduction 54

4.2 Circulation variability in the RCEMIP CRM ensemble 58
4.3 Congestus invigoration in two-dimensional RCE 68
4.4 Why does static stability increase with aggregation? 76
4.5 Discussion 82
4.6 Supplementary Figures 85

Chapter 5: Internal variability in kilometer-scale simulations of coupled radiative-convective equilibrium 94
5.1 Introduction 94
5.2 Data and Methods 97
5.3 Description of the cycle of internal variability 100
5.4 Circulation throughout the cycle 109
5.5 Tropospheric stratification throughout the cycle 115
5.6 Sensitivity of the cycle to domain length 122
5.7 Sensitivity of the cycle to mean climate 126
5.8 Summary and Conclusion 129
5.9 Supplementary Information 131

LIST OF FIGURES

Figure Number Page

2.1 a) The forced cooling rate F applied in force300. b) Dashed red line: the radiative cooling rate Q_R in force300. Solid lines: the combined radiative and forced cooling rate Q_{R+F} in all three simulations. c) As in b, but as a function of temperature. Note that Q_R and Q_{R+F} are equal in con300 and con305. The radiative cooling rates are for all-sky conditions. 10

2.2 a) Tendencies of the liquid-ice static energy s due to (dashed lines) latent heating, (dotted) advection, and (solid) radiative and forced cooling Q_{R+F}. Tendencies are divided by C_p so that they have units K/day. The sum of the three tendencies is approximately equal to zero in equilibrium, since the diffusive tendency is small. b) Domain-averaged ice mass mixing ratio q_i. c) Latent heating efficiency of ice ϵ given by Eq. 2.3. 11

2.3 a) Cloud fraction, b) in-cloud ice mixing ratio, and c) domain-averaged ice mixing ratio as a function of temperature in the three simulations. d-f) fractional changes in each quantity with respect to con300. Note: model grid boxes are considered cloudy if the total condensate mixing ratio exceeds 10^{-5} kg kg^{-1} or 1% of the saturation vapor pressure of water, whichever is smaller. 13

2.4 a) Probability density functions (PDFs) of $\log_{10}$IWP for each simulation. b) Changes in the IWP PDF with respect to con300. 14

2.5 Profiles of each term in Eq. 2.10 for a) con305 and b) force300. The terms are normalized by C_p so that they are in K/day. Black lines show the total $\Delta\dot{s}_{ice}$ relative to con300, which is equal to the sum of the six individual terms and corresponds to the differences in the latent heating tendencies in Fig. 2.2a. 19

2.6 Contributions of (blue) non-q_i factors, (green) q_i, and (red) q_i' to changes in the latent heating efficiency ϵ relative to con300 in a) con305 and b) force300. Bold black lines show the total $\Delta\epsilon$, which is equal to the sum of the three colored lines and corresponds to the differences in the ϵ profiles in Fig. 2.2c . The dashed black line in (a) shows $\Delta\epsilon$ for a modified con305 scenario in which the q_i profile was shifted towards colder temperatures by 1 K. Non-q_i terms include ρ, Γ, V_m, and V_m'. 23

2.7 Latent heating efficiency ϵ in the upper troposphere in RCE simulations with different SSTs. 25

2.8 Schematic diagram illustrating this chapter's findings. The left side shows a cooler climate, and the right side shows changes that occur with warming. Dashed grey lines are isotherms. The radiative cooling and latent heating rates at a fixed temperature level both increase. As isotherms rise to higher altitudes and lower pressures, the lapse rate Γ and ambient density ρ decrease. Clouds contain a greater amount of ice, but the residence time of ice at any particular temperature shortens. Cloud fraction decreases. 26

2.9 Change in $\dot{s}_{ice}$ relative to con300 calculated using (solid lines) Eq. 2.9 and (dashed lines) the total differential approximation given by Eq. 2.10. 29

3.1 Mean ice cloud optical depth τ as a function of IWP in the three combined radar-lidar satellite retrievals. Bin widths are 0.1 for $\log_{10}$IWP. 32

3.2 The tropical ice cloud continuum. **(a)** f(IWP) derived from satellite observations of the tropical West Pacific (150-180°E, 15°S-15°N) for 2009. Three satellite retrievals and their mean are shown. **(b)** Multimodel mean CRE(IWP) for the CRM simulations with T_s=300 K. 34

3.3 Model representations of the ice cloud continuum. Panels show f(IWP) for each model and T_s. Dashed grey lines show the mean of the three satellite-derived estimates of f, scaled arbitrarily by a factor of 0.75 to aid comparison of distribution shapes. Vertical, dotted grey lines mark the cutoff between thick and thin clouds. 35

3.4 Cloud fraction composited by IWP for the simulations with T_s=300 K and the DARDAR v2.1.1 satellite retrieval (bootom right). Red lines show the mean cloud top height (CTH; shading is 10th-90th percentile). For the simulations, grid boxes are considered cloudy if the total condensate mixing ratio exceeds 10^{-5} kg/kg. CTH statistics do not extend all the way down to IWP=1 g/m^2 because such low IWPs can only result from ice mixing ratios below the cloudiness threshold. For the satellite retrieval, cloudy volumes are those with nonzero ice water content and visible extinction coefficients exceeding 0.125 km^{-1} [*Sokol and Hartmann*, 2020]. Data are for 150-180°E and 12°S-12°N for the 2009. 36

3.5 The ice cloud response to warming and its radiative effects. **(a)** fractional change in f(IWP), CRE(IWP) for T_s = 295 K, and $\Delta_f C$, the change in domain-averaged CRE due to changes in f alone. Lines show multimodel means and shading shows 25-75th percentiles. **(b)** Fractional change in f_{ice} and its decomposition into thick- and thin-cloud components. **(c)** $\Delta_f C_{\text{ice}}$, its thick- and thin-cloud components, and its area and opacity components. All values are normalized by ΔT_s. For box plots, boxes show Q1-Q3, dashes show medians, red triangles show means, and dots show individual models. 38

3.6 Correlation coefficients are shown for various quantities. Black: absolute changes in f(IWP) and f_{ice}. Green: fractional changes in f(IWP) and f_{ice}. Pink: $\Delta_f C$(IWP) and $\Delta_f C_{\text{ice}}$. 40

3.7 Decomposition of $\Delta C = \Delta(f \cdot CRE)$ into its three component terms (Eq. 3.3) 41

3.8 Δf_{ice}, Δf_{thick}, and Δf_{thin} versus $\Delta_f C_{\text{ice}}$ and its area- and opacity-related components. Correlation coefficients are marked with an asterisk if *not* statistically different from zero with 95% confidence. All values are normalized by ΔT_s. 45

3.9 Updating the probability density function of ECS. Grey: baseline WCRP feedback estimate of $N(-0.20, 0.20)$ W/m^2/K, where $N(x, y)$ is a Gaussian with mean x and standard deviation y. Pink: updated calculation using the RCEMIP-informed value of $N(0.03, 0.06)$ W/m^2/K. Above, the thin horizontal lines and boxes show 90% and 66% confidence intervals, respectively, and white dashes show the central estimate (median). 46

3.10 **(a)** Multimodel mean CRE computed three different ways, as described in the text. **(b)** Multimodel mean liquid cloud fraction as a function of IWP for the 300-K run. A column is determined to contain liquid cloud if the liquid water path exceeds 1 g/m^2. 51

4.1 CRH percentiles for the RCEMIP CRMs (RCE_large300 simulation). The CRH variance σ^2_{CRH} for each model is given in parentheses. 60

4.2 (**a**) Streamfunction Ψ, (**b**) relative humidity, and (**c**) radiative heating rate in moisture space for the RCEMIP CRMs. The black contours in (**b**) and (**c**) show Ψ and have a spacing of 1 g m^{-2} s^{-1} (the outermost contour is 1 g m^{-2} s^{-1}). Flow is counterclockwise around Ψ maxima. The orange contour in (**b**) indicates a cloud fraction of 0.1 using a cloud condensate threshold of 10^{-5} kg kg^{-1}. The hatching in (**c**) shows where the radiatively driven divergence D_{rad} exceeds 0.05 day^{-1}; hatching is only shown between 350 and 750 hPa. Note: While not visible, Ψ goes to zero at the highest CRH percentile. 62

4.3 Domain-averaged static stability s for each RCEMIP CRM. Dots indicate the freezing level for each run. 65
4.4 Selected profiles from the 2D SAM runs, with the color of each line corresponding to the degree of aggregation. (**a**) Temperature anomaly ΔT with respect to the control run, (**b**) static stability, (**c**) mean RH, (**d**) cloud fraction, (**e**) radiative cooling rate Q_{rad}, (f) radiatively driven divergence D_{rad}, (**g**) horizontal velocity v at the 50th CRH percentile, and (**h**) RH within 9 km of a convective updraft. With the exception of (**g**), all profiles are domain averages. 71
4.5 Streamfunctions for the 2D RCE ensemble, shown as the average of the streamfunctions from the 6-7 simulations falling within each σ^2_{CRH} tercile. **(a)** $\sigma^2_{\mathrm{CRH}} < 0.011$ **(b)** $0.011 < \sigma^2_{\mathrm{CRH}} < 0.028$ **(c)** $\sigma^2_{\mathrm{CRH}} > 0.028$ 72
4.6 Results from the prescribed radiation (PR) run. (**a**) Static stability, (**b**) radiative cooling rate Q_{rad}, (**c**) radiatively driven divergence D_{rad}, and (**d**) convergence of the in-cloud mass flux $-\partial_p \omega_{\mathrm{CLD}}$. All profiles are domain averages. Clouds are defined as grid boxes with a cloud condensate mixing ratio exceeding 10^{-5} kg/kg. 74
4.7 Difference between aggregated and unaggregated 2D runs in (**a**) differential radiative cooling and (**b**) three different static stability profiles. Yellow: domain-averaged stability; red: stability in grid boxes containing active convection; blue: stability of a undiluted moist adiabat computed as described in the text. 77
4.8 Stability and radiative cooling in a highly aggregated run (*u0 SSTa1 5xVT*). (**a**) Colored shading shows the instantaneous radiative heating rate. The black contour indicates static stability in excess of 0.075 K hPa^{-1} and the red contour relative humidity above 60%. (**b**) Blue shading shows the domain-averaged radiative heating rate over a ten-day period. Black contours indicate domain-averaged stability of 0.065 and 0.073 K/day. 81
4.9 Column relative humidity (CRH) distributions for each run in the 2D RCE ensemble. The color of each line corresponds to the degree of aggregation (red is high σ^2_{CRH}). 85
4.10 Hovmöller diagrams of column relative humidity for three of the simulations in the 2D ensemble. The three runs were chosen because they illustrate low, moderate, and high degrees of aggregation. Data are coarsened to 12-km horizontal and 6-hour time resolution before plotting. 86
4.11 Streamfunctions for each simulation the 2D RCE ensemble. The simulations are ordered by increasing σ^2_{CRH}, which is given in the top left corner of each plot. 87

4.12 Relative humidity as function of pressure and CRH percentile for each simulation in the 2D RCE ensemble. Black contours show the streamfunction Ψ reproduced from Fig. 4.11 and have a spacing of 1 g m^{-2} s^{-1} (the outermost contour is 1 g m^{-2} s^{-1}). 88

4.13 As in Fig. 4.12 but for the radiative heating rate. 89

4.14 As in Fig. 4.12 but for static stability. The color scale is intended to accentuate differences in stability in the mid-troposphere. The red contours enclose regions where the radiative cooling rate exceeds 2 K day^{-1}. 90

4.15 As in Fig. 4.12 but for cloud fraction. 91

4.16 As in Fig. 4.12 but for the radiatively driven divergence D_{rad}. D_{rad} is not shown within the boundary layer, where it is undefined due to near-zero stability. 92

4.17 Relationship between two measures of congestus strength in the 2D ensemble. v_{cong} is defined in section 2.2 and $-\partial_p \omega_{\text{CLD}}$ is the convergence of the in-cloud mass flux. $r^2 = 0.81$ excluding the prescribed radiation (PR) run. 93

5.1 (a) Mean (blue) precipitation and (red) 500-hPa vertical velocity sorted by SST percentile. SST percentiles are computed for each day of the simulation such that 0 and 1 represents the coldest and warmest SSTs on any given day, regardless of the domain-averaged SST. Bin widths: 0.05. (b) Correlation coefficients between the daily mean temperature at each model level and (black) SST_c and (dashed grey) $\overline{SST}$. 99

5.2 Time series of various quantities for a 2250-day period of the simulation. **(a)** various SST metrics; **(b)** net top-of-atmosphere downward radiation; **(c)** low cloud fraction; **(d)** the three leading terms of SST variance budget; **(e)** $\Delta_{cp}SST$, the metric developed in section 5.3.1 that quantifies the SST difference between the warmest and coldest parts of the cold, nonconvective region. For clarity, all time series except $\overline{SST}$ and $\Delta_{cp}SST$ are low-pass filtered using a 4th-order Butterworth filter with a 50-day cutoff. 101

5.3 Hovmöller diagrams of weekly mean (a) SST, (b) precipitation, and (c) albedo for a 1800-day period of the simulation. Data are coarsened to a horizontal resolution of 81 km for plotting. The black contour indicates a column relative humidity of 0.6 and is intended to loosely enclose regions of active convection. (d) Time series of $\overline{SST}$ and σ_{SST} reproduced from Figure 5.2a. 103

5.4 Characteristics of the (a,c,e) high-contrast cooling phase and (b,d,f) low-contrast warming phase. (a, b) Relative humidity. (c, d) Total nonprecipitating cloud condensate. Contours in (a-d) show the mass streamfunction with an interval of 4,000 kg m^{-1} s^{-1} (solid are positive; dashed are negative; zero contour not shown). (e,f) SST, albedo, precipitation, and the surface energy budget terms. Energy budget terms are expressed as anomalous fluxes with respect to the domain average, with positive values indicating downward energy flux into the surface. Data reflect the average of 2-hourly instantaneous output over 50-day periods within each phase of the cycle. 105

5.5 Profiles of (a) potential temperature, (b) vertical velocity, (c) the standard deviation of the vertical velocity, (d) RH, and (e) cloud fraction averaged over the (gold) relatively warm, cloud-free center and (purple) the cold, cloudy edges of the cold region. Profiles are computed from 3D output over a 50-day period during the high-contrast phase. 106

5.6 The three principal terms of the SST variance budget composited around the point in the cycle where $\overline{SST}$ reaches its **(a)** minimum and **(b)** maximum; i.e., $t = 0$ marks the end of the cooling phase in **(a)** and the end of the warming phase in **(b)**. The black lines show the composited time series of σ^2_{SST}. The composite represents the average of seven iterations of the cycle. 108

5.7 **(a)** the mean convective mass flux M and **(b)** its vertical gradient $\partial_p M$. **(c)** The first two EOFs of M and **(d)** their vertical gradient. The numbers in the EOF labels show the fraction of variance explained, and the horizontal dashed lines in (b) and (d) indicate the level of maximum $\partial_p M$. **(e)** Time series of the normalized anomalies of SST_c and σ_{SST}. **(f)** The first two principal components (PCs) corresponding to the EOFs shown in (c). 112

5.8 Vertical profiles comparing the (top) high-σ_{SST} and low-σ_{SST} phases and (bottom) high-SST_c and low-SST_c parts of the cycle. **(a,e)** clear-sky radiative cooling rate, **(b,f)** static stability, **(c,g)**, radiatively driven subsidence, and **(d,h)** convective mass flux. In (c), the dotted black line shows ω_r computed using Q_r from the low-σ_{SST} phase and s from the high-σ_{SST} phase; vice versa for the dashed black line. 113

5.9 **(a)** Shading shows monthly s anomalies. The grey line shows the freezing level. Normalized anomalies of SST_c (black) and σ_{SST} (green) are shown on a separate y-axis. **(b)** Correlation coefficients between monthly mean s and (black) SST_c and (green) σ_{SST}. **(c)** Difference in convective-region RH between the high- and low-contrast phases. **(d)** Black: difference in (solid) the domain mean stability $\Delta\overline{s}$ and (dashed) the convective-region stability Δs_c. Colored lines: difference in s predicted by the spectral plume model for various entrainment rates (expressed in km^{-1}.) and a LCL of 500 m. **(e)** difference in domain-averaged $(\partial_t S)_r$. Note the difference in y-axis limits between the top and bottom rows. 117

5.10 Vertical profiles of the correlation coefficient between monthly mean s and (black) SST_c, (green) σ_{SST}, and (purple) σ^2_{CRH}in ERA5. Data reflect the equatorial Pacific. Shading shows the 95% confidence interval generated from 10,000 bootstrapped samples. 121

5.11 Weekly average (a) $\overline{SST}$, (b) σ_{SST} and (c) $\Delta_{cp}SST$ for model runs with various domain lengths (L). The run with L =7,776 km is not shown in (c) because it does not have the cold edge-warm center SST pattern, so $\Delta_{cp}SST$ is undefined. Note that the beginning of the 2,000-day record shown in the figure corresponds not to the beginning of each simulation but to the beginning of the selected study period for each run. (d) Contrast in surface energy budget terms between the warm center and cold edges of the subsiding region; positive values act to increase the amplitude of the cold edge-warm center SST pattern and negative values act to dampen it. 124

5.12 $\overline{SST}$ (lines) for the sensitivity tests with different Q-fluxes. The blue line is the control run that is the primary subject of this chapter. Shading is between the 10th and 90th SST percentiles found across the domain. 127

5.13 Hovmöller diagrams of SST', the SST anomaly relative to the instantaneous domain average, for (a) the control run and (b) SST310, the warm, non-cycling run with Q=30 $\mathrm{W/m^2}$. The black contour shows CRH above 0.6 and is intended to loosely trace the parts of the domain with active convection. Note: domain-average SSTs vary with time and between the two panels, so the same SST' does not indicate the same absolute SST. 128

5.14 Overview of the cycle in $\overline{SST}$-σ_{SST} phase space. Each scatter point represents a 7-day period and is shaded according to the domain-averaged albedo anomaly. Low-contrast and high-contrast refer to the amount of SST variability across the domain. The circular arrow represents the direction in which the cycle progresses over time. 130

LIST OF TABLES

Table Number Page

3.1 Percentile values and other statistics (in $^{\circ}C$) for the posterior PDFs of ECS generated from different feedback values. Statistics are given for the original WCRP feedback estimate and for the RCEMIP-informed estimates, which use different values for the feedback uncertainty. 48

3.2 Table A3.1. Values of select quantities for the individual models in the RCEMIP CRM ensemble. All f values are unitless. All C values and $\overline{CRE}$ are in W/m^2. 52

3.3 Table A3.2. Values of select quantities for individual models. All values correspond to absolute changes between the 295- and 305-K simulations, normalized by ΔT_s. Δf values are in 1/K and all other values are in W/m^2/K. "Area" and "Opacity" refer to the area and opacity components of $\Delta_f C_{\text{ice}}$. "Global" refers to the global mean feedback, which is computed from $\Delta_f C_{\text{ice}}$ as described in the text. Note that Δf_{ice}, Δf_{thin} and Δf_{thick} shown here differ from the values shown in Fig. 3.5b, which are fractional changes. 53

4.1 Correlation coefficients for measures of convective aggregation (σ^2_{CRH}), congestus strength (v_{cong}), midlevel stability (s), and radiatively driven divergence (D_{rad}) across the RCEMIP CRM ensemble. 66

4.2 Model adjustments used in the 2D simulation ensemble 69

5.1 Details for the sensitivity tests of varying domain length L. SST and σ_{SST} represent averages over time (not including the equilibration period). 123

5.2 Details for the sensitivity tests with different mean climates achieved by changing the Q-flux. Results reflect the last 2,000 days of each run with the exception of the control run (Q=35 W/m^2), for which we use the same time period used for the rest of the chapter. 126

ACKNOWLEDGMENTS

I am grateful to my advisor, Dennis Hartmann, for his mentorship, his encouragement, and the intellectual freedom he gave me throughout graduate school, which fostered my interests and growth. Dennis' approach to science—in which physical understanding is paramount and cordiality is key—is one I deeply admire and strive to replicate. I feel incredibly lucky to have had the chance to learn from Dennis.

I want to thank the other members of my committee—Rob Wood, Kyle Armour, and Chris Bretherton—for their feedback and support, and for welcoming me into their group meetings over the years. Peter Blossey has also provided much support for this work, and I am grateful for his kindness, constant willingness to help, and expert modeling intuition.

I want to thank the many collaborators, mentors, and officemates who have enriched this work and my time in graduate school: Blaž Gasparini, Jacqueline Nugent, Sami Turbeville, Rachel Atlas, Chris Wright, Pedro Angulo-Umaña, Brittany Dygert, Aodhan Sweeney, Vince Cooper, Lily Zhang, Kat Huybers, David Battisti, Tom Ackerman, and Casey Wall. I am also grateful to my undergraduate advisor, Trude Storelvmo, whose early encouragement was an important part of my choice to pursue a PhD.

Countless other members of the UW Atmospheric Sciences community have been close friends and supporters. I cannot imagine a better environment in which to pursue a PhD.

Finally, I thank my parents, my sister, and my partner, Eva—none of this would be possible without their love and support.

Chapter 1
INTRODUCTION

In 2012, the World Climate Research Programme (WCRP) published a white paper titled *Clouds, Circulation, and Climate Sensitivity* [*Bony and Stevens*, 2012]. The topic had recently been designated one of seven "Grand Challenges" intended to inform the next decade of research in climate science. The white paper contended that clouds were largely to blame for the stubbornly large uncertainty in how Earth's climate would respond to rising greenhouse gas concentrations. A few years later, *Bony et al.* [2015] delineated four specific focus areas for the grand challenge, three of which dealt explicitly or very closely with tropical moist convection. Deep convection, in addition to being responsible for most of the precipitation that falls across the tropics [*Nesbitt et al.*, 2006], plays a critical role in many aspects of the global atmospheric circulation and climate. The transport of mass by deep convective updrafts forms the ascending branches of the Walker and Hadley circulations, two fundamental components of the atmospheric general circulation. Deep convection also excites vertically propagating gravity waves, which have myriad effects on the dynamics of the stratosphere [*Fritts and Alexander*, 2003]. And the clouds generated by convection affect local energy fluxes [*Ramanathan et al.*, 1989] as well as the large-scale atmospheric circulation [*Voigt et al.*, 2021]. With these impacts in mind, it is no surprise that tropical convection lay at the center of the WCRP grand challenge. Convection and its associated clouds are governed by processes occurring at much smaller scales than the typical size of a general circulation model (GCM) grid box. These processes must therefore be parameterized, and these parameterizations have served as a major source of uncertainty since the advent of numerical atmospheric modeling. Because uncertainty in convective processes can quickly cascade through the global climate system, a better understanding of convective processes

is critical for accurate predictions of future climate.

* * *

The research presented in this thesis is motivated by two outstanding questions about tropical convection and climate. The first deals with the expansive anvil clouds produced by tropical deep convection: What controls their area on climatological scales, and do changes in anvil act as a positive, negative, or neutral feedback on climate change? This question was first tackled by *Lindzen et al.* [2001], who proposed that increases in sea surface temperature (SST) would drive a large reduction in anvil cloud area and act as a strong negative feedback on warming. This so-called "Iris hypothesis" was flawed and controversial at the time of its publication [*Hartmann and Michelsen*, 2002; *Lin et al.*, 2002; *Chambers et al.*, 2002], but one central aspect of it seems to have held up over time: that the area covered by deep convection and anvil clouds decreases as the surface warms. This response is generally supported by observational, theoretical, and model-based evidence [*Ito and Masunaga*, 2022; *Zelinka and Hartmann*, 2010; *Bony et al.*, 2016; *Saint-Lu et al.*, 2020, 2022; *Choi et al.*, 2017; *Zelinka and Hartmann*, 2011]. Importantly, though, there is no evidence supporting Lindzen's originally proposed mechanism for this trend, which hypothesized that increases in the precipitation efficiency within deep convective towers would reduce the amount of ice detrained into the upper troposphere. More recent explanations for the decrease in cloud area typically rely on the fact that, in the Tropics, the convectively driven overturning circulations slows down as surface temperature increases [*Held and Soden*, 2006; *Zelinka and Hartmann*, 2010; *Bony et al.*, 2016].

Even if we knew exactly how anvil cloud area would respond to surface warming, determining the radiative feedback associated with such a change would still pose a challenge. Unlike most other cloud types, anvil clouds can have a positive, negative, or neutral cloud radiative effect (CRE) at different stages of their life cycle [*Hartmann and Berry*, 2017]. Deep convective towers and fresh, optically thick anvils have a CRE, while thinner, aged anvils have a positive CRE. In the present climate, the relative abundance of thick and thin

anvils and their respective CREs are such that the climatological CRE in regions of tropical convection is near zero [*Ramanathan et al.*, 1989; *Hartmann et al.*, 2001]. If a reduction in anvil cloud area were to affect thick and thin clouds in proportion to their present-day abundance, the radiative feedback would be neutral [*Pierrehumbert*, 1995]. But if the fractional changes in area vary, the radiative feedback could be positive or negative depending on whether thick or thin clouds are most affected [*Hartmann*, 2016]. Until now, we lacked an understanding of whether and why the thick and thin cloud responses may differ and, more broadly, how large the reduction in total anvil area may be. For these reasons, the anvil cloud area feedback was the least certain of all individual feedback processes considered in a recent WCRP assessment of equilibrium climate sensitivity [*Sherwood et al.*, 2020].

Chapters 2 and 3 of this dissertation address these important questions about tropical convection, anvil clouds and climate. In Chapter 2, I investigate how the amount of cloud ice in the tropical troposphere responds to changes in surface temperature. Using an energy balance approach, I find that the increase in cloud ice mixing ratio is not as large as the increase in radiative cooling or latent heating. This implies a reduction in the residence time of ice in the atmosphere, which is achieved via a decrease in density at any particular temperature level and a corresponding increase in ice fall speed.

In Chapter 3, I take a new approach to understanding the anvil cloud area and optical depth feedbacks. I examine the anvil response to warming using an approach that treats high clouds as part of an optical continuum rather than entities with fixed opacity. Applying this approach to an ensemble of cloud-resolving models, I find that they do not support a negative anvil cloud feedback. Rather, the models suggest that changes in cloud area and opacity together act as a weakly positive feedback. The positive opacity component arises from the disproportionate reduction in the area of thick, climate-cooling clouds relative to thin, climate-warming clouds. This result implies a +0.3 °C shift in the median estimate of equilibrium climate sensitivity relative to a previous community assessment.

* * *

The second motivating question of this work deals with the tropical overturning circulation and its interaction with the underlying SST. It is well known that the overall sensitivity of Earth's climate to CO_2 forcing depends on the spatial pattern of SST change [*Zhou et al.*, 2016; *Andrews et al.*, 2018]. Of particular importance is whether the zonal SST gradient across the equatorial Pacific increases, decreases, or remains the same in a warmer climate. Most general circulation models (GCMs) predict a strengthening of this gradient, that is, an El Niño-like response to warming [*Wills et al.*, 2022]. Such a response would be expected to produce a relative weakening of the Pacific Walker Circulation. On the other hand, observations over recent decades show a strengthening of the SST gradient and Walker circulation—a La Niña-like trend [*L'Heureux et al.*, 2013]. A La Niña-like response is more favorable for low cloud formation over the relatively cool SSTs in the eastern Pacific, and it is therefore associated with reduced climate sensitivity in models [*Zhou et al.*, 2016; *Dong et al.*, 2019]. Because the ocean and atmosphere in the equatorial Pacific are tightly coupled [*Bjerknes*, 1969], future changes in the Walker circulation could impact the zonal SST gradient across the Pacific and the trajectory of future climate change.

The rising branch of the Walker circulation in the western Pacific is driven by the upward transport of mass by deep convection. Changes in the spatial organization of convection and/or the mean vertical profile of convective mass flux have the potential to affect Walker strength and are therefore important for the global response to forcing. The static stability of the troposphere is an important factor for circulation strength and vertical structure [*Sohn et al.*, 2016]. It has long been known that tropospheric stability is sensitive to surface temperature and convective organization [*Knutson and Manabe*, 1995; *Held et al.*, 1993], but these sensitivities are not fully understood.

Chapters 4 and 5 of this dissertation focus on the vertical structure and internal variability of the tropical circulation using model configurations of various complexity. Chapter 4 examines the "forgotten" mode of tropical convection, referred to as the congestus mode. In an ensemble of cloud-resolving models, I find that the congestus mode is stronger in models that have a greater degree of large-scale convective aggregation. Aggregation invigorates

the congestus mode via a positive feedback involving moisture and radiative cooling. Chapter 5 examines the internal variability of a cloud-resolving model coupled to an interactive, mixed-layer ocean. When the mean SST is close to present-day tropical values, this system undergoes coherent, low-frequency oscillations in mean SST, SST contrast, and large-scale convective organization. This variability is described in full, and various aspects of the oscillations are discussed. Both chapters examine the modulation of tropospheric stability in idealized models of the tropical atmosphere. I find that upper-level stratification is modulated first and foremost by the SST, while mid-level stratification is more sensitive to changes in convective organization.

* * *

An overarching theme of this work is the extraction of robust insights from idealized models of radiative-convective equilibrium (RCE). RCE—one of the simplest models of Earth's atmosphere—describes the statistical equilibrium between radiative cooling and convective heating of the atmosphere. At large spatiotemporal scales, RCE is a good approximation of the tropical atmosphere [*Jakob et al.*, 2019]. RCE models of varying complexity have long been used as a test bed for understanding many atmospheric and climatic phenomena, such as the influence of CO_2 on surface temperature [e.g., *Manabe and Wetherald*, 1967], the effect of climate change on precipitation [e.g., *Romps*, 2011], and even the effects of nuclear winter on the thermal structure of the atmosphere [*Ramaswamy and Kiehl*, 1985]. More pertinently to this work, RCE has been used extensively to understand the SST dependence of convective cloud properties [e.g., *Harrop and Hartmann*, 2012; *Seidel and Yang*, 2022; *Seeley et al.*, 2019], convective organization [e.g., *Bretherton et al.*, 2005; *Wing et al.*, 2017], and the tropical overturning circulation [e.g., *Jenney et al.*, 2020; *Jeevanjee*, 2022]. By leveraging RCE to address the questions described above, I seek to build on this rich tradition.

Chapter 2

ENERGY BALANCE CONSTRAINTS ON THE AMOUNT OF CLOUD ICE IN THE TROPICAL UPPER TROPOSPHERE

This work was published as: Sokol, A. B. and D. L. Hartmann (2022). Radiative cooling, Latent Heating, and Cloud Ice in the Tropical Upper Troposphere. *Journal of Climate, 35*(5), 1643-1654. doi.org/10.1175/JCLI-D-21-0444.1.

2.1 Introduction

Ice clouds produced by tropical convection play an important role in Earth's climate yet remain a significant source of uncertainty in projections of climate change [*Bony et al.*, 2015; *Zelinka et al.*, 2017]. Changes in the properties and abundance of deep convective cores and their associated anvil clouds could have wide implications for the tropical radiation budget and global climate [*Zelinka et al.*, 2012; *Hartmann*, 2016]. Predicting these changes requires an understanding of complex dynamic, microphysical, and radiative processes that are difficult to observe and model. This complexity is evident in the Radiative-Convective Equilibrium Model Intercomparison Project (RCEMIP), in which different cloud-resolving models (CRMs) with nearly identical domains produce wildly different cloud climatologies and cloud responses to warming [*Wing et al.*, 2020]. While the radiative feedbacks associated with tropical convection remain difficult to constrain, recent work has advanced understanding of how warming may impact more specific aspects of convection, including its large-scale organization [e.g., *Coppin and Bony*, 2018], precipitation efficiency [e.g., *Lutsko and Cronin*, 2018], and anvil cloud evolution [e.g., *Gasparini et al.*, 2021]. In this chapter, we examine how warming may impact the mean profile of cloud ice amount.

The radiative-convective equilibrium (RCE) approximation provides a conceptual link

between the formation of ice and the atmospheric radiative cooling rate Q_R. The formation of ice during convection releases latent heat, which is transported to the upper troposphere (UT) by deep convective plumes. This latent heating, along with the eddy heat flux convergence associated with the convection, constitutes the total convective heating. In RCE, convective heating is balanced by Q_R, which we can compute accurately for known temperature and moisture profiles.

Models of varying complexity predict that Q_R in the UT will increase with warming if the temperature profile approximately follows a moist adiabat. This result is supported by prior work using early general circulation models [*Mitchell and Ingram*, 1992; *Knutson and Manabe*, 1995], simple spectral models [*Jeevanjee and Fueglistaler*, 2020], and modern line-by-line models [*Jeevanjee and Fueglistaler*, 2020]. *Jeevanjee and Romps* [2018] showed that the radiative flux divergence ($\mathrm{W/m^2/K}$ in temperature coordinates) at any particular temperature is unaffected by surface warming in simulations of RCE. But warming drives isotherms to lower pressures, where the ambient air is less dense. This produces an increase in Q_R (K/day), which is inversely related to density. *Hartmann et al.* [2022] used the cooling-to-space approximation to show that emission from the atmosphere is purely a function of temperature and relative humidity, but as the surface warms and the emission moves to a lower pressure, the transmission to space increases, which allows Q_R to increase. If the temperature profile follows a moist adiabat, Q_R preferentially increases at the anvil cloud level, causing the Q_R profile to become more top-heavy.

This chapter seeks to understand how the warming-driven increase in Q_R affects the mean profile of cloud ice amount in an RCE framework. Doing so requires us to examine the connection between radiative cooling, latent heating, and the ice mass mixing ratio q_i in the UT. In section 2.2, we describe a set of CRM simulations that allow us to examine how the atmosphere responds to an increase in Q_R with and without a corresponding change in surface temperature. This will show that the q_i response to warming is tempered by an increase in the efficiency by which ice imparts latent heat to the UT. To understand this change, we develop a mathematical expression for the ice-related latent heating rate and use

it to diagnose the CRM results (sections 2.3 and 2.4). This will show that the increased efficiency of latent heating is caused by the migration of isotherms to lower pressures and by the slight warming of the top of the convective layer. We discuss and contextualize these results in section 2.5.

2.2 Cloud-Resolving Model Simulations

We conduct RCE simulations using the System for Atmospheric Modeling [SAM; *Khairoutdinov and Randall*, 2003] with RRTM radiative transfer code [*Iacono et al.*, 2000; *Mlawer et al.*, 1997]. The model domain is 96 km $\times$ 96 km with 2-km horizontal resolution and periodic lateral boundaries. Because this small domain precludes convective aggregation, we can be confident that changes in the degree of aggregation do not impact our results. The vertical grid has 128 levels with variable spacing. The spacing is 50 m near the surface, smoothly increases to $\sim$300 m by 5 km, and increases again between 25 and 39 km to a maximum spacing of 1 km. Gravity waves are dampened by a sponge layer extending upward from 27 km. Sea surface temperature (SST) is fixed and uniform, there is no rotation, and insolation follows a fixed diurnal cycle corresponding to January 1 at the equator. We use the Predicted Particle Properties (P3) bulk microphysics scheme [*Morrison and Milbrandt*, 2015], which has a single ice-phase hydrometeor category with four prognosed variables: total ice mass, total ice number, rime mass, and rime volume. Because P3 has only one ice category, we do not differentiate between precipitating and nonprecipitating ice. We use the term "cloud ice" to refer to all ice-phase hydrometeors and the symbol q_i to denote the total ice mass mixing ratio.

Three simulations are conducted:

1. *con300*: 350-day control run with 300-K SST

2. *con305*: 350-day warming run with 305-K SST

3. *force300*: experimental run with 300-K SST and a forced cooling F intended to mimic

the upper tropospheric Q_R response to warming. This run is branched from con300 at day 150 and integrated for another 150 days. F is sinusoidal in pressure coordinates with positive (cooling) and negative (warming) lobes between 250-550 and 550-850 hPa, respectively, and a maximum amplitude of 0.26 K/day (Fig. 2.1a). Because of its sinusoidal structure, F has a mass integral of zero and thus no direct effect on the column-integrated cooling rate. We conducted an additional run in which F consisted only of its upper lobe, but there were no significant differences in the upper tropospheric quantities of interest.

The time-averaged results shown in the following sections reflect the last 75 days of each model run.

In equilibrium, the convective heating rate must balance the sum of Q_R and F, which we denote as Q_{R+F}. The solid lines in Fig. 2.1b-c show Q_{R+F} for each run. Because there is no forcing in con300 and con305, Q_{R+F} is just equal to Q_R in those runs and is larger in con305 for the reasons discussed in section 2.1. The increase in Q_R with warming is limited to temperatures above ∼220 K, since the Q_R profile is constrained to decrease at colder temperatures due to the scarcity of water vapor [*Hartmann and Larson*, 2002]. In force300, Q_R (dashed red line) is similar to that in con300, reflecting the fact that the two runs have equal SST and thus very similar temperature and moisture profiles. But because F is nonzero in force300, upper tropospheric Q_{R+F} is more like that in con305, especially when viewed in temperature coordinates (Fig. 2.1c). So while the temperature, moisture, and Q_R profiles in force300 match its 300-K SST, the total cooling "experienced" in the UT corresponds to a SST of 305 K. This is exactly the intent of the temperature forcing and will allow us to compare the atmosphere's response to increased Q_{R+F} in the presence and absence of SST warming. An implication of this approach is that F does not capture the warming-driven shift of the Q_R profile to lower pressures (Fig 2.1b).

The increase in upper tropospheric Q_{R+F} in con305 and force300 must be balanced by an increase in convective heating. We can examine the energy budget of the UT to better

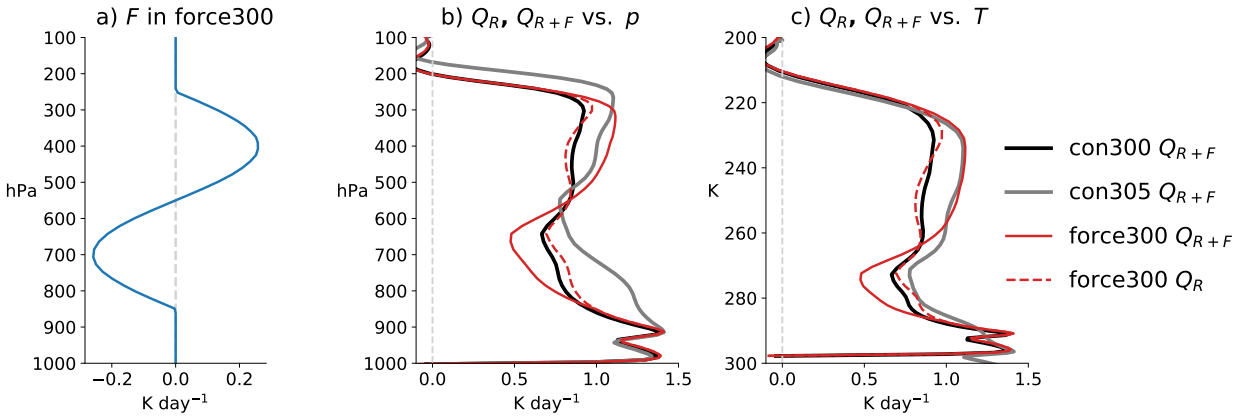

Figure 2.1: a) The forced cooling rate F applied in force300. b) Dashed red line: the radiative cooling rate Q_R in force300. Solid lines: the combined radiative and forced cooling rate Q_{R+F} in all three simulations. c) As in b, but as a function of temperature. Note that Q_R and Q_{R+F} are equal in con300 and con305. The radiative cooling rates are for all-sky conditions.

understand how this is achieved. The thermodynamic variable used for this budget analysis and throughout the rest of the chapter is the liquid-ice static energy:

$$s = c_p T + gz - Lq_l - L_s q_i. \tag{2.1}$$

C_p is the specific heat of dry air at constant pressure, T is temperature, g is the gravitational acceleration, q_l is the mass mixing ratio of all liquid condensate, and L and L_s are the latent heats of vaporization and sublimation, respectively. s is the prognostic thermodynamic variable in SAM and is exactly conserved by the model's governing equations. It is informative to use s for our analysis because it is approximately conserved during moist adiabatic processes and is therefore unaffected by phase changes.

Fig. 2.2a shows the model-computed tendencies of s due to Q_{R+F}, advection, and latent heating. These three tendencies, along with a very small diffusive tendency (not shown), form a closed energy budget. The advective tendency is negative because s increases with height, meaning that convective plumes deposit low-s air from the surface into the high-s

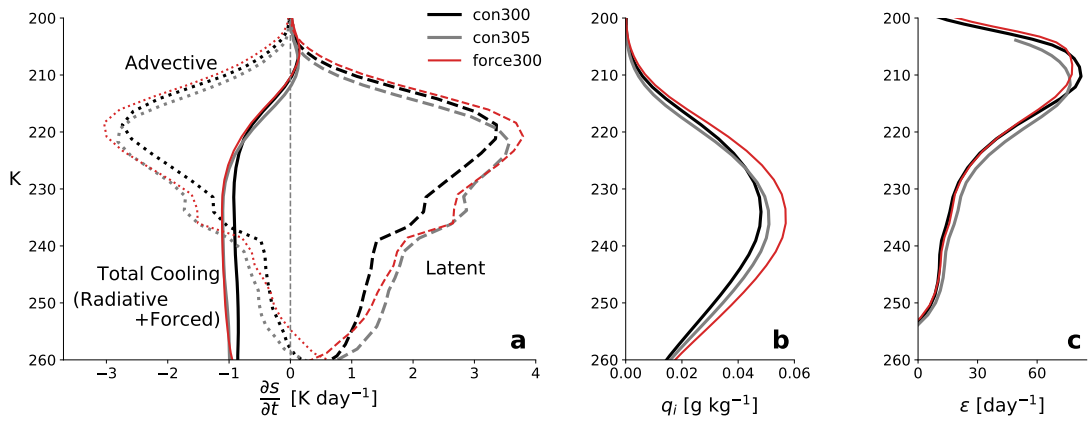

Figure 2.2: a) Tendencies of the liquid-ice static energy s due to (dashed lines) latent heating, (dotted) advection, and (solid) radiative and forced cooling Q_{R+F}. Tendencies are divided by C_p so that they have units K/day. The sum of the three tendencies is approximately equal to zero in equilibrium, since the diffusive tendency is small. b) Domain-averaged ice mass mixing ratio q_i. c) Latent heating efficiency of ice ϵ given by Eq. 2.3.

UT. Because there is no large-scale vertical motion in these runs, the advective tendency is comprised solely of the heating by resolved eddies. The convective heating rate is thus equal to the sum of the advective and latent heating tendencies.

Fig. 2.2a indicates that both the latent and advective components of the s budget strengthen in response to the increase in Q_{R+F} in con305 and force300. The increase in latent heating dominates, so the convective heating rate increases as a result. This increase in latent heating must be associated with changes in ice, since liquid condensate is scarce or nonexistent at temperatures below ∼245 K. To formally distinguish the ice-related latent heating from the total latent heating, we define $\dot{s}_{ice}$ as the latent heating tendency of s due to ice alone. To better conceptualize $\dot{s}_{ice}$, let us consider a saturated air parcel rising in a deep convective plume. Once the freezing level is surpassed, ice accumulates via freezing, vapor deposition, and/or new nucleation. This releases latent heat, which warms the parcel but does not change s, since s is conserved during phase changes. For as long as the ice remains with the parcel, there is the possibility that it sublimates and consumes the latent

heat released during its formation. But if the ice sediments out of the parcel, that latent heat is irreversibly left behind, and by Eq. 2.1, s increases because q_i has decreased. The important point here is that the latent heating of s results not from the formation of ice but from its irreversible sedimentation later on. This can be expressed mathematically as

$$\dot{s}_{ice} = -L_s \dot{q}_{i_{sed}} \tag{2.2}$$

where $\dot{q}_{i_{sed}}$ is the tendency of q_i due to sedimentation.

Because $\dot{s}_{ice}$ is determined by the net ice sedimentation rate rather than q_i itself, the relative differences in $\dot{s}_{ice}$ between the three simulations are not necessarily reflected in their domain-averaged q_i profiles. This is evident in Figure 2.2b. q_i is highest in force300 despite the fact that there is more latent heating in con305 over much of the same temperature range. In con305, the fractional increase in $\dot{s}_{ice}$ relative to con300 far exceeds that in q_i throughout most of the UT. In force300, while the fractional changes in $\dot{s}_{ice}$ and q_i are not exactly equal, they are much more similar. This difference is encapsulated by what we define as the latent heating efficiency:

$$\epsilon \equiv \frac{\dot{s}_{ice}}{L_s q_i}. \tag{2.3}$$

As ϵ increases, a smaller mean q_i is needed to achieve a given amount of latent heating. Fig. 2.2c shows profiles of ϵ for the three simulations. At air temperatures exceeding 215 K, ϵ is nearly the same in con300 and force300 but is larger in con305, suggesting that ϵ increases with SST. As will be shown later, additional simulations with SSTs of 295, 310, and 315 K support this trend.

Changes in the domain-averaged q_i can be caused both by changes in cloud fraction and by changes in the in-cloud ice amount. These two factors have important implications for both the top-of-atmosphere energy budget and atmospheric radiative heating rates, which have been shown to play an important role in the circulation response to warming [*Voigt et al.*, 2019]. In con305, ice cloud fraction is lower at any particular temperature than in con300 but the in-cloud q_i is higher on average (Fig. 2.3). The fractional increase in in-cloud

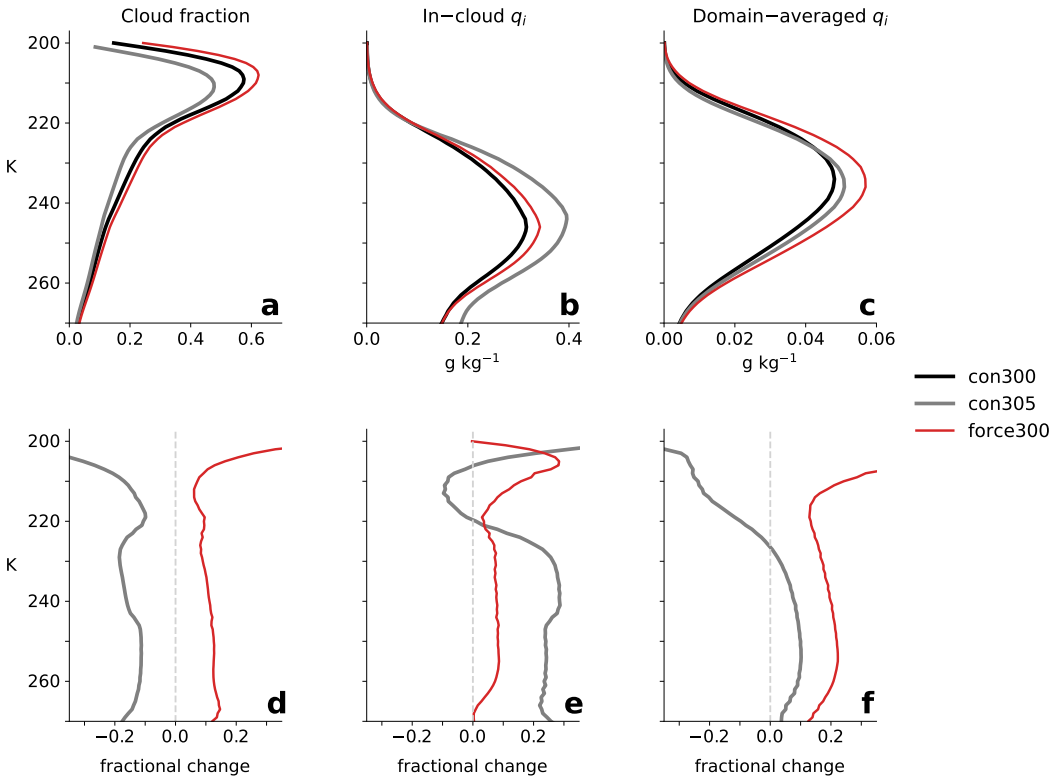

Figure 2.3: a) Cloud fraction, b) in-cloud ice mixing ratio, and c) domain-averaged ice mixing ratio as a function of temperature in the three simulations. d-f) fractional changes in each quantity with respect to con300. Note: model grid boxes are considered cloudy if the total condensate mixing ratio exceeds 10^{-5} kg kg^{-1} or 1% of the saturation vapor pressure of water, whichever is smaller.

q_i dominates the decrease in cloud fraction for $T > 224$ K, and so the the domain-averaged q_i increases there. This results primarily from an increase in the amount of ice within deep convective cores; if we were to exclude the 2% of the model domain with the highest column-integrated ice water path (IWP) from the calculation of domain-averaged q_i, then q_i would actually decrease with warming at most upper tropospheric temperature levels. Thus, it is the increase in q_i in the iciest parts of the atmosphere that is responsible for the increase in domain-averaged q_i at fixed temperature. In contrast, the large increase in domain-averaged

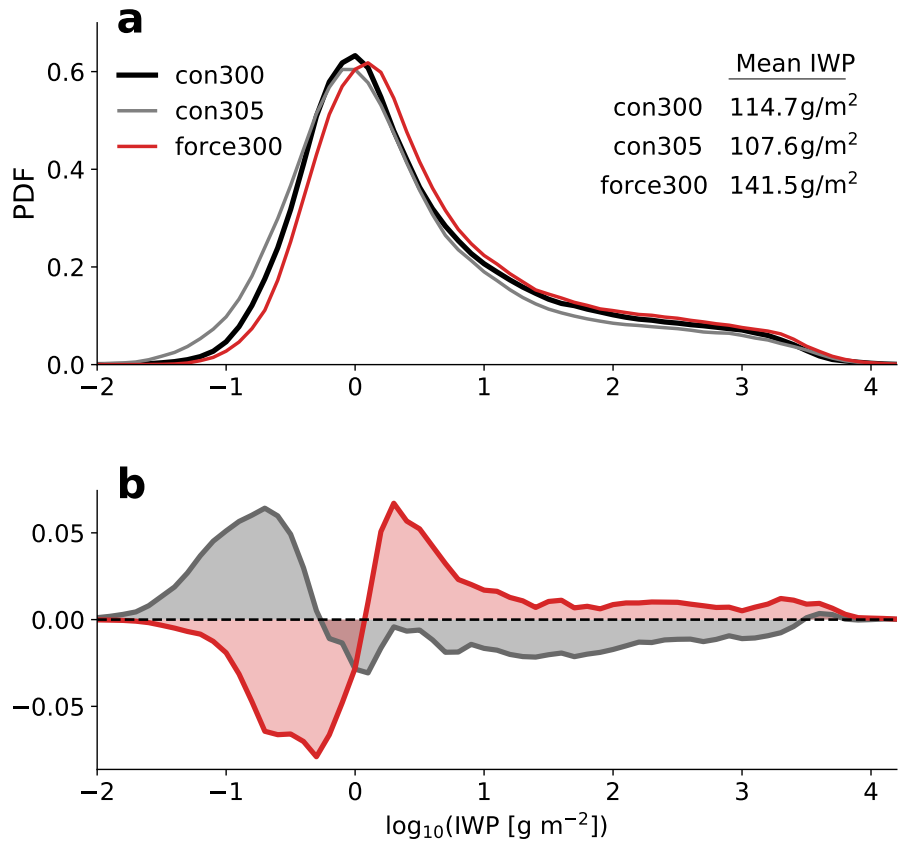

Figure 2.4: a) Probability density functions (PDFs) of $\log_{10}$IWP for each simulation. b) Changes in the IWP PDF with respect to con300.

q_i in force300 comes mostly from an increase in cloud fraction, with a small increase in in-cloud q_i playing a lesser role. These differences make sense: as SSTs warm, the troposphere deepens and warms at its base, and convective updrafts accumulate a greater amount of condensate before reaching any particular isotherm in the upper troposphere. Because there is no warming in force300, any significant increase in domain-averaged q_i must come from changes in cloud fraction.

Cloud changes can be further understood by examining the probability density functions (PDFs) of IWP, shown in Fig. 2.4a. The PDFs are computed from instantaneous 2D

snapshots taken at 6-hour intervals for the final 75 days of each simulation. None of these snapshots contain grid cells with zero IWP, likely because the domain is relatively small and is easily covered by ice spreading out from convective regions. Because true clear-sky conditions do not occur, altering the IWP distribution is a zero-sum game: differences in the PDFs at one IWP must be compensated for by differences at another IWP rather than by differences in the total cloud coverage. In con305, SST warming reduces the coverage of clouds with $\log_{10}$IWP between -0.3 and 3.5 (Fig. 2.4b), which include convective cores, detrained anvil clouds, and other thin cirrus [*Sokol and Hartmann*, 2020]. This reduction is compensated for by an increase in the area with $\log_{10}$IWP between -2 and -0.3, which is as close as it gets to clear-sky conditions in these simulations. In essence, warming shifts the IWP distribution towards lower values, and the mean IWP decreases by 6% as a result (Fig. 2.4a). This may seem counterintuitive given the increase in domain-averaged q_i at fixed temperature shown in Fig. 2.2b, but the pressure and density at a fixed temperature decrease with SST warming, and so the same q_i (kg/kg) corresponds to a smaller ice water content (kg/m^3), which is the quantity used to compute IWP. In force300, the IWP changes are reversed. The frequency of high IWPs increases at the expense of low IWPs, which shifts the distribution towards higher values and increasing the mean IWP by 23%.

In this brief overview of the CRM results, we have found that RCE requires $\dot{s}_{ice}$ to increase in response to an increase in Q_{R+F} whether it is driven by SST warming or an imposed temperature forcing. On the other hand, latent heating efficiency is largely unaffected by the temperature forcing but increases with warming. This allows the q_i profiles in con305 and force300 to differ substantially even at temperatures where $\dot{s}_{ice}$ is equal. In con305, an increase in convective core q_i drives the slight increase in domain-averaged q_i, while in force300 the much larger increase in domain-averaged $q_i$is due mainly to greater cloudiness. These results raise some interesting questions. What is the relationship between latent heating and q_i? Why does the latent heating efficiency increase with SST? And what can this tell us about the q_i response to warming? We address these questions in the following sections.

2.3 An Analytical Model for Latent Heating

Our goal in this section is to develop an expression relating $\dot{s}_{ice}$ to q_i. Eq. 2.2 defines $\dot{s}_{ice}$ in terms of $\dot{q}_{i_{sed}}$, which is the sedimentation tendency of q_i equal to

$$\dot{q}_{i_{sed}} = -\frac{1}{\rho}\frac{\partial F_{sed}}{\partial z} \tag{2.4}$$

where ρ is the air density and F_{sed} is the sedimentation ice flux. In the P3 scheme, this is given by

$$F_{sed} = \rho q_i f V_m \tag{2.5}$$

where V_m is the mass-weighted ice crystal terminal fall speed calculated following *Mitchell and Heymsfield* [2005]. f is an air density modification to V_m which, following *Heymsfield et al.* [2007], is given by $(\rho_0/\rho)^{0.54}$, where ρ_0 is a reference density. Substituting in for f in Eq. 2.5 gives $F_{sed} = \rho_0^{0.54}\rho^{0.46} q_i V_m$. Combining this with Eqs. 2.2 and 2.4 yields

$$\dot{s}_{ice} = \frac{k}{\rho}\frac{\partial}{\partial z}\left(\rho^{0.46} q_i V_m\right) \tag{2.6}$$

where $k = L_s \rho_0^{0.54}$. Expanding the derivative gives

$$\dot{s}_{ice} = \frac{k}{\rho^{0.54}}\left(0.46 q_i V_m \frac{\partial \ln \rho}{\partial z} + q_i \frac{\partial V_m}{\partial z} + V_m \frac{\partial q_i}{\partial z}\right). \tag{2.7}$$

Using the ideal gas law $p = \rho R_d T_v$ and hydrostatic balance $\partial p/\partial z = -\rho g$, it can be shown that

$$\frac{\partial \ln \rho}{\partial z} \approx \frac{1}{T}\left(\Gamma - \frac{g}{R_d}\right) \tag{2.8}$$

where Γ is the lapse rate and R_d the gas constant for dry air. Here we have assumed that the virtual temperature T_v is approximately equal to the absolute temperature T, which is a good approximation over the range of temperatures that we will consider. Combining Eqs.

2.7 and 2.8 and replacing $\partial/\partial z$ with $-\Gamma \cdot \partial/\partial T$ gives

$$\dot{s}_{ice} = \frac{k}{\rho^{0.54}} \left[\Gamma \left(\frac{0.46 V_m q_i}{T} - q_i \frac{\partial V_m}{\partial T} - V_m \frac{\partial q_i}{\partial T} \right) - \frac{0.46 c q_i V_m}{T} \right] \tag{2.9}$$

where $c = g/R_d$. The conversion to temperature coordinates simplifies the comparison of simulations with different SSTs because the temperature at which Q_R falls towards zero—which is also the top of the convective layer—is approximately fixed [*Hartmann and Larson*, 2002]. This is illustrated in Fig. 2.1c, in which the Q_R and Q_{R+F} curves collapse onto one another at ∼220 K.

Eq. 2.9 is useful because it allows us to calculate the domain-averaged $\dot{s}_{ice}$ profile given profiles of T, ρ, q_i, and V_m. If we convert these profiles to temperature coordinates, we can calculate $\partial q_i/\partial T$ and $\partial V_m/\partial T$, which we denote as q_i' and V_m', respectively. Then, using the total differential of Eq. 2.9, we can attribute changes in $\dot{s}_{ice}$ at some fixed T to changes in six different variables:

$$\Delta \dot{s}_{ice} \approx \Delta\rho \frac{\partial \dot{s}_{ice}}{\partial \rho} + \Delta\Gamma \frac{\partial \dot{s}_{ice}}{\partial \Gamma} + \Delta V_m \frac{\partial \dot{s}_{ice}}{\partial V_m} + \Delta V_m' \frac{\partial \dot{s}_{ice}}{\partial V_m'} + \Delta q_i \frac{\partial \dot{s}_{ice}}{\partial q_i} + \Delta q_i' \frac{\partial \dot{s}_{ice}}{\partial q_i'}. \tag{2.10}$$

Here, ΔX denotes the change in X at fixed T relative to some baseline. Expressions for the partial derivatives can be determined analytically from Eq. 2.9 and are provided in section 2.6.1. Eq. 2.10 is an accurate approximation of $\Delta\dot{s}_{ice}$ over the range of atmospheric states produced by the three model runs (section 2.6.2).

2.4 Application to Model Simulations

We can now use Eq. 2.10 to understand the differences in $\dot{s}_{ice}$ between the three simulations. To do so, we must evaluate each term on the right hand side for con305 and force300, using con300 as a baseline. The value of each term can be interpreted as the contribution of that variable to the total change in $\dot{s}_{ice}$ at some particular T. The model provides hourly profiles of domain-averaged T, ρ, q_i, and F_{sed} in height coordinates. For each time step, we compute

Γ and compute the q_i-weighted V_m as $F_{sed}/(f\rho q_i)$, which follows from Eq. 2.5. We then convert the vertical grid to temperature coordinates using the time- and domain-averaged T at each vertical level, interpolate the profiles onto a common T grid, and calculate q_i' and V_m'. We use output from con300 to compute the partial derivatives in Eq. 2.10, and the Δ terms are computed for con305 and force300 with respect to con300.

Fig. 2.5 shows the results of this procedure, with each colored line representing one of the six terms on the right hand side of Eq. 2.10. The bold black lines, which show $\Delta\dot{s}_{ice}$, are equal to the sum of the six individual terms and correspond closely to the differences in the latent heating profiles shown in Fig. 2.2a. The profiles have been normalized by C_p so that they are in K/day. If a profile is near the zero line, then the variable it represents does not change significantly at that T and therefore has little impact on $\dot{s}_{ice}$.

In the following sections, we discuss each variable and its relevance to changes in $\dot{s}_{ice}$ before synthesizing the results with a discussion of latent heating efficiency. All changes (e.g., increases and decreases) mentioned in this section are with respect to con300 unless stated otherwise. It is important to remember that $\dot{s}_{ice}$ is only equal to the total latent heating of s when the effects of liquid condensate are negligible. In our model runs, $\dot{s}_{ice}$ accounts for 90% or more of the total latent heating at temperatures colder than 245 K, and we therefore restrict our analysis to that range.

2.4.1 Density and Lapse Rate

We begin by discussing ρ and Γ together because their values at any particular T are both fundamentally linked to SST. This linkage arises from the fact that the tropical temperature profile is dynamically constrained to be close to a moist adiabat originating from the boundary layer [*Sobel et al.*, 2001], and the temperature of the boundary layer is determined by the SST. Since con300 and force300 have the same SST, they also have similar T profiles and therefore similar ρ and Γ at any particular T. Consequently, in force300 the ρ and Γ contributions to $\Delta\dot{s}_{ice}$ (blue and orange lines in Fig. 2.5b, respectively) are negligible.

On the other hand, SST warming in con305 drives isotherms upwards toward lower

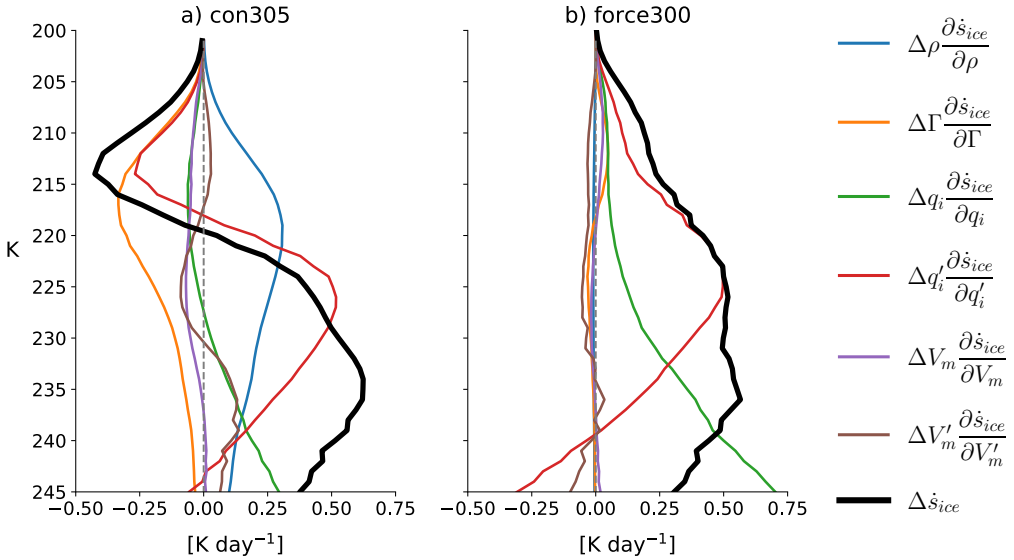

Figure 2.5: Profiles of each term in Eq. 2.10 for a) con305 and b) force300. The terms are normalized by C_p so that they are in K/day. Black lines show the total $\Delta\dot{s}_{ice}$ relative to con300, which is equal to the sum of the six individual terms and corresponds to the differences in the latent heating tendencies in Fig. 2.2a.

pressures, and the ρ at any particular T decreases as a result. Since $\dot{s}_{ice}$ and ρ are inversely related in Eq. 2.9, the decrease in ρ acts to increase $\dot{s}_{ice}$, as evidenced by the positive values of the ρ term (blue line) in Fig. 2.5a. The physical interpretation of this ρ effect is straightforward: ice crystals fall faster at lower air densities because drag is reduced. As ρ decreases, ice crystals are quick to sediment out of a parcel and leave their latent heat behind. Mathematically, the ρ effect stems from the density modification f applied to the ice crystal fall speed, and the magnitude of the ρ effect is therefore sensitive to the formulation of f. But insofar as ρ and fall speed are inversely related, the sign of the ρ effect is robust.

Changes in Γ in con305 act to reduce $\dot{s}_{ice}$, as shown by the orange line in Fig. 2.5a. This, too, arises from the migration of isotherms to lower pressures with warming, which reduces the moist adiabatic lapse rate at any particular T. The pressure dependence of the moist adiabatic lapse rate is indirect, occurring by way of the saturation specific humidity. The reduction in Γ with warming causes our temperature range of interest to expand vertically

in Cartesian space, which "stretches out" and weakens the sedimentation flux divergence, reducing $\dot{s}_{ice}$. The sign of the Γ effect seems robust considering that an increase in static stability (decrease in Γ) with warming has long appeared in observations and models [*Knutson and Manabe*, 1995; *Zelinka and Hartmann*, 2010, 2011; *Bony et al.*, 2016]. It's magnitude, especially in the uppermost UT, could be influenced by the model's representation of ozone. Γ could also be sensitive to model resolution if resolution impacts the entrainment rate, since entrainment modifies the RCE temperature profile [*Zhou and Xie*, 2019].

The arguments in this section, grounded in first principles, tell us that the ρ and Γ effects push $\dot{s}_{ice}$ in opposing directions as SST warms. Ice crystals fall faster but must travel a greater distance from one isotherm to the next. The combined effect of ρ and Γ, which is relatively small compared to their individual effects, is negative at temperatures below 220 K and positive at warmer temperatures, with a positive mass integral between 220 and 245 K. Thus, if all else is equal, warming causes the $\dot{s}_{ice}$ profile to increase in magnitude and shift slightly towards warmer temperatures.

2.4.2 Ice Crystal Fall Speed

We turn now to V_m and V'_m. Unlike ρ and Γ, V_m and V'_m do not have an obvious SST dependence that can be inferred from first principles, so we instead rely here on their prediction by the P3 microphysics scheme. In P3, V_m is determined following *Mitchell and Heymsfield* [2005] and depends on several microphysical quantities, including ice particle density. Ice density is predicted from the scheme's prognostic ice variables and accounts for the effects of riming, which is critical for the simulation of certain convective structures [*Morrison et al.*, 2015]. This makes P3 well suited for the present analysis compared to schemes that sort ice particles into predefined categories with prescribed fall speeds. Changes in V_m between the three simulations reflect changes in ice microphysics and do not necessarily correspond to changes in the *actual* fall speed, since we have separated V_m from its air density modification factor f.

In force300, the V_m and V'_m effects on $\dot{s}_{ice}$ (purple and brown lines in Fig. 2.5b, respec-

tively) are negligible, indicating that changes in ice microphysical properties cannot explain the increase in latent heating. In con305, the V_m and V_m' effects are large enough to warrant discussion but are still relatively small compared to the other terms. V_m increases (becomes less negative) throughout the UT, which acts to reduce $\dot{s}_{ice}$ above the level of maximum q_i (234 K) and enhance $\dot{s}_{ice}$ below. The V_m' effect has a more complicated vertical structure and is largest between 235-240 K, where a steepening of the V_m profile strengthens the sedimentation flux divergence and enhances $\dot{s}_{ice}$.

Understanding the slight differences in V_m and V_m' between our three simulations requires an in-depth analysis of their microphysics. We forgo such analysis here, since the V_m and V_m' effects are relatively small in both con305 and force300, and neglecting them produces only minor changes in $\Delta\dot{s}_{ice}$. Moreover, the insights gained from such an analysis would be specific to the P3 microphysics scheme and the V_m parameterization it employs. The parameterization of V_m is an obvious source of uncertainty in our results, and while the small size of the V_m and V_m' effects alleviates some of this uncertainty, it is possible that a different fall speed parameterization could produce very different results, although this would likely require large microphysical changes. The importance of ice fall speed in the tropical energy budget—underscored by the mere presence of V_m and V_m' in Eq. 2.9 and by a large body of research [e.g., *Grabowski et al.*, 2000; *Mitchell et al.*, 2008; *Sanderson et al.*, 2008]—is worthy of further study.

2.4.3 Cloud Ice

The two remaining terms in Eq. 2.10 are the q_i and q_i' terms, shown respectively by the green and red lines in Fig. 2.5. In force300, the increase in q_i acts to increase $\dot{s}_{ice}$ at all T. The q_i effect is largest at warmer temperatures, where the absolute change in q_i is greatest and where $\dot{s}_{ice}$ is especially sensitive to changes in q_i because V_m is large. The q_i' effect is also significant in force300 and reflects a general steepening of the q_i profile, which causes q_i' at any particular T to increase in magnitude but retain the same sign. If all else is equal, this acts to enhance latent heating above the level of maximum q_i and hinder it below. The q_i'

effect dominates the total change in $\dot{s}_{ice}$ at cold temperatures, whereas the q_i effect dominates at warmer temperatures.

In con305, the q_i and q_i' effects have a more complex vertical structure. This is due to a slight (1-K) warming of the top of the convective layer, which results from an increase in tropospheric stability with SST [*Zelinka and Hartmann*, 2011]. As the top of the convective layer warms, so does the upper extent of the q_i profile, but the lower extent is tied to the freezing level and thus does not warm in the same way. As a result, the q_i profile is vertically squashed in temperature space towards warmer temperatures. One consequence of this shift is that the q_i and q_i' effects are both negative at low T. Between 215-225 K, the q_i' effect increases rapidly with T and becomes larger in magnitude than the q_i effect, which is still negative. This is significant because it produces an increase in $\dot{s}_{ice}$ despite a decrease in the amount of ice. The q_i' effect has the largest magnitude of any term in con305 throughout much of the UT and at some points is even larger than its counterpart in force300. At $\sim$239 K, the q_i, q_i', ρ, and V_m' effects all contribute equally to the increase in $\dot{s}_{ice}$ in con305. This is in stark contrast to force300, in which only the q_i and q_i' effects are significant. This has important implications for the latent heating efficiency, which is discussed in the next section.

2.4.4 Latent Heating Efficiency

Having examined how $\dot{s}_{ice}$ changes in response to warming SSTs and an imposed forcing, we can return to the question posed at the end of section 2.2: why does the latent heating efficiency ϵ increase with SST, and what can this tell us about the q_i response to warming? Just as we did with $\dot{s}_{ice}$, we can decompose changes in ϵ into contributions from the same six variables (section 2.6.1). This decomposition is shown in Fig. 2.6, which is restricted to the 215-245 K range over which ϵ shows a clear dependency on SST. The ρ, Γ, V_m, and V_m' contributions have been grouped into a single "non-q_i" term. These non-q_i terms and q_i' have straightforward effects on ϵ: wherever they act to increase (decrease) $\dot{s}_{ice}$, they also act to increase (decrease) ϵ. The q_i effect on ϵ is more complicated, since q_i appears both explicitly

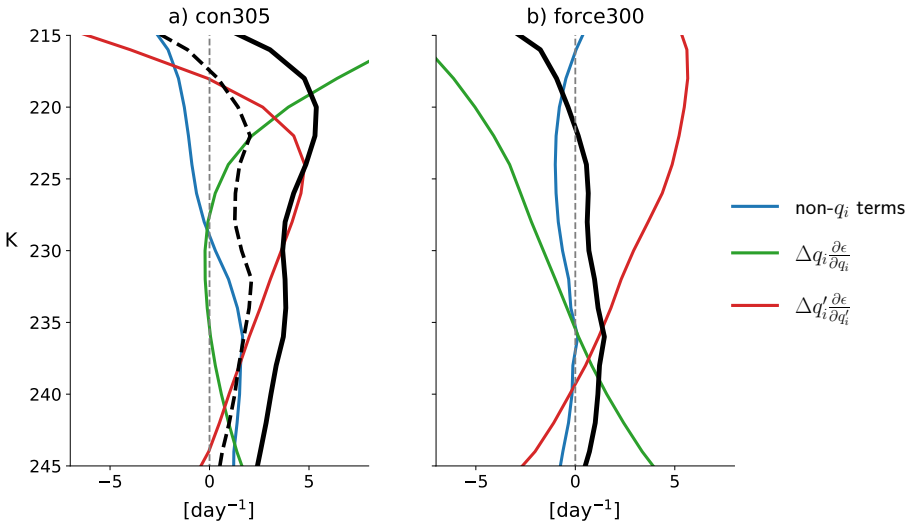

Figure 2.6: Contributions of (blue) non-q_i factors, (green) q_i, and (red) q_i' to changes in the latent heating efficiency ϵ relative to con300 in a) con305 and b) force300. Bold black lines show the total $\Delta\epsilon$, which is equal to the sum of the three colored lines and corresponds to the differences in the ϵ profiles in Fig. 2.2c . The dashed black line in (a) shows $\Delta\epsilon$ for a modified con305 scenario in which the q_i profile was shifted towards colder temperatures by 1 K. Non-q_i terms include ρ, Γ, V_m, and V_m'.

and implicitly (via $\dot{s}_{ice}$) in Eq. 2.3. It can be shown from Eq. 2.3 that

$$\frac{\partial \epsilon}{\partial q_i} = \frac{1}{L_s q_i^2}\left(q_i \frac{\partial \dot{s}_{ice}}{\partial q_i} - \dot{s}_{ice}\right) = \frac{k\Gamma V_m q_i'}{L_s \rho^{0.54} q_i^2} \tag{2.11}$$

The algebraic signs on the right hand side work out such that $\partial\epsilon/\partial q_i$ takes the opposite sign of q_i'. Above the q_i maximum at 234 K, q_i' is positive and so $\partial\epsilon/\partial q_i$ is negative, meaning that ϵ will decrease in response to an increase in cloud ice.

In force300, the total change in ϵ (solid black line in Fig. 2.6b) is relatively small. Since the non-q_i contribution is also small, it must then be the case that the q_i (green line) and q_i' (red line) effects approximately cancel. Indeed, throughout most of the temperature range shown in Fig. 2.6, the decrease in ϵ associated with enhanced q_i is balanced by the increase associated with steeper q_i gradients.

On the other hand, ϵ increases significantly in con305. The non-q_i terms account for approximately half of the ϵ increase at high T but work against the increase at colder T. The rest of the ϵ change is explained by the q_i and q_i' effects, which differ significantly in shape from those in force300 because of the slight warming of the top of the q_i profile. To examine this effect, we shifted the con305 q_i profile towards colder temperatures by 1 K, which brings the top of the profile in line with that from con300. We then recalculated q_i' and ϵ at each T. The dotted black line in Fig. 2.6a shows the resulting $\Delta\epsilon$ profile, which is reduced in magnitude by $\sim$50% or more compared to the actual con305 profile. This shows that approximately half of the ϵ increase in the UT can be explained by the warming of the convective layer top. At warmer temperatures, the non-q_i terms and warming of the convective layer top account for nearly all of the increase in ϵ from con300 to con305. At cold temperatures, where the non-q_i terms work against the ϵ increase, the rest is accounted for by the portions of the q_i and q_i' effects that are not associated with the temperature at the top of the convective layer.

The increase in ϵ with warming can be understood physically as a shortening of the residence time of ice at some particular temperature against sedimentation. This residence time can be expressed as $\tau_{sed} = -q_i/\dot{q}_{i_{sed}}$, where the negative sign converts the sedimentation tendency to a removal rate. Using Eqs. 2.3 and 2.2, it can be shown that $\tau_{sed} = \epsilon^{-1}$. When ϵ is high as in con305, ice is cycled through the upper troposphere at a faster rate, and the climatological q_i at any particular T is kept low by rapid sedimentation. On the other hand, when ϵ is low, ice lingers at a particular temperature for a greater amount of time before sedimenting onward to the next isotherm, and the same latent heating rate is associated with larger climatological q_i. It is important that this shortening of τ_{sed} with warming not be equated with an increase in the fall speed, which is only one of several factors that determine τ_{sed}.

The pattern of increasing ϵ and decreasing τ_{sed} with warming is supported by three additional model runs with SSTs of 295, 310, and 315 K, as shown in Fig. 2.7. Apart from their SSTs, these three runs have identical setups to con300 and con305.

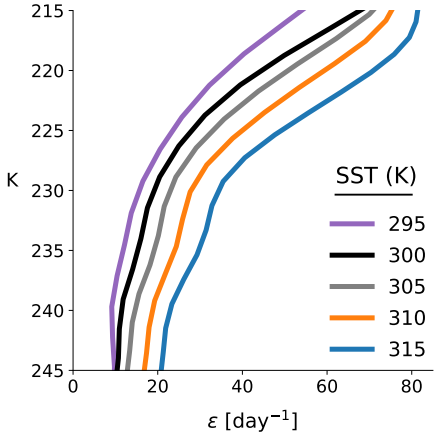

Figure 2.7: Latent heating efficiency ϵ in the upper troposphere in RCE simulations with different SSTs.

2.5 Summary and Discussion

This chapter is motivated by the question of how the mean q_i in the tropical UT would respond to an increase in the radiative cooling rate. In our RCE simulations, the q_i response to warming SSTs is tempered by an increase in the latent heating efficiency ϵ, which allows con305 and force300 to achieve the same latent heating rate with different amounts of ice. The theoretical model developed in section 2.3 reveals that q_i is only one of several factors that determine $\dot{s}_{ice}$ and therefore ϵ. Applying this model to our simulations, we found that the increase in ϵ with warming can be explained primarily by 1) changes in the non-q_i terms and 2) the slight warming of the upper branch of the q_i profile. Another way to understand these results is that ice is cycled across isotherms at a faster rate in con305 than in force300, and the lingering of ice at an isotherm in force300 results in a larger climatological q_i for a given latent heating rate. These results are summarized schematically in Fig. 2.8.

An important limitation of this work is that we have used only one model with one cloud microphysics scheme. Given the wide variety of cloud condensate profiles produced by the CRMs participating in RCEMIP [see Fig. 10c in *Wing et al.*, 2020], it is likely that the q_i response to warming varies considerably across models. But our finding that ϵ increases

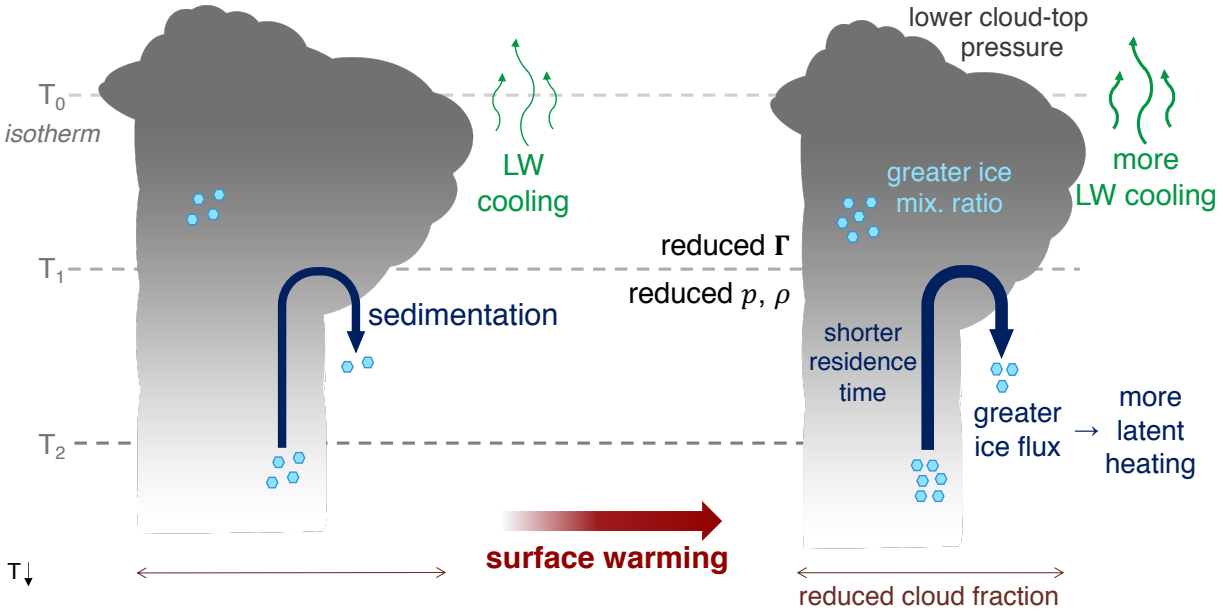

Figure 2.8: Schematic diagram illustrating this chapter's findings. The left side shows a cooler climate, and the right side shows changes that occur with warming. Dashed grey lines are isotherms. The radiative cooling and latent heating rates at a fixed temperature level both increase. As isotherms rise to higher altitudes and lower pressures, the lapse rate Γ and ambient density ρ decrease. Clouds contain a greater amount of ice, but the residence time of ice at any particular temperature shortens. Cloud fraction decreases.

with warming relies on some basic mechanisms that are widely supported by previous work, namely that SST warming causes a slight warming of the convective layer top and a decrease in ρ and Γ at fixed T. Barring drastic intermodel differences in the V_m response to warming, it is reasonable to suspect that the increase in ϵ with warming is robust. It would be beneficial to assess whether the RCEMIP models agree in this regard.

In this study, we have focused primarily on changes in the *domain-averaged* q_i because it can be theoretically linked to the energy balance requirements of RCE, as we have shown. But when it comes to global climate, changes in cloud amount and cloud optical properties with warming are of primary importance. In our RCE simulations, warming SSTs cause a reduction in cloud fraction and an increase in mean in-cloud q_i at fixed temperature (Fig.

2.3). Decreasing ice cloud area is consistent with the long-debated iris hypothesis [*Lindzen et al.*, 2001] and the more recently developed stability iris hypothesis [*Bony et al.*, 2016], both of which predict a reduction in anvil cloud fraction with warming. It is also in agreement with the majority of the cloud-resolving models in the RCEMIP ensemble [*Wing et al.*, 2020]. But it is important to recognize that a reduction in high cloud fraction is *not* an inevitable consequence of an increase in ϵ or an increase in mean q_i. By themselves, increases in ϵ and q_i do not imply any specific changes in cloud amount or optical properties; because deep convection is associated with a variety of cloud types, there are myriad ways by which increases in ϵ and mean q_i could be achieved. The link between mean q_i and cloud fraction is further complicated by, among other factors, warming-induced changes in convective organization [*Emanuel et al.*, 2014; *Wing et al.*, 2017; *Coppin and Bony*, 2018; *Cronin and Wing*, 2017] and the complexity of anvil cloud dynamics [*Schmidt and Garrett*, 2013; *Hartmann et al.*, 2018; *Gasparini et al.*, 2019; *Wall et al.*, 2020].

Future work may focus on the extension of the framework developed here to three dimensions, which would reveal how changes in the mean ice amount and latent heating efficiency are manifested across the distribution of convective clouds. Recently, *Beydoun et al.* [2021] developed a diagnostic framework that is useful for interpreting changes in anvil cloud fraction. The integration of these two frameworks seems particularly promising and could advance understanding of the links between radiative cooling, latent heating, convection, and convective cloud cover.

2.6 Supplementary Information

2.6.1 Analytical expressions for the sensitivities of $\dot{s}_{ice}$ and ϵ

Here we provide expressions for the partial derivatives of $\dot{s}_{ice}$ on the right hand side of Eq. 2.10. These expressions are derived from Eq. 2.9 and used to construct the curves shown in Fig. 2.5. q_i' and V_m' denote $\partial q_i/\partial T$ and $\partial V_m/\partial T$, respectively. As an approximation, q_i and q_i' are treated as independent of one another, as are V_m and V_m'.

$$\frac{\partial \dot{s}_{ice}}{\partial \rho} = -0.54 \frac{\dot{s}_{ice}}{\rho}$$

$$\frac{\partial \dot{s}_{ice}}{\partial \Gamma} = \frac{k}{\rho^{0.54}} \left(\frac{0.46 V_m q_i}{T} - q_i V_m' - V_m q_i' \right)$$

$$\frac{\partial \dot{s}_{ice}}{\partial q_i} = \frac{k}{\rho^{0.54}} \left[\Gamma \left(\frac{0.46 V_m}{T} - V_m' \right) - \frac{0.46 c V_m}{T} \right]$$

$$\frac{\partial \dot{s}_{ice}}{\partial q_i'} = -\frac{k V_m \Gamma}{\rho^{0.54}}$$

$$\frac{\partial \dot{s}_{ice}}{\partial V_m} = \frac{k}{\rho^{0.54}} \left[\Gamma \left(\frac{0.46 q_i}{T} - q_i' \right) - \frac{0.46 c q_i}{T} \right]$$

$$\frac{\partial \dot{s}_{ice}}{\partial V_m'} = -\frac{k q_i \Gamma}{\rho^{0.54}}$$

In section 2.42.4.4, $\Delta\epsilon$ is decomposed in the same manner as $\Delta \dot{s}_{ice}$. The total differential approximation for $\Delta\epsilon$, analogous to Eq. 2.10, is

$$\Delta\epsilon \approx \Delta\rho \frac{\partial \epsilon}{\partial \rho} + \Delta\Gamma \frac{\partial \epsilon}{\partial \Gamma} + \Delta V_m \frac{\partial \epsilon}{\partial V_m} + \Delta V_m' \frac{\partial \epsilon}{\partial V_m'} + \Delta q_i \frac{\partial \epsilon}{\partial q_i} + \Delta q_i' \frac{\partial \epsilon}{\partial q_i'}.$$

Using Eq. 2.3, $\partial\epsilon/\partial X$ can be expressed in terms of $\partial \dot{s}_{ice}/\partial X$ and evaluated using the expressions above, where X is ρ, Γ, q_i, q_i', V_m, or V_m'. The results are used to construct the curves shown in Fig. 2.6.

2.6.2 Validation for the total differential approximation of $\dot{s}_{ice}$

Here we validate the use of the total differential to assess changes in $\dot{s}_{ice}$. Fig. 2.9 shows $\Delta \dot{s}_{ice}$ (relative to con300) for con305 and force300. The solid lines show the true change, calculated by evaluating Eq. 2.9 for each run and taking the difference at each T. Dashed

lines show the approximate change given by the total differential (Eq. 2.10). For both con305 and force300, the total differential approximation is within 10% of the true change at all T with the exception of $T < 205$ K, where the fractional errors are slightly larger because $\Delta \dot{s}_{ice}$ is small in magnitude. This close agreement validates the use of the total differential to attribute changes in $\dot{s}_{ice}$ to changes in other factors. The accuracy of the approximation is similar for changes in ϵ (not shown).

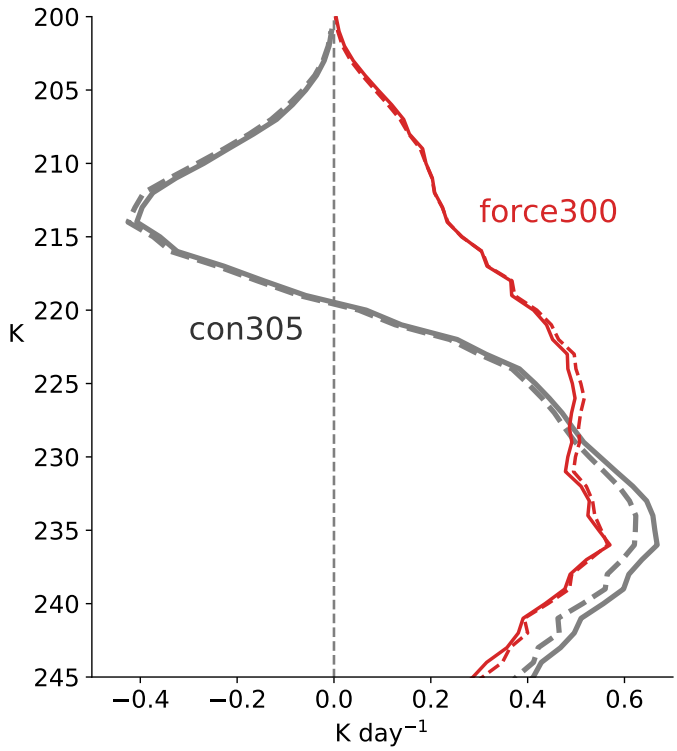

Figure 2.9: Change in $\dot{s}_{ice}$ relative to con300 calculated using (solid lines) Eq. 2.9 and (dashed lines) the total differential approximation given by Eq. 2.10.

Chapter 3

THE ANVIL CLOUD RESPONSE TO WARMING IN RCE AND ITS IMPLICATIONS FOR CLIMATE SENSITIVITY

This work was published as: Sokol, A. B., C. J. Wall, and D. L. Hartmann (2024). Greater climate sensitivity implied by anvil cloud thinning. *Nature Geoscience, 17*(5), 398-403. doi:10.1038/s41561-024-01420-6.

3.1 Introduction

Anvil clouds produced by deep convection are widespread in the Tropics and are a leading source of uncertainty in the recent assessment of climate sensitivity by the WCRP [*Sherwood et al.*, 2020]. Thermodynamic arguments predict that anvil cloud area decreases as the surface warms [*Zelinka and Hartmann*, 2010; *Bony et al.*, 2016], but this could produce a positive, negative, or neutral radiative feedback, since, unlike other cloud types, anvils can have both a positive or negative cloud radiative effect (CRE) at different stages of their life cycle [*Hartmann et al.*, 2018; *Gasparini et al.*, 2019]. Deep convective towers and fresh, thick anvils have a high albedo and a strong, negative CRE, while thinner, aged anvils exert a modest, positive CRE [*Hartmann and Berry*, 2017]. Previous estimates of the anvil area feedback are altogether inconclusive; nevertheless, the maximum likelihood value assessed by the WCRP was substantially negative (-0.2 W/m^2/K, with a Gaussian standard deviation of 0.2 W/m^2/K). Here, we will show that such a negative feedback is not supported by an ensemble of state-of-the-art, cloud-resolving models (CRMs). To the contrary, the models predict that reductions in high cloud area come mostly from thick, reflective anvil clouds that cool the climate. The clouds left behind are optically thinner on average and have a more positive climatological CRE.

Previous work examining the relationship between surface temperature (T_s) and convective cloud area generally supports a reduction in cloud area with warming, albeit with regional and methodological sensitivities [*Ito and Masunaga*, 2022; *Kubar and Jiang*, 2019; *Saint-Lu et al.*, 2020, 2022; *Lindzen et al.*, 2001; *Su et al.*, 2008; *Zelinka and Hartmann*, 2011; *Choi et al.*, 2017; *Igel et al.*, 2014; *Liu et al.*, 2017; *McKim et al.*, 2024]. Estimates of the associated radiative feedback, however, range from significantly negative [*Choi et al.*, 2017; *Lindzen et al.*, 2001; *Mauritsen and Stevens*, 2015] to nearly neutral [*Ito and Masunaga*, 2022] or slightly positive [*McKim et al.*, 2024; *Chambers et al.*, 2002; *Lin et al.*, 2002; *Li et al.*, 2019; *Williams and Pierrehumbert*, 2017]. This continued uncertainty may arise, in part, from the use of various cloud classifications (e.g., cirrus, high cloud, anvil, stratiform, etc.) based on arbitrary thresholds that vary from study to study. In reality, tropical convection generates a continuum of ice clouds, with thick cumulonimbi on one end and thin cirrus on the other. This continuum perspective is valuable because it reflects real physical processes—the production, gradual thinning, and eventual dissipation of ice clouds—and provides an intuitive way of understanding the role of convectively generated clouds in tropical climate.

Here, we examine the ice cloud continuum using ice water path (IWP) as a coordinate. IWP—the total mass of condensed ice in the atmospheric column—can be estimated from satellite observations, is easily calculated from model output, and is closely linked to CRE and cloud optical depth (τ; Figure 3.1). Changes in the frequency distribution of IWP are therefore informative for understanding the impact of ice clouds on the top-of-atmosphere radiative balance.

We apply the continuum perspective to an ensemble of CRMs in which deep convection and anvil evolution are explicitly simulated. As part of the Radiative-Convective Equilibrium Model Intercomparison Project (RCEMIP) [*Wing et al.*, 2018], these models were run on a limited-area, oceanic domain large enough to permit large-scale convective organization (section 3.2.2). Simulations were conducted for three fixed, uniform T_s values (295, 300, and 305 K). We will show that the ice cloud response to warming is characterized by two regimes:

a robust reduction in thick ice cloud area that is consistent with existing thermodynamic arguments, and a small but uncertain change in thin ice cloud area. Such changes produce an overall thinning of the cloud population and a positive opacity feedback, implying a +0.3 °C shift in the WCRP estimate of equilibrium climate sensitivity (ECS).

3.2 Model Simulations and Satellite Data

3.2.1 Satellite retrievals of Ice Water Path

We use three different satellite retrievals to construct an observational baseline of the IWP distribution in tropical convective regions. All three are combined radar-lidar retrievals that use measurements from the CALIOP lidar [*Winker et al.*, 2009] and the CloudSat radar [*Stephens et al.*, 2002]. Both instruments are part of the A-train satellite constellation. The three retrievals are DARDAR-Cloud version 2.1.1 [*Delanoë and Hogan*, 2010], DARDAR-Cloud version 3.1 [*Cazenave et al.*, 2019], and 2C-ICE R05 [*Deng et al.*, 2010]. The two versions of DARDAR-Cloud differ principally in their treatment of cloudy volumes detected by the lidar only [*Cazenave et al.*, 2019]. All three products also include retrievals of cloud optical depth, τ, which allows for an approximate conversion between IWP and τ to facilitate

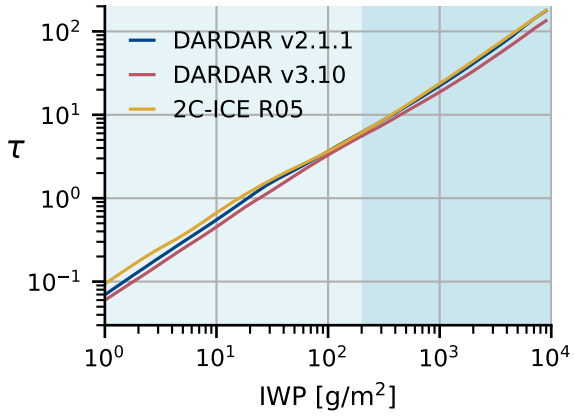

Figure 3.1: Mean ice cloud optical depth τ as a function of IWP in the three combined radar-lidar satellite retrievals. Bin widths are 0.1 for $\log_{10}$IWP.

comparison with previous work (Figure 3.1).

3.2.2 RCEMIP Cloud-Resolving Model Simulations

This analysis uses output from the "RCE_large" simulations of RCEMIP. The full simulation protocol is described in [*Wing et al.*, 2018]. Briefly, the simulations have a domain size of ∼6,000×400 km^2 with 3-km horizontal resolution. They used three fixed, uniform sea surface temperatures (295, 300, and 305 K) and were integrated for 100 days. We use the instantaneous 3D output (every 6 hours) from the last 25 days of each run. Instantaneous IWP is computed by vertically integrating the total (precipitating and nonprecipitating) atmospheric ice content. We included precipitating ice to be consistent with the satellite observations, which do not distinguish between ice types.

Our analysis includes all of the RCEMIP CRMs for which the necessary, standardized output is publicly available, with the exception of UKMO-RA1-T-nocloud and UKMO-CASIM. UKMO-RA1-T-nocloud is the same as UKMO-RA1-T apart from its deactivation of a subgrid cloud scheme. UKMO-CASIM is excluded because the unique vertical structure of convection in that model produces an IWP distribution that does not reflect deep convective cloud climatology, but rather expansive, stratiform ice clouds produced by convective detrainment near the freezing level. We also include the RCEMIP_large-style simulations described in [*Sokol and Hartmann*, 2022], which use the SAM model [*Khairoutdinov and Randall*, 2003] with P3 microphysics [*Morrison et al.*, 2015] (referred to as SAM-P3).

3.3 Convective clouds as a continuum of ice

The continuum of tropical ice clouds can be represented by a discrete frequency distribution of IWP [*Berry and Mace*, 2014; *Chen et al.*, 2016]. We denote this distribution as f(IWP), which can be interpreted as the IWP-resolved cloud fraction. Similarly, we denote the mean CRE of convectively generated ice clouds as CRE(IWP). Satellite-derived estimates of f from the tropical West Pacific, along with model-estimated CRE, provide an intuitive understanding of convective cloud evolution (Figure 3.2). At high IWP ($> 10^3$ g/m^{-2}), deep

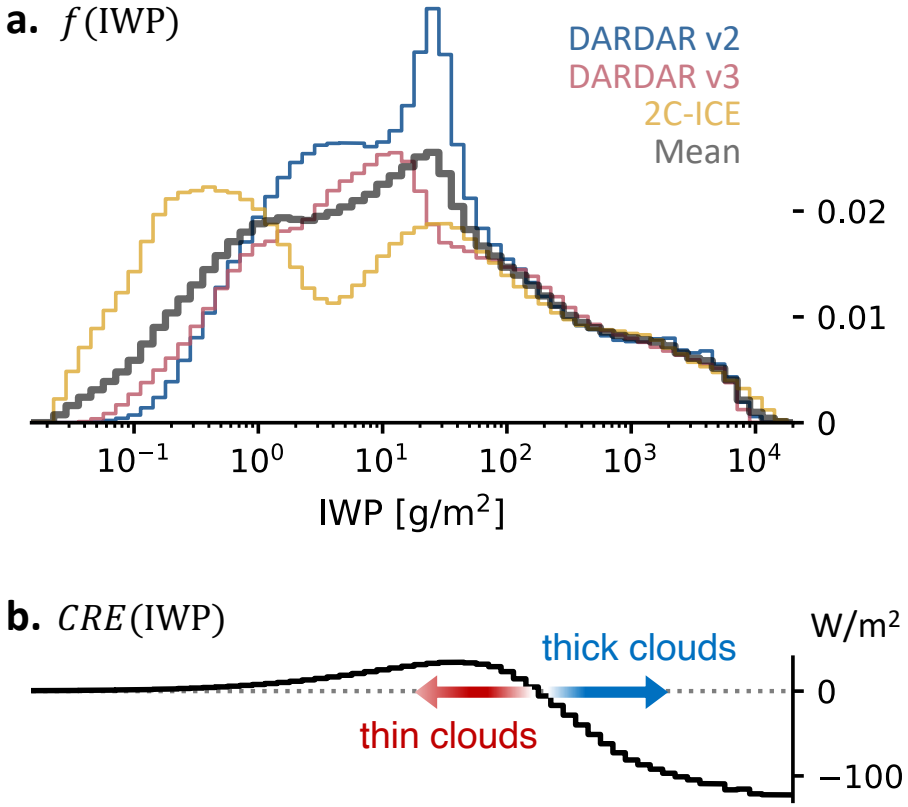

Figure 3.2: The tropical ice cloud continuum. **(a)** f(IWP) derived from satellite observations of the tropical West Pacific (150-180°E, 15°S-15°N) for 2009. Three satellite retrievals and their mean are shown. **(b)** Multimodel mean CRE(IWP) for the CRM simulations with T_s=300 K.

convective cores have a large, negative CRE but cover a small area. As IWP decreases, f and CRE both increase rapidly, which reflects the thinning and spreading of detrained anvils. Maximum f occurs around 15-35 g/m^2 (τ ∼1-2), which approximately coincides with the CRE maximum; the most abundant anvil clouds are therefore those with the strongest warming effect. These clouds counteract the cooling effect of thicker clouds, leading to a climatological CRE near zero in tropical convective regions [*Ramanathan et al.*, 1989; *Hartmann et al.*, 2001].

The CRM ensemble produces a wide variety of IWP distributions with varying degrees of

similarity to the satellite-derived f (Figure 3.3). In general, the models capture the maximum IWP of 2-4$\times 10^4$ g/m^2 and the rapid increase in f as IWP decreases from 10^3 to 10^2 g/m^2. More than half of the models produce a relative maximum or plateau near the observed range of 15-35 g/m^2. This suggests that the models are generally capturing the basic thinning and spreading of anvil clouds after detrainment, and that the convective cloud continuum can be captured even in idealized representations of the tropical atmosphere. While the individual f(IWP) curves produced by each model vary significantly, we will show that the *change* in

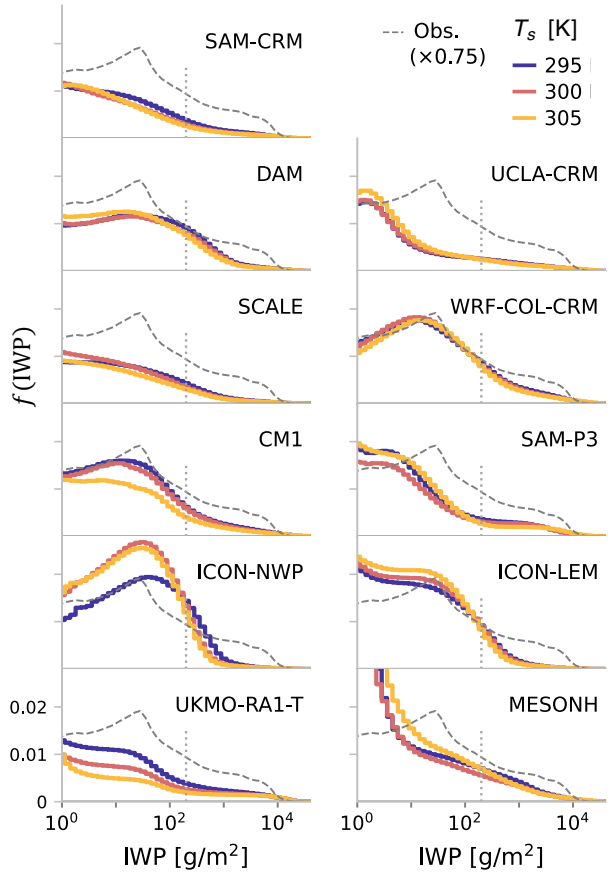

Figure 3.3: Model representations of the ice cloud continuum. Panels show f(IWP) for each model and T_s. Dashed grey lines show the mean of the three satellite-derived estimates of f, scaled arbitrarily by a factor of 0.75 to aid comparison of distribution shapes. Vertical, dotted grey lines mark the cutoff between thick and thin clouds.

f in response to surface warming follows a robust pattern across the ensemble.

In the deep Tropics, the ice cloud continuum is dominated by clouds with tops near the level of deep convective detrainment [*Stephens et al.*, 2018]. Mid-level ice clouds are very rare in the observations and model simulations considered here (Figure 3.4), so we are confident that f reflects a continuum of high clouds consisting of deep convective towers, their attached anvils, and thin cirrus of convective or in-situ origin. Based on Fig. 3.2, the continuum can

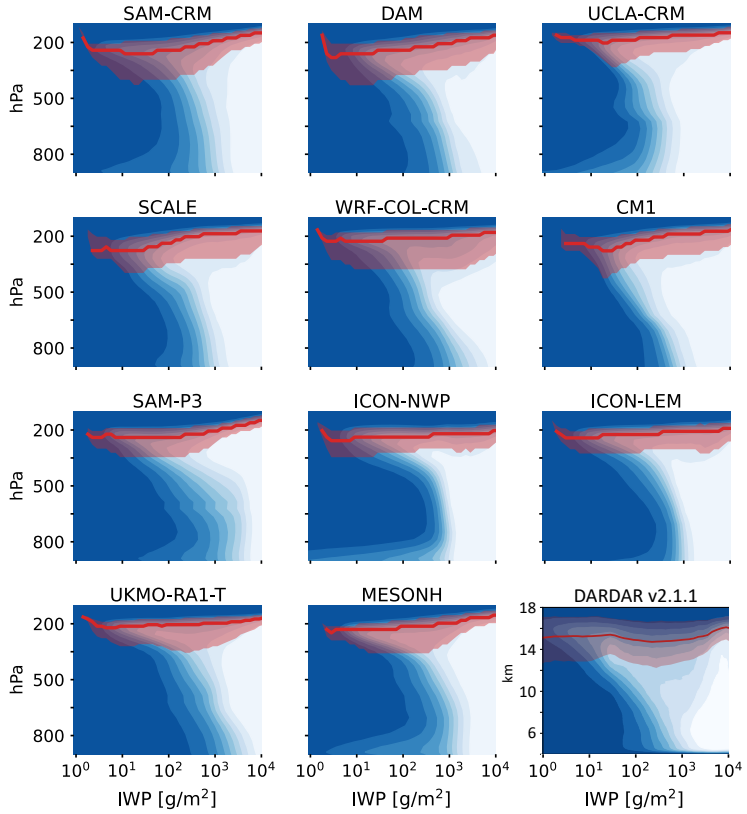

Figure 3.4: Cloud fraction composited by IWP for the simulations with T_s=300 K and the DARDAR v2.1.1 satellite retrieval (bootom right). Red lines show the mean cloud top height (CTH; shading is 10th-90th percentile). For the simulations, grid boxes are considered cloudy if the total condensate mixing ratio exceeds 10^{-5} kg/kg. CTH statistics do not extend all the way down to IWP=1 g/m^2 because such low IWPs can only result from ice mixing ratios below the cloudiness threshold. For the satellite retrieval, cloudy volumes are those with nonzero ice water content and visible extinction coefficients exceeding 0.125 km^{-1} [*Sokol and Hartmann*, 2020]. Data are for 150-180°E and 12°S-12°N for the 2009.

be divided into two categories with physical relevance for cloud-climate interactions: clouds with $CRE < 0$ and those with $CRE > 0$. We refer to these as thick and thin clouds, respectively, and separate them by an IWP threshold corresponding to the change in sign of the multimodel mean CRE. The area fractions covered by thick and thin clouds are then

$$f_{\text{thick}} = \sum_{200\,\text{g/m}^2}^{\infty} f(\text{IWP})$$

$$f_{\text{thin}} = \sum_{1\,\text{g/m}^2}^{200} f(\text{IWP})$$

and the total ice cloud fraction is $f_{\text{ice}} = f_{\text{thick}} + f_{\text{thin}}$. Clouds with IWP$<$ 1 g/m^2 have a small CRE and are excluded from our analysis due to the tendency of some models to produce numerically small IWP values over large swaths of the domain. We exclude these cirrus because they can have an outsized influence on cloud fraction statistics despite their negligible influence on radiative fluxes. We repeated our analysis using alternative thresholds of 0.1 and 10 g/m^2, which does not have an appreciable quantitative effect on our results.

The domain-averaged CRE of ice clouds, denoted here as C_{ice}, can be similarly decomposed into thick- and thin-cloud contributions, C_{thick} and C_{thin}, respectively. We first define the area-weighted CRE as

$$C(\text{IWP}) = f(\text{IWP}) \cdot CRE(\text{IWP}) \tag{3.1}$$

which represents the CRE of a particular IWP bin averaged over the entire domain. Then, as with f, C_{ice}, C_{thick}, and C_{thin} are found by summing C over the relevant IWP intervals (Table A3.1).

3.4 Ice cloud thinning in response to warming

The response of f to surface warming varies substantially across the ensemble (Fig. 3.3, Table A3.2). To identify robust aspects of the response, we compute the multimodel mean fractional

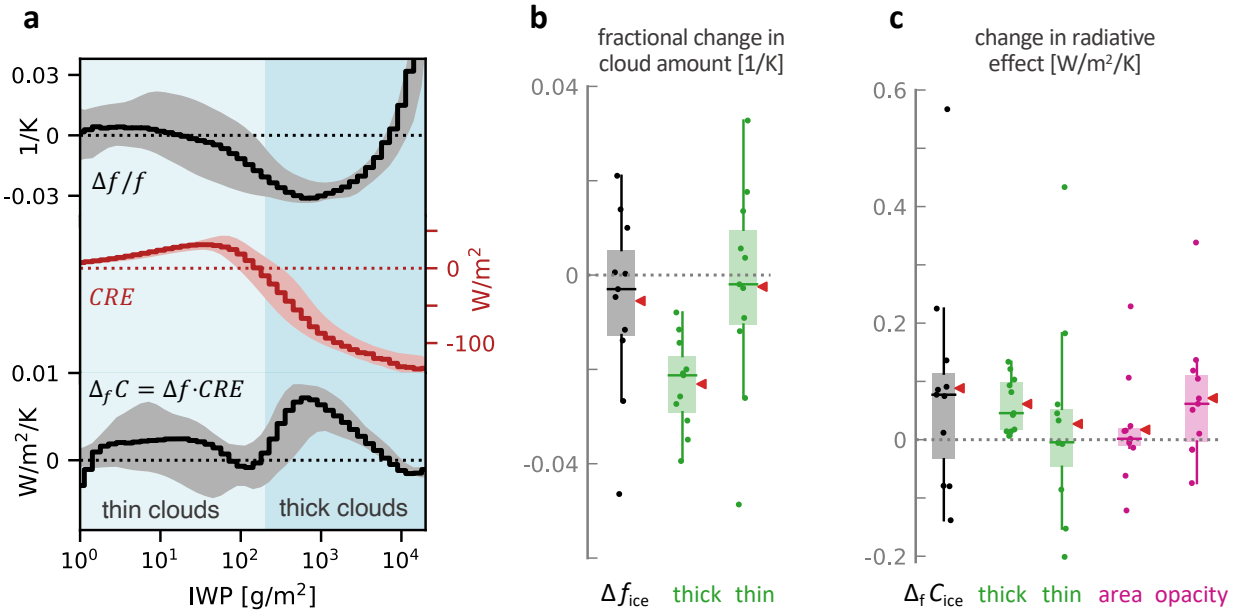

Figure 3.5: The ice cloud response to warming and its radiative effects. **(a)** fractional change in f(IWP), CRE(IWP) for $T_s = 295$ K, and $\Delta_f C$, the change in domain-averaged CRE due to changes in f alone. Lines show multimodel means and shading shows 25-75th percentiles. **(b)** Fractional change in f_{ice} and its decomposition into thick- and thin-cloud components. **(c)** $\Delta_f C_{\text{ice}}$, its thick- and thin-cloud components, and its area and opacity components. All values are normalized by ΔT_s. For box plots, boxes show Q1-Q3, dashes show medians, red triangles show means, and dots show individual models.

change in f between 295 and 305 K (Fig. 3.5a). This shows that f increases with warming at the largest IWPs, reflecting an increase in the ice content of the strongest convective updrafts. Otherwise, we find that thick clouds consistently contract across the entire ensemble, with a mean change in f_{thick} of -2 %/K. This change, reflective of a decrease in the area occupied by deep convective cores and fresh anvils, is in line with the anticipated weakening of the mean convective mass flux [*Knutson and Manabe*, 1995; *Held and Soden*, 2006; *Jeevanjee*, 2022]. In theory, this weakening could manifest as a decrease in the convective area fraction, a decrease in the vertical velocity within convection, or some combination thereof. Since convective storms are expected to be *more* vigorous with warming [*Singh et al.*, 2017; *Romps*, 2016], it seems likely that convective area fraction decreases. This could arise from a reduction

in the number of convective events or a decrease in their typical width, but the present analysis does not discern between these two mechanisms. Regardless, the reduction in f_{thick} seen here suggests that changes in convective area fraction affect not only deep convective cores, but also fresh, thick anvil clouds, which are typically attached to convective cores and undergo relatively rapid thinning after their formation [*Lilly*, 1988; *Jensen et al.*, 2018]. The impressive agreement between the CRMs (Fig. 3.5b) suggests that this response is rooted in fundamental physics shared by all of the models.

In contrast to the reduction in f_{thick}, there is no model consensus on changes in thin cloud area. The ensemble is evenly split on the sign of Δf_{thin}, resulting in a small ensemble mean response despite wide intermodel spread (Fig. 3.5b). The mismatch between changes in f_{thick} and f_{thin} suggests that the thin cloud response is not as tightly constrained by changes in the convective mass flux. This is in line with our current understanding that the spreading, thinning, and maintenance of aged anvils are driven by various microphysical and radiative processes that are not directly related to the total convective mass flux [*Schmidt and Garrett*, 2013; *Gasparini et al.*, 2019; *Hartmann et al.*, 2018; *Wall et al.*, 2020; *Dobbie and Jonas*, 2001]. Intermodel differences in the representation of these processes (particularly microphysics) almost certainly impact the simulated thin cloud response. With these insights into the anvil life cycle, it is perhaps unsurprising that Δf_{thin} is poorly constrained compared to Δf_{thick}. Since thin clouds are much more abundant than thick ones, changes in f_{ice} largely reflect those in f_{thin} (Tables A3.1-A3.2). Intermodel spread in Δf_{ice} is best explained by Δf at $\sim$20 g/m^2 (r^2=0.92; Figure 3.6), which closely corresponds to the most abundant IWP in observations and some models.

With a robust reduction in f_{thick} and a small mean change in f_{thin}, the ensemble suggests that the ice cloud population becomes thinner in response to surface warming. The ratio of thin to thick clouds increases in all but one of the models, demonstrating that this thinning can occur regardless of whether the total ice cloud fraction increases, decreases, or stays the same. This thinning is qualitatively consistent with the previous finding that thick high clouds respond more readily than thin high clouds to interannual T_s variability observed in

the real Tropics [*Kubar and Jiang*, 2019; *Höjgård-Olsen et al.*, 2022; *Liu et al.*, 2017; *Li et al.*, 2019; *Stubenrauch et al.*, 2021].

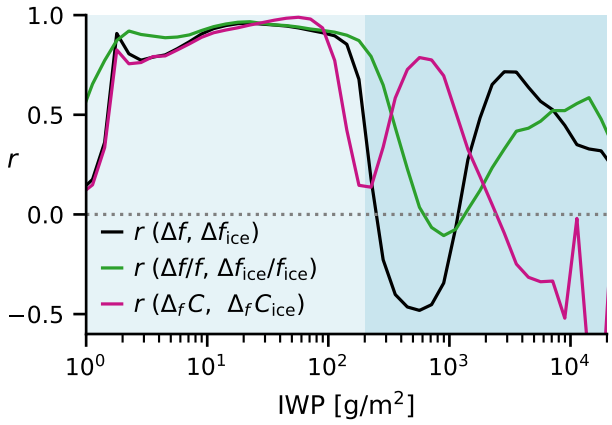

Figure 3.6: Correlation coefficients are shown for various quantities. Black: absolute changes in $f(\text{IWP})$ and f_{ice}. Green: fractional changes in $f(\text{IWP})$ and f_{ice}. Pink: $\Delta_f C(\text{IWP})$ and $\Delta_f C_{\text{ice}}$.

3.5 A positive opacity feedback

3.5.1 Analytical Framework

We now seek to understand how changes in the ice cloud continuum affect C_{ice}, the domain-averaged CRE of ice clouds which can be expressed as

$$C_{\text{ice}} = \sum_{1\,\text{g/m}^2}^{\infty} C(\text{IWP}) = \sum_{1\,\text{g/m}^2}^{\infty} f(\text{IWP}) \cdot CRE(\text{IWP}) \tag{3.2}$$

The Cess-type cloud feedback is defined as the change in domain-averaged CRE normalized by ΔT_s [*Cess and Potter*, 1988]. It differs slightly from the formal cloud feedback parameter computed by partial radiative perturbation *Soden et al.* [2004]. In traditional feedback analysis, the total cloud feedback is often decomposed into cloud altitude, area, and opacity components. Resolved across the IWP continuum, the total Cess-type, ice cloud feedback is

expressed as

$$\Delta C(\text{IWP}) = CRE \cdot \Delta f + f \cdot \Delta CRE + \Delta f \cdot \Delta CRE \tag{3.3}$$

where all variables are functions of IWP and all Δ terms are assumed to be normalized by ΔT_s. The multimodel mean of the three terms on the right-hand side are shown in Figure 3.7. The final term on the right-hand side (purple line in Fig. 3.7) is a small nonlinear term that we neglect here. The second term on the right-hand side (green line in Fig. 3.7) accounts for changes in CRE(IWP), which may occur due to changes in clear-sky fluxes or cloud temperature, altitude, and microphysical structure. This term encompasses so-called cloud masking effects [*Soden et al.*, 2004], the entire ice cloud altitude feedback, as well as the microphysical part of the opacity feedback, which manifests as a change in the optical depth associated with a particular IWP. While this term is significant, it is not our focus here.

Our interest here is in the first term on the right-hand side of Eq. 3.3, which we define as $\Delta_f C$:

$$\Delta_f C(\text{IWP}) = \Delta f(\text{IWP}) \cdot CRE(\text{IWP}) \tag{3.4}$$

This is the part of ΔC attributable to changes in the frequency of a particular IWP. $\Delta_f C_{\text{ice}}$, equal to the sum of $\Delta_f C$ across all IWP > 1 g/m^2, is thus the change in the domain-averaged

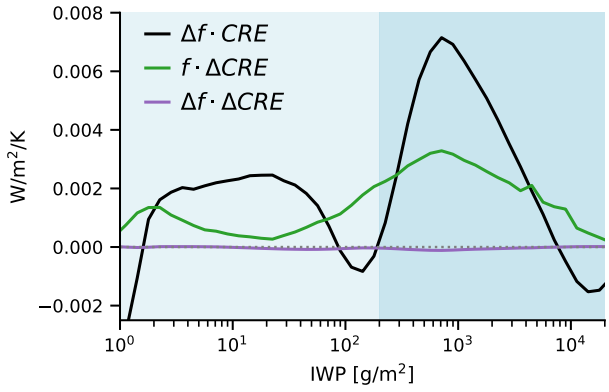

Figure 3.7: Decomposition of $\Delta C = \Delta(f \cdot CRE)$ into its three component terms (Eq. 3.3)

CRE of ice clouds due to changes in f alone. This can be separated into thick- and thin-cloud contributions by summing $\Delta_f C(\text{IWP})$ across the respective IWP ranges.

$\Delta_f C_{\text{ice}}$ encompasses the entire ice cloud area feedback and the remaining part of the ice cloud opacity feedback, since nonuniform changes in f can drive changes in mean ice cloud opacity. To formally separate the area and opacity components, we first define the fractional change in $f(\text{IWP})$ as

$$g(\text{IWP}) = \frac{\Delta f}{f} \tag{3.5}$$

which can be decomposed as

$$g(\text{IWP}) = G + g'(\text{IWP}) \tag{3.6}$$

where $G = \Delta f_{\text{ice}}/f_{\text{ice}}$ is the fractional change in total ice cloud fraction and g' is the deviation from G at a particular IWP. Combining Eqs. 3.5 and 3.6 yields

$$\Delta f = f \cdot (G + g') \tag{3.7}$$

which when substituted into Eq. 3.4 yields

$$\Delta_f C = C(G + g') \tag{3.8}$$

where we have employed Eq. 3.1. $\Delta_f C_{\text{ice}}$ is then found by summing over all IWP > 1 g/m^2:

$$\Delta_f C_{\text{ice}} = G \sum_{1\,\text{g/m}^2}^{\infty} C + \sum_{1\,\text{g/m}^2}^{\infty} g' C \tag{3.9}$$

which, using the definitions of C_{ice} and G, simplifies to

$$\Delta_f C_{\text{ice}} = \Delta f_{\text{ice}} \cdot \overline{CRE} + \sum_{1\,\text{g/m}^2}^{\infty} g' C \tag{3.10}$$

where $\overline{CRE} = C_{\text{ice}}/f_{\text{ice}}$ is the conditionally averaged ice cloud CRE. The first term on the

right-hand side is the area component of $\Delta_f C_{\text{ice}}$, which is attributable to changes in total ice cloud fraction assuming fixed $\overline{CRE}$ (i.e., a uniform fractional change in f across all IWP). The second term is the opacity component, which accounts for deviations from a uniform fractional change, which causes bulk thinning or thickening of the ice cloud population and may affect $\overline{CRE}$. The opacity component does not account for the microphysically driven opacity changes included in the second term of Eq. 3.3.

Recently, *McKim et al.* [2024] developed a simplified expression for the anvil cloud area feedback (their Eq. 9, which they refer to as the Iris feedback). Unlike the Cess-type feedbacks discussed above, their expression aligns with traditional feedback formalism. Discretizing their expression shows that it is the same as the cloud area component of Eq. 3.10, with the addition of a cloud overlap term. Therefore, $\Delta_f C_{\text{ice}}$ can be interpreted as the sum of the ice cloud area feedback and the part of the opacity feedback related to changes in f. With regard to our treatment of cloud overlap here, the formulation of $CRE(\text{IWP})$ described in section 3.5.1 must be kept in mind. Whether or not the radiative effects of cloud liquid are included in $\Delta_f C$ depends on IWP. At high IWPs corresponding to deep convective cores and very thick anvil clouds, we have assumed that any liquid present in the column belongs to the same cloud system as the ice, and the all-sky CRE is thus used to evaluate $\Delta_f C$. On the other hand, at low IWPs, $\Delta_f C$ is evaluated using the ice-only CRE. This means, for example, that the ice-free area exposed by a reduction in f is partially occupied by low clouds exerting a negative radiative effect. The low-cloud CRE in the newly exposed regions is assumed to be equal to the difference between the all-sky and ice-only CREs. This is likely an underestimate, since the CREs of overlapping low and high clouds are not simply additive in reality. However, the impact of this bias on $\Delta_f C_{\text{ice}}$ is small due to compensating effects of models with increasing and decreasing thin cloud area. To account for this potential uncertainty, our analysis of ECS includes sensitivity tests, described below.

3.5.2 Model Results

We assess $\Delta_f C$ and $\Delta_f C_{\text{ice}}$ separately for each model between 295–305 K. All but three produce positive $\Delta_f C_{\text{ice}}$ (Fig. 3.5c; Table A3.2), demonstrating that cloud thinning can lead to an increase in climatological CRE regardless of whether f_{ice} increases or decreases. The ensemble mean $\Delta_f C_{\text{ice}}$ is +0.09 W/m^2/K; nearly all of this increase comes from thick cloud changes, while the mean thin-cloud contribution is again very small but with considerably more spread (Fig. 3.5c). Intermodel spread in $\Delta_f C_{\text{ice}}$ is well explained by its thin-cloud component (r^2=0.95) and best predicted by $\Delta_f C$ at 40-70 g/m^2 (r^2=0.97; Fig. 3.6).

$\Delta_f C_{\text{ice}}$ can be decomposed into two parts analogous to conventional cloud area and opacity feedbacks (section 3.3). The area component assumes a uniform fractional change in f and no change in $\overline{CRE}$, the conditionally averaged CRE of ice clouds. In most of the models, the area component is very small (Fig. 3.5c), either because Δf_{ice} is small or because the ice cloud population is about radiatively neutral to begin with. This is in line with previous arguments suggesting that the radiative neutrality of convective clouds constrains the area feedback to be small [*Pierrehumbert*, 1995].

The opacity component of $\Delta_f C_{\text{ice}}$ accounts for changes in $\overline{CRE}$ brought about by nonuniform changes in f, such as the thinning of the cloud population described above. Unlike the area component, the opacity 3.5c), reflecting a mean increase in $\overline{CRE}$ due to cloud thinning. The ensemble mean opacity component accounts for nearly all of the magnitude of $\Delta_f C_{\text{ice}}$, suggesting that when it comes to anvil radiative feedbacks, the total change in cloud area is less important than *how* that change is spread across the ice cloud continuum. The CRMs show impressive agreement in this regard, as does at least one general circulation model with parameterized convection [*Li et al.*, 2019]. Again, intermodel spread in the area and opacity components is well explained by the spread in Δf_{thin} (Figure 3.8).

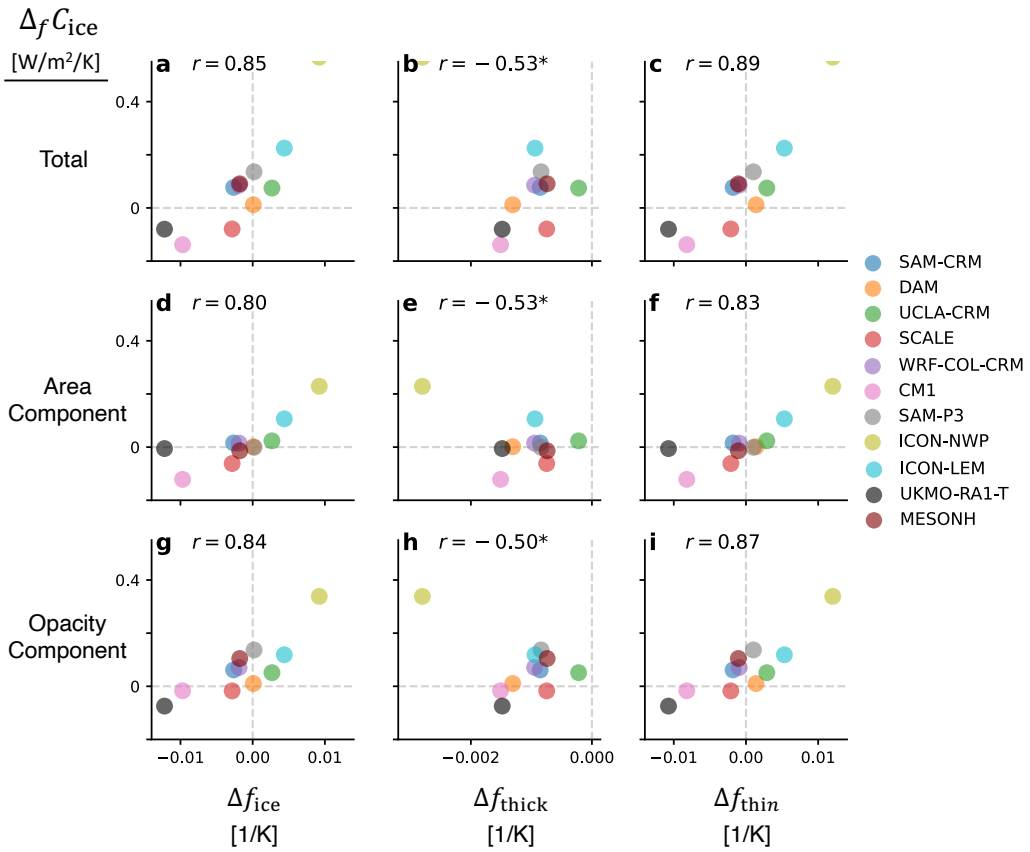

Figure 3.8: Δf_{ice}, Δf_{thick}, and Δf_{thin} versus $\Delta_f C_{\text{ice}}$ and its area- and opacity-related components. Correlation coefficients are marked with an asterisk if *not* statistically different from zero with 95% confidence. All values are normalized by ΔT_s.

3.6 Implications for climate sensitivity

The positive feedback predicted by the CRM ensemble represents a significant departure from the WCRP estimate of the combined anvil area and opacity feedback, suggesting that clouds act to enhance global warming more than was assumed in the WCRP assessment of ECS. To update that assessment, we seek to replace the previous feedback estimate with our RCEMIP-informed value and generate a new probability density function (PDF) of ECS. The PDF is generated using the Bayesian inference code from *Sherwood et al.* [2020] with all three lines of evidence used in the original WCRP analysis (historical, process-based, and

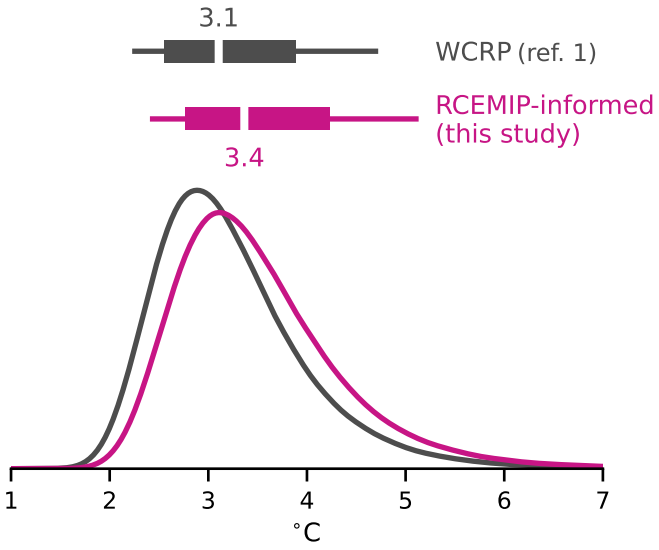

Figure 3.9: Updating the probability density function of ECS. Grey: baseline WCRP feedback estimate of $N(-0.20, 0.20)$ W/m^2/K, where $N(x, y)$ is a Gaussian with mean x and standard deviation y. Pink: updated calculation using the RCEMIP-informed value of $N(0.03, 0.06)$ W/m^2/K. Above, the thin horizontal lines and boxes show 90% and 66% confidence intervals, respectively, and white dashes show the central estimate (median).

paleoclimatological).

To derive the RCEMIP-informed feedback value, we must convert the multimodel mean $\Delta_f C_{\text{ice}}$ to a global mean feedback. To that end, we multiply $\Delta_f C_{\text{ice}}$ by the fractional area of Earth's tropical oceans (37%) and assume that the Tropics warm by 0.9 °C for every degree of global mean warming [*Lee, J.-Y. et al.*, 2021]. This gives a feedback estimate of $N(0.03, 0.06)$ W/m^2/K, where, following the WCRP convention [*Sherwood et al.*, 2020], $N(x, y)$ is a Gaussian with mean x and standard deviation y, which we set equal to the feedback standard deviation across the RCEMIP ensemble. While the RCEMIP-informed feedback is small in magnitude compared to other cloud feedbacks, it is a large change from the previous estimate and corresponds to a 51% increase in the total cloud feedback assessed by the WCRP.

Updating the feedback results in a broad +0.3°C shift in the ECS PDF (Figure 3.9). The

central estimate (median) increases from 3.1 to 3.4 °C, and the 66% likely range from 2.6-3.9 to 2.8-4.2 °C (Table 3.1). The ∼10% widening of the likely range is counterintuitive given the reduction in anvil feedback uncertainty relative to the WCRP assessment. The reduction in uncertainty is outweighed by the increase in the central estimate of the feedback, which acts to broaden the PDF due to the nonlinear relationship between ECS and feedback strength [*Roe and Baker*, 2007]. The likelihoods of extreme ECS values are most dramatically affected by the feedback update: the probability of ECS $> 6°$C doubles, while that of ECS $< 2°$C is reduced by 74%.

We conduct sensitivity tests to account for additional sources of uncertainty that may not be captured by the standard deviation of the RCEMIP ensemble. For example, changes in cloud microphysical structure could contribute to the opacity feedback but are not included in our estimate due to model output limitations. Overlap between high and low clouds, some of which is accounted for in our estimate, is another possible source of model bias and feedback uncertainty. To assess the impact of greater feedback uncertainty, we run the ECS calculations for additional feedback values of $N(0.03, 0.16)$ and $N(0.03, 0.20)$ W/m^2/K (Table 3.1). The value of 0.16 W/m^2/K is the maximum deviation of any individual model from the multimodel mean and thus encompasses the full ensemble spread. The value of 0.20 W/m^2/K is the WCRP-assessed uncertainty from [*Sherwood et al.*, 2020], intended to serve as an upper bound. As shown in Table 3.1, changing the feedback uncertainty has little effect on the resulting PDF. This suggests that the shift in the PDF seen in Figure 3.9 arises from the increase in the central estimate of the feedback rather than the reduced uncertainty.

3.7 Discussion

A main takeaway of this work is that changes in tropical ice cloud opacity are a critical part of the cloud response to warming. The possibility of a high cloud opacity feedback has been noted before [*Mauritsen and Stevens*, 2015; *Hartmann*, 2016; *Li et al.*, 2019] but has received comparatively little attention in broader discussions of cloud feedback and ECS. Previous

assessments have often assumed fixed anvil opacity [*Lindzen et al.*, 2001; *Lin et al.*, 2002], perhaps due to the lack of *a priori* expectations for how changes in area would be spread across the distribution of clouds observed in the present-day Tropics. By treating tropical ice clouds as a continuum, this work provides an initial characterization of that response. While our estimate of the combined area and opacity feedback is small, it constitutes a significant increase from the WCRP estimate [*Sherwood et al.*, 2020] and implies a substantial shift in the PDF of ECS.

There are several possible explanations for the disagreement between the RCEMIP-derived feedback estimate and that of the WCRP. The WCRP estimate of $N(-0.20, 0.20)$ W/m^2/K was based on the results of *Williams and Pierrehumbert* [2017], who examined the interannual variability of tropical CRE using CERES satellite measurements and ECMWF reanalysis. We note, however, that we are unsure of the exact methodology used by the WCRP to arrive at a central feedback estimate of -0.2 W/m^2/K, and we have been unable to arrive at that value ourselves. Nevertheless, there are several possible explanations for the disagreement. First, *Williams and Pierrehumbert* [2017] computed CRE as a function of B, a metric of cloud-base buoyancy that is used to identify convectively active regions of the Tropics. The WCRP feedback estimate was based on the T_s-CRE relationship in the parts of the Tropics where $B > 0$, which are taken to be deep convective regions. While

Percentile:	5th	17th	50th	83rd	95th	Mode	Mean
WCRP: $N(-0.2, 0.2)$	2.26	2.55	3.11	3.88	4.70	2.96	3.25
RCEMIP: $N(0.03, 0.06)$	2.44	2.77	3.37	4.23	5.11	3.02	3.52
RCEMIP: $N(0.03, 0.16)$	2.41	2.74	3.35	4.22	5.12	3.01	3.50
RCEMIP: $N(0.03, 0.20)$	2.38	2.72	3.33	4.22	5.13	3.11	3.49

Table 3.1: Percentile values and other statistics (in $^\circ C$) for the posterior PDFs of ECS generated from different feedback values. Statistics are given for the original WCRP feedback estimate and for the RCEMIP-informed estimates, which use different values for the feedback uncertainty.

high ice clouds dominate the cloud distribution in those regions, shallow cumulus are also present and could affect the T_s-CRE relationship in significant ways. It therefore seems likely that other types of clouds were included in the WCRP estimate of the anvil area feedback. Second, studies based on interannual variability are confounded by El Niño-Southern Oscillation variability, which affects the large-scale distribution of convection and may plausibly affect cloud properties. On the contrary, the RCEMIP experiments use uniform changes in T_s. Lastly, our estimate of the feedback does not account for any significant changes in cloud microphysical structure that would have been implicitly included in observations of interannual variability. We stress that these three explanations are speculative, and that there may be other reasons why the WCRP and RCEMIP-based feedback estimates differ.

Extrapolating from RCEMIP to a global mean feedback comes with the caveat that certain atmospheric changes cannot be captured in such idealized simulation setups. For example, our feedback estimate cannot account for warming-induced changes in planetary-scale circulation or dynamical modes of variability, which could affect patterns of convection and cloudiness. However, the RCEMIP CRMs produce a wide range of changes in large-scale convective organization in response to warming [*Wing et al.*, 2020]; these changes freely affect cloud properties and are thus implicitly included in our analysis. We are therefore confident that our estimate spans a wide range of possible changes in large-scale convective dynamics. Furthermore, we have already shown that the CRMs capture the expected reduction in deep convective area in response to warming; this, along with previous work showing that the ensemble-predicted changes in cloud altitude and temperature are consistent with observational and theoretical expectations [*Wing et al.*, 2020; *Stauffer and Wing*, 2022], adds confidence that the most fundamental aspects of the convective response are well represented by the CRMs.

The continuum framework has revealed that thick, climate-cooling and thin, climate-warming clouds are affected differently by changes in T_s. The robust decrease in thick cloud area mirrors expected changes in convective mass flux, whereas the uncertain thin-cloud response appears to be influenced by other factors. In particular, thin clouds with IWP

between 20-70 g/m^2 (τ ∼1-3) are the leading source of uncertainty in changes in ice cloud area and radiative effect. These clouds are known to be shaped by various radiative, dynamic, and microphysical processes that may respond to warming in complex ways [*Gasparini et al.*, 2023]. Constraining these changes is a challenging undertaking that requires consideration of a wide range of physical scales, but such an endeavor may prove critical for understanding tropical climate change.

3.8 Supplementary Information

3.8.1 Calculation of CRE(IWP) and treatment of low clouds

For each column of model output, CRE is computed as the difference between hourly mean all-sky and clear-sky radiative fluxes. We seek to calculate CRE(IWP) such that it reflects the radiative effects of clouds produced by deep convection while excluding the effects of unrelated liquid clouds below. To this end, we first compute the mean CRE of all columns falling within each IWP bin (the "all-cloud" CRE) as well as that of the columns with liquid water path below 1 g/m^2 (the "ice-only" CRE) (Figure 3.10a). Liquid clouds found in low-IWP columns are typically low clouds at the top of the boundary layer, which are unrelated to the overlying ice clouds but nevertheless have an impact on the top-of-atmosphere CRE [*Kang et al.*, 2020]. Therefore, to exclude their radiative effects from CRE(IWP), we set CRE(IWP) equal to the ice-only for IWP $< 10^2$ g/m^2. On the other hand, liquid found in high-IWP columns is typically part of same deep convective cloud as the ice above; we seek to include these liquid effects and therefore set CRE(IWP) equal to the all-sky CRE for IWP $> 10^3$ g/m^2. Between 10^2 and 10^3 g/m^2, we use a transition that is linear with respect to $\log_{10}$IWP (Fig. 3.10a). These thresholds were selected based on the multimodel mean liquid cloud fraction within each IWP bin (Figure 3.10b), which increases rapidly within this range, signaling a shift from low clouds unrelated to the high clouds above to deep convective clouds occupying a large portion of the atmospheric column. Our results are not sensitive to the details of this transition, and the multimodel mean CRE(IWP) for T_s=295 K changes

sign at ∼200 g/m^2 (τ ∼4-5) , which is consistent with previous analyses [*Hong et al.*, 2016; *Berry and Mace*, 2014; *Kubar et al.*, 2007].

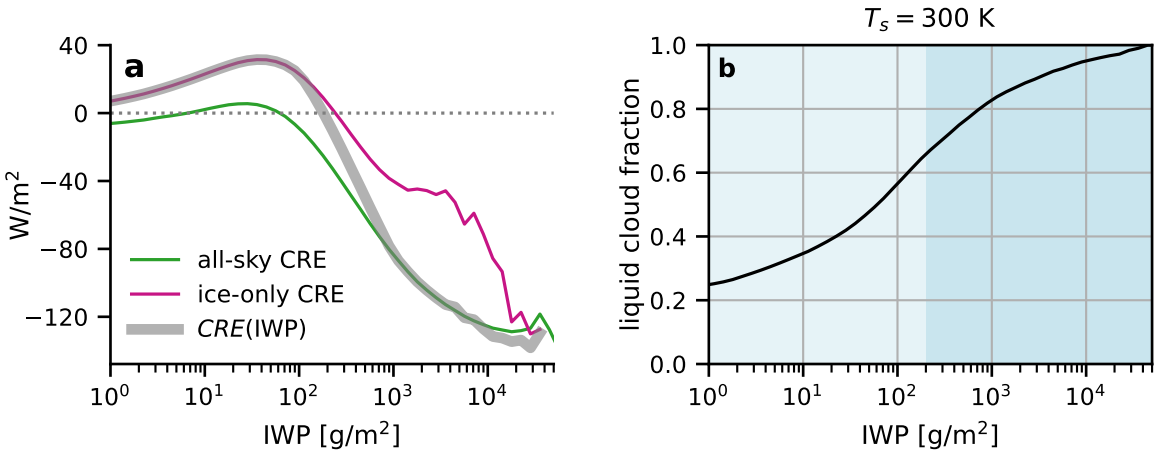

Figure 3.10: **(a)** Multimodel mean *CRE* computed three different ways, as described in the text. **(b)** Multimodel mean liquid cloud fraction as a function of IWP for the 300-K run. A column is determined to contain liquid cloud if the liquid water path exceeds 1 g/m^2.

3.8.2 Tables

Model	f_{ice}	f_{thin}	f_{thick}	C_{ice}	C_{thin}	C_{thick}	$\overline{CRE}$
			$T_s = 295$ K				
SAM-CRM	0.2273	0.1960	0.0313	-1.3452	1.3769	-2.7220	-5.9175
DAM	0.3093	0.2477	0.0616	5.5146	6.1598	-0.6451	17.8271
UCLA-CRM	0.1916	0.1638	0.0278	1.6927	3.3738	-1.6810	8.8362
SCALE	0.2053	0.1763	0.0290	4.4638	4.7173	-0.2535	21.7375
WRF-COL-CRM	0.4048	0.3389	0.0660	-3.1959	2.9234	-6.1193	-7.8940
CM1	0.3634	0.3145	0.0489	4.5477	5.0635	-0.5158	12.5134
SAM-P3	0.3228	0.2808	0.0421	-1.3681	4.3847	-5.7529	-4.2378
ICON-NWP	0.4380	0.3669	0.0710	10.8685	13.6368	-2.7683	24.8167
ICON-LEM	0.4371	0.3920	0.0451	10.6213	12.3052	-1.6839	24.3001
UKMO-RA1-T	0.2631	0.2206	0.0425	0.1170	3.9020	-3.7850	0.4447
MESONH	0.6012	0.5371	0.0641	4.6222	7.8594	-3.2372	7.6885
Mean	0.3422	0.2941	0.0481	3.3217	5.9730	-2.6513	9.1013
St. Dev.	0.1175	0.1064	0.0148	4.4591	3.6782	1.8951	11.6571
			$T_s = 300$ K				
SAM-CRM	0.2018	0.1767	0.0251	0.0298	2.0116	-1.9819	0.1475
DAM	0.2948	0.2402	0.0545	5.6431	6.0633	-0.4202	19.1426
UCLA-CRM	0.1944	0.1678	0.0266	2.2951	3.6245	-1.3294	11.8078
SCALE	0.2090	0.1846	0.0244	4.3751	4.6433	-0.2683	20.9309
WRF-COL-CRM	0.4060	0.3452	0.0607	-1.2774	3.6637	-4.9411	-3.1466
CM1	0.3412	0.2967	0.0446	4.2264	4.6043	-0.3779	12.3855
SAM-P3	0.2778	0.2386	0.0392	-1.1071	4.0657	-5.1728	-3.9850
ICON-NWP	0.5514	0.5013	0.0501	17.4096	18.7798	-1.3702	31.5761
ICON-LEM	0.4569	0.4152	0.0417	11.7734	12.9995	-1.2260	25.7671
UKMO-RA1-T	0.1878	0.1552	0.0326	0.3212	3.2015	-2.8804	1.7101
MESONH	0.4515	0.4000	0.0515	4.2143	6.9136	-2.6993	9.3332
Mean	0.3248	0.2838	0.0410	4.3549	6.4155	-2.0607	11.4245
St. Dev	0.1203	0.1117	0.0120	5.4601	4.8018	1.6379	11.4356
			$T_s = 305$ K				
SAM-CRM	0.2010	0.1782	0.0227	0.4525	2.3056	-1.8531	2.2518
DAM	0.3102	0.2617	0.0485	3.0872	3.5621	-0.4749	9.9517
UCLA-CRM	0.2182	0.1927	0.0256	3.5113	4.6452	-1.1339	16.0896
SCALE	0.1769	0.1553	0.0216	4.1445	4.4591	-0.3146	23.4286
WRF-COL-CRM	0.3860	0.3295	0.0565	-0.2437	4.0894	-4.3331	-0.6313
CM1	0.2664	0.2325	0.0338	3.4477	3.7547	-0.3070	12.9441
SAM-P3	0.3247	0.2911	0.0337	1.2244	5.3036	-4.0792	3.7707
ICON-NWP	0.5301	0.4871	0.0430	14.9193	15.8377	-0.9184	28.1420
ICON-LEM	0.4809	0.4451	0.0357	13.1020	14.0538	-0.9518	27.2471
UKMO-RA1-T	0.1410	0.1133	0.0277	-0.4999	2.1195	-2.6194	-3.5462
MESONH	0.5833	0.5266	0.0567	7.4853	10.0338	-2.5485	12.8337
Mean	0.3290	0.2921	0.0369	4.6028	6.3786	-1.7758	12.0438
St. Dev	0.1423	0.1334	0.0121	4.9559	4.5164	1.3808	10.4886

Table A3.1. Values of select quantities for the individual models in the RCEMIP CRM ensemble. All f values are unitless. All C values and $\overline{CRE}$ are in W/m^2.

Model	Δf_{ice}	Δf_{thin}	Δf_{thick}	$\Delta_f C_{\text{ice}}$	$\Delta_f C_{\text{thin}}$	$\Delta_f C_{\text{thick}}$	Area	Opacity	Global
SAM-CRM	-0.0026	-0.0018	-0.0009	0.0772	-0.0045	0.0816	0.0156	0.0616	0.0257
DAM	0.0001	0.0014	-0.0013	0.0119	-0.0056	0.0175	0.0016	0.0104	0.0040
UCLA-CRM	0.0027	0.0029	-0.0002	0.0748	0.0606	0.0142	0.0236	0.0512	0.0249
SCALE	-0.0028	-0.0021	-0.0007	-0.0792	-0.0856	0.0065	-0.0618	-0.0173	-0.0264
WRF-COL-CRM	-0.0019	-0.0009	-0.0009	0.0857	-0.0075	0.0932	0.0149	0.0708	0.0285
CM1	-0.0097	-0.0082	-0.0015	-0.1382	-0.1526	0.0144	-0.1215	-0.0168	-0.0460
SAM-P3	0.0002	0.0010	-0.0008	0.1361	0.0329	0.1031	-0.0008	0.1368	0.0453
ICON-NWP	0.0092	0.0120	-0.0028	0.5671	0.4334	0.1337	0.2288	0.3383	0.1888
ICON-LEM	0.0044	0.0053	-0.0009	0.2249	0.1825	0.0424	0.1064	0.1186	0.0749
UKMO-RA1-T	-0.0122	-0.0107	-0.0015	-0.0799	-0.2011	0.1212	-0.0054	-0.0745	-0.0266
MESONH	-0.0018	-0.0011	-0.0007	0.0908	0.0452	0.0455	-0.0138	0.1046	0.0302
Median	-0.00180	-0.00090	-0.00090	0.07720	-0.00450	0.04550	0.00160	0.06160	0.02570
Mean	-0.00131	-0.00020	-0.00111	0.08829	0.02706	0.06121	0.01705	0.07125	0.02939
St. Dev.	0.00570	0.00583	0.00065	0.18191	0.16266	0.04467	0.08544	0.10445	0.06056

Table A3.2. Values of select quantities for individual models. All values correspond to absolute changes between the 295- and 305-K simulations, normalized by ΔT_s. Δf values are in 1/K and all other values are in W/m^2/K. "Area" and "Opacity" refer to the area and opacity components of $\Delta_f C_{\text{ice}}$. "Global" refers to the global mean feedback, which is computed from $\Delta_f C_{\text{ice}}$ as described in the text. Note that Δf_{ice}, Δf_{thin} and Δf_{thick} shown here differ from the values shown in Fig. 3.5b, which are fractional changes.

Chapter 4

CONVECTIVE AGGREGATION AND THE CONGESTUS MODE OF TROPICAL CONVECTION

This work was published as: Sokol, A. B. and D. L. Hartmann (2022). Congestus mode invigoration by convective aggregation in simulations of radiative-convective equilibrium. *Journal of Advances in Modeling Earth Systems, 14*(7). doi.org/10.1029/2022MS003045.

4.1 Introduction

Convection in the tropical atmosphere is known to be trimodal [*Johnson et al.*, 1999]. The first and dominant mode is deep convection, marked by towering cumulonimbus clouds extending from the boundary layer to the tropopause. Deep convection is typically front and center in conceptual models of the tropical circulation because of its close relationship to the Hadley and Walker circulations, which play an important role in global climate. The second mode is shallow convection, which produces shallow cumulus clouds (also called trade wind cumulus) at the top of the boundary layer. The final mode, the congestus mode, describes convection that reaches the mid-troposphere. Congestus cloud tops are typically found in the vicinity of the freezing level, distinctly between shallow and deep cumulus. This third mode is the primary focus of this chapter.

In previous work, the term *shallow* has often been used to refer to any convective feature that is distinct from the deep mode. But such features could be either shallow or congestus in nature; to avoid this ambiguity, we refer to features as *shallow* if they are restricted to pressures greater than 750 hPa and *congestus* if their upper extent lies between 400 and 750 hPa.

The three modes of tropical convection were first recognized by *Johnson et al.* [1999] in

the observed distribution of clouds over tropical oceans. However, overturning circulations observed in the tropics or derived from global wind reanalyses have generally been only bimodal, with a deep mode and a second mode that is either shallow, congestus, or something in between [*Zhang et al.*, 2004, 2008; *Schulz and Stevens*, 2018; *Chen and Yu*, 2021; *Trenberth et al.*, 2000]. There are several possible explanations for this discrepancy. It could be the case that the three modes are not expressed simultaneously, or that the shallow and congestus modes fuse together when averaged over large regions or periods of time. It could also be the case that the relatively fine structures of the shallow mode are not well resolved in reanalyses. Or, perhaps the shallow and congestus modes of convection simply do not translate into distinct modes of the tropical overturning circulation due to interference from other dynamical factors.

The situation is somewhat different in model simulations of radiative-convective equilibrium (RCE), in which each mode of convection is associated with a closed overturning circulation. This is because traditional "RCE-in-a-box" simulations, unlike the real tropics, have no mean large-scale vertical motion, so all convective detrainment must be compensated for by subsidence at the same vertical level. Many model simulations successfully capture the trimodal character of convection [*Bretherton et al.*, 2006; *Posselt et al.*, 2008; *Muller and Held*, 2012; *Holloway and Woolnough*, 2016; *Beydoun and Hoose*, 2019; *Chen and Wu*, 2019], but others produce just two modes [*Grabowski et al.*, 2000; *Nolan et al.*, 2007; *Arnold and Putman*, 2018]. The congestus mode is especially fickle but has received little attention compared to the deep and shallow modes. Our primary goal here is to better understand the variability and sensitivities of the congestus mode in simulated RCE.

Previous work has provided valuable insight into the nature of congestus overturning. *Yano et al.* [2002] argued that cloud-resolving models (CRMs) develop congestus-like circulations (what they refer to as "shallow double-cell" circulations) because the deep circulation is linearly unstable when the model domain is a few thousand kilometers in length. The deviation of model temperature profiles from the real atmosphere has also been implicated [*Grabowski et al.*, 2000]. Others have described congestus convection as a precursor to deep

convection that imports moist static energy until the latent heating is strong enough to support deep updrafts [*Wu*, 2003; *Masunaga and L'Ecuyer*, 2014; *Chen and Yu*, 2021]. Additionally, congestus clouds have long been associated with mid-tropospheric stable layers, which are thought to inhibit the vertical development of convection by reducing updraft buoyancy and promoting midlevel detrainment. These stable layers have been attributed to various causes, including: latent cooling associated with the melting of frozen precipitation from stratiform clouds [*Mapes and Houze*, 1995; *Johnson et al.*, 1996; *Yasunaga et al.*, 2006]; evaporative cooling of detrained liquid condensate and subsequent radiative cooling [*Posselt et al.*, 2008; *Nuijens and Emanuel*, 2018]; and the radiative [*Mapes and Zuidema*, 1996] and microphysical [*Zuidema et al.*, 2006] responses to dry air intrusions. This previous work suggests that careful consideration of moisture, radiative transfer, and static stability is necessary in order to fully understand how the congestus mode is expressed in cloud-resolving RCE.

The apparent linkages to moisture and static stability also beg the question of how the congestus mode is affected by the large-scale self-aggregation of convection (*aggregation* for brevity). Aggregation describes the process by which convection spontaneously organizes into distinct regions characterized either by mean ascent (the *moist* or *convecting* regions) or by radiatively driven subsidence (the *dry* or *nonconvecting* regions). The convecting and nonconvecting regions correspond to the rising and subsiding branches, respectively, of the convectively coupled circulation modes. Aggregation affects the mean RCE climate in several important ways, two of which will be especially relevant throughout this chapter. First, the troposphere becomes warmer and more stable [*Held et al.*, 1993; *Bretherton et al.*, 2005; *Wing and Cronin*, 2016]. Because stable layers are thought to promote congestus-level detrainment, we may *a priori* expect the congestus circulation to strengthen in response to aggregation. Second, the troposphere becomes drier on average as the dry, nonconvecting regions grow to occupy a large fraction of the horizontal area [*Bretherton et al.*, 2005]. Dryness aloft allows for strong radiative cooling at the top of the moist boundary layer in nonconvecting regions, which is thought to play an important role in driving shallow circulations [*Nigam*, 1997;

Bretherton et al., 2005; *Nishant et al.*, 2016; *Naumann et al.*, 2017, 2019]. These shallow circulations have been shown to support aggregation by transporting moist static energy up-gradient from nonconvecting to convecting regions [*Bretherton et al.*, 2005; *Muller and Held*, 2012; *Muller and Bony*, 2015; *Schulz and Stevens*, 2018]. Despite extensive study of convective aggregation, its impact on congestus circulations has, to our knowledge, not been investigated.

This chapter explores three different aspects of the congestus mode in cloud-resolving RCE. First, we seek to understand its intermodel variability. To do so, we examine the circulation structures produced by the ensemble of CRMs participating in the Radiative-Convective Equilibrium Model Intercomparison Project [RCEMIP; *Wing et al.*, 2018]. Beyond contributing to the ongoing exposition of RCEMIP results, which is valuable in its own right, this analysis will illustrate that different models produce very different RCE circulations even when the experimental configurations are identical. It will also show that stronger congestus circulations are associated with higher degrees of convective aggregation and greater tropospheric stability.

Second, we ask why the congestus circulation is invigorated by convective aggregation. This question is difficult to answer using the RCEMIP ensemble, since the RCEMIP models differ in countless ways. We overcome this difficulty by performing a new set of idealized, two-dimensional RCE simulations that use a single model but span a wide range of aggregation states, which offers a more compelling account of the relationship between aggregation, congestus strength, and static stability. In this new ensemble, aggregation invigorates the congestus circulation at the expense of the shallow circulation. We will show that the congestus circulation is subject to a positive feedback involving vertical gradients of moisture and radiative cooling. An additional simulation with prescribed radiative cooling will show that this feedback is central to congestus invigoration, whereas greater tropospheric stability is not necessary.

Lastly, we investigate why the troposphere is more stable when convection is aggregated. This will show that congestus invigoration is a cause, rather than a consequence, of en-

hanced stability. Previously identified sources of enhanced stability are also found to play an important role.

In section 4.2, we describe the RCEMIP model output, explain the transformation to "moisture space" used to characterize atmospheric circulations, and discuss the RCEMIP results. In section 4.3, we introduce the new, 2D simulations and investigate the causes of congestus invigoration. Section 4.4 focuses on static stability, its dependence on aggregation, and its relationship to the congestus mode. In section 4.5, we summarize and discuss our results.

4.2 Circulation variability in the RCEMIP CRM ensemble

4.2.1 Simulations and Output

The RCEMIP simulation protocol is described in *Wing et al.* [2018]. We use output from the "RCE_large300" CRM runs obtained from the public RCEMIP repository hosted by the German Climate Computing Center. We refer to the different models using the same naming conventions as in *Wing et al.* [2020]. There are twelve CRMs for which full RCE_large300 output is available at the time of writing; all are included in our analysis with the exception of the UKMO-RA1-T-nocloud simulation, which differs from the UKMO-RA1-T run (which we include) only in that that sub-grid cloud scheme is disabled.

The RCE_large300 simulations use a domain size of ∼6000 km × ∼400 km, a horizontal grid spacing of 3 km, and a uniform sea surface temperature (SST) of 300 K. There is no rotation. Each model run was integrated for at least 100 days. Our analysis uses the last 25 days of each simulation, for which instantaneous 3D output is available at six-hour intervals. An exception to these specifications is the DAM model, which has 2.5-km horizontal grid spacing and 3D output available at 24-hour intervals. The RCEMIP CRMs use a variety of vertical coordinates. To facilitate comparison across models, we convert all output to pressure coordinates by taking the time- and domain-averaged pressure at each vertical level.

In addition to the 11 RCEMIP simulations, we conduct a new, RCEMIP-style run using

the System for Atmospheric Modeling [SAM; *Khairoutdinov and Randall*, 2003] with the Predicted Particle Properties (P3) microphysics scheme [*Morrison and Milbrandt*, 2015] and RRTM radiation [*Iacono et al.*, 2000; *Mlawer et al.*, 1997]. We will refer to this run as SAM-P3 to distinguish it from the RCEMIP SAM-CRM run, which uses a different microphysics scheme. The SAM-P3 run uses a 6144×384-km^2 domain. All other specifications (horizontal resolution, vertical grid, insolation, trace gases, etc.) follow the RCEMIP protocol for RCE_large300 simulations.

4.2.2 Transformation to Moisture Space

We will examine atmospheric circulations in "moisture space", as has been done in the past [e.g. *Bretherton et al.*, 2005; *Holloway and Woolnough*, 2016; *Schulz and Stevens*, 2018; *Beydoun and Hoose*, 2019]. In this approach, vertical columns of the atmosphere are rearranged and binned according to some measure of column-integrated moisture; here, we use the column relative humidity (CRH) percentile. Because horizontal temperature gradients are weak in the tropics [*Sobel et al.*, 2001], CRH corresponds closely to the column-integrated moist static energy. We use all of the model output from the 25-day compositing period to compute the mean atmospheric state as a function of CRH percentile. The result is a transformation of the modeled atmosphere from four dimensions (x, y, p, t) to two (CRH percentile, p). The circulations that emerge from this transformation reflect the exchange of mass between moist regions typically associated with convection and dry regions associated with subsidence.

For each simulation, we begin by computing CRH for each atmospheric column at every time step in the 25-day compositing period for which 3D output is available. CRH is computed from the 2D output as the ratio of the column-integrated water vapor to the saturation column-integrated water vapor. The calculation of saturation vapor pressure is not specified in the RCEMIP protocol and therefore varies from model to model. CRH percentiles are then assigned to each grid cell at each time step; the percentiles are computed relative to the entire set of CRH values for the 25-day compositing period, as opposed to the values from

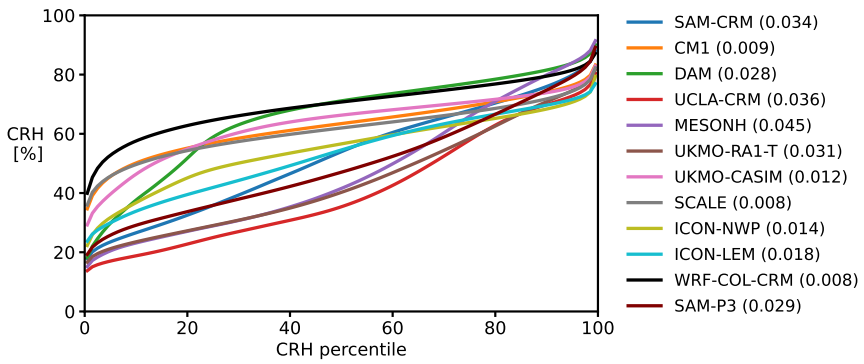

Figure 4.1: CRH percentiles for the RCEMIP CRMs (RCE_large300 simulation). The CRH variance σ^2_{CRH} for each model is given in parentheses.

each individual time step. The grid cells are then sorted by CRH percentile into 100 equally sized bins, with each bin thus representing 1% of the domain area over time.

Figure 4.1 shows the CRH percentiles for each of the RCEMIP models. Differences in the curves reflect intermodel differences in how moisture is distributed across the domain, which are closely related to differences in the degree of convective aggregation. In this chapter, we quantify the degree of aggregation using the spatial and temporal variance of CRH (σ^2_{CRH}), which has been used by others in the past [*Wing et al.*, 2020]. We prefer this metric because it is simple and physically intuitive within the moisture space context. Fig. 4.1 shows that the models are tightly clustered when it comes to the CRH in the moistest part of the domain. The intermodel spread is much larger in the driest regions, suggesting that σ^2_{CRH} is determined primarily by how dry the dry regions become.

Following *Schulz and Stevens* [2018], we compute the mass streamfunction Ψ (kg m^{-2} s^{-1}) in pressure coordinates as

$$\Psi_i(p) = \Psi_{i-1}(p) + \frac{\alpha}{g}\omega_i(p) \tag{4.1}$$

where i is the CRH percentile bin rank (1-100) and $\Psi_0(p) = 0$. ω is the bin-averaged vertical velocity in pressure coordinates, g is the acceleration due to gravity, and $\alpha = 0.01$ is the

fraction of total grid boxes contained in the i-th bin. The algebraic sign of Ψ is such that flow is counterclockwise around Ψ maxima and clockwise around Ψ minima in all subsequent figures.

From Ψ, we can compute the horizontal velocity in moisture space, v, as

$$v_i(p) = -g\frac{\partial \Psi_i(p)}{\partial p}. \tag{4.2}$$

v represents the horizontal exchange of mass between CRH percentile bins. It has unconventional units of time^{-1} because, in moisture space, "distance" is measured as a dimensionless fraction of the domain area. We have chosen these particular formulations of Ψ and v because they are independent of domain size, which varies slightly across the RCEMIP ensemble for computational reasons. They are also easily applicable in both two and three dimensions, allowing us to use the same formulations in our analysis of the 2D ensemble in section 4.3.

In moisture space, we quantify the strength of the congestus circulation asv_{cong}, equal to the 400-750-hPa mass average of the negative values of v at the 50th CRH percentile. The 400-750 range was chosen because it excludes outflow associated with the deep and shallow circulations but captures the range of congestus detrainment heights produced by the different simulations. If v is positive throughout this entire range, as it is in two of the RCEMIP models (SCALE and WRF-COL-CRM), v_{cong} is set to zero. More negative values of v_{cong} indicate stronger congestus-level flow from high to low CRH and thus a stronger congestus circulation.

4.2.3 Circulation

Streamfunctions (Ψ) for the RCEMIP models are shown in Figure 4.2a. While there is clearly great diversity among the models, there are some common features to note. All models produce a dominant deep circulation that extends from the lower troposphere to ∼200 hPa. The rising branches of the deep cells are confined to the top few CRH percentiles, meaning that the upward convective mass flux is concentrated within a small horizontal area. A

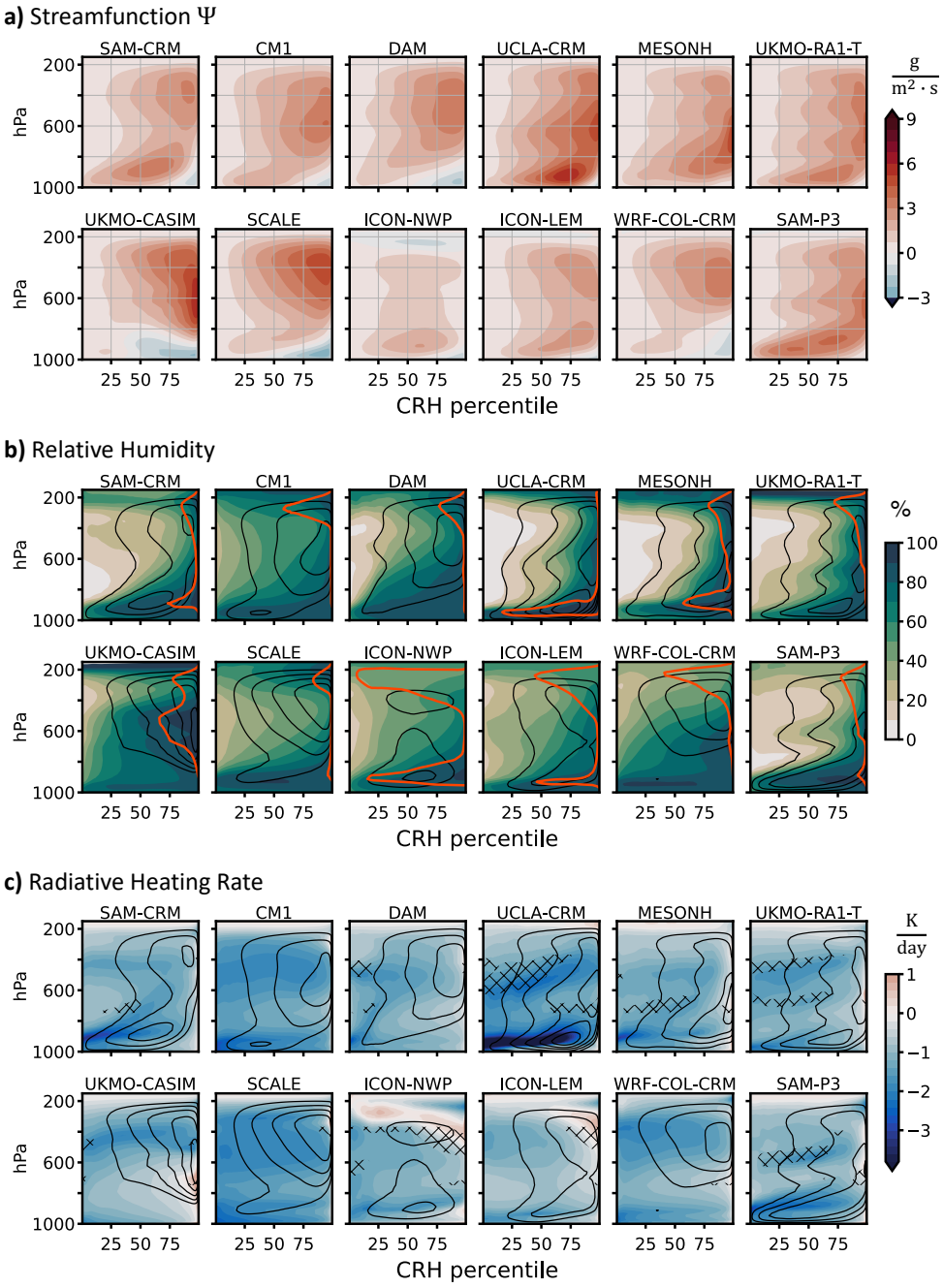

Figure 4.2: (**a**) Streamfunction Ψ, (**b**) relative humidity, and (**c**) radiative heating rate in moisture space for the RCEMIP CRMs. The black contours in (**b**) and (**c**) show Ψ and have a spacing of 1 g m^{-2} s^{-1} (the outermost contour is 1 g m^{-2} s^{-1}). Flow is counterclockwise around Ψ maxima. The orange contour in (**b**) indicates a cloud fraction of 0.1 using a cloud condensate threshold of 10^{-5} kg kg^{-1}. The hatching in (**c**) shows where the radiatively driven divergence D_{rad} exceeds 0.05 day^{-1}; hatching is only shown between 350 and 750 hPa. Note: While not visible, Ψ goes to zero at the highest CRH percentile.

majority of the models have negative Ψ near the surface in the top few CRH percentiles, which is the signature of below-cloud downdrafts driven by the evaporative cooling of rain (i.e., cold pools).

The deep circulation in ICON-NWP is unique in several ways. First, the rising branch extends to much lower CRH percentiles than in the other runs. This does not mean that updrafts occupy a larger fraction of the domain (they do not), but that ω is not tightly linked to CRH in ICON-NWP. Second, the deep overturning circulation is weak compared to those in the other models. This is consistent with the previous finding that the integrated, atmospheric radiative cooling rate is smaller in ICON-NWP than in any other RCEMIP model, including the general circulation models (see R_{Net} in Table A2 in Wing el al., 2020). The weak atmospheric cooling is partially due to especially high cloud fraction in the upper troposphere (Fig. 4.2b). The ubiquitous high clouds are also responsible for the distinct circulation cell between 150-300 hPa that flows in the opposite direction as the deep cell, with ascent in dry regions and subsidence in moist regions. This circulation is driven by cloud radiative effects, which heat the upper troposphere at low CRH and cool it at high CRH(Fig. 4.2c).

Shallow circulations centered near the top of the boundary layer are present in a majority of the models. As one would expect from previous work, the models with strong shallow circulations are generally those with strong radiative cooling at the top of the dry-region boundary layer (Fig. 4.2c). This cooling is remarkably strong in UCLA-CRM due to the combination of high humidity and cloud fraction within the boundary layer and low humidity immediately above.

The most notable difference between the model circulations is the representation of the congestus mode. In the moisture-space framework, the clearest marker of the congestus circulation is its upper branch, which manifests as a layer of moist-to-dry outflow (negative v) in the mid-troposphere. UCLA-CRM and SAM-P3 produce distinct congestus cells with outflow between 400-600 hPa (Fig. 4.2a). MESONH also has a trimodal circulation with lower outflow layers at 400-500 and 650-800 hPa. UKMO-CASIM and DAM both have weak con-

gestus outflow layers, although in DAM the flow is restricted to low CRH percentiles, which suggests that it may not originate from surface-based convection. Interestingly, UKMO-RA1-T produces a circulation with four distinct cells, the middle two of which have outflow in the congestus range. The remaining models produce bimodal circulations without a congestus cell.

When present, the congestus circulation has a large impact on relative humidity (RH; Fig. 4.2b) and radiative cooling (Fig. 4.2c). Congestus outflow layers are associated with plumes of moisture extending from the convective regions into the nonconvective regions, which tend to be drier in the runs with strong congestus cells. As the moist outflow travels away from its convective source, the atmosphere above it becomes increasing dry, and a strong vertical gradient in RH develops at the top of the outflow layer. The sharp drop-off in RH with height allows for strong radiative cooling, which causes the layer to gradually subside as it moves further from convection. This structure is most evident in UCLA-CRM, UKMO-RA1-T, and SAM-P3.

The sharp vertical gradients in RH and radiative cooling are similar in many respects to those thought to induce shallow circulations at the top of the boundary layer [*Bretherton et al.*, 2005; *Naumann et al.*, 2017]. It is easy to envision an analogous mechanism acting as a positive feedback on congestus detrainment. Because horizontal temperature gradients in tropical RCE are weak, the dominant thermodynamic balance in the free troposphere in nonconvective regions is that between radiative cooling and subsidence warming. The rate of subsidence needed to exactly balance radiative cooling is $\omega_{\text{rad}} = Q_{\text{rad}}/s$, where Q_{rad} is the radiative cooling rate and s the static stability. In nonconvective regions, where radiative cooling is the principal diabatic process, ω_{rad} is a good approximation of mean ω. Vertical gradients in ω_{rad} produce radiatively driven divergence

$$D_{\text{rad}} = \frac{\partial}{\partial p}\omega_{\text{rad}}. \tag{4.3}$$

To satisfy mass continuity, radiatively driven divergence in nonconvective regions must be

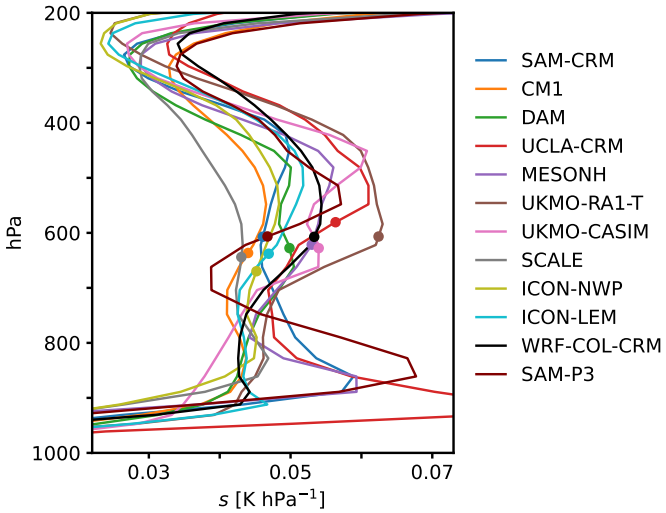

Figure 4.3: Domain-averaged static stability s for each RCEMIP CRM. Dots indicate the freezing level for each run.

filled by horizontal outflow from convective regions at the same vertical level. These outflow plumes undergo strong cooling, which generates radiatively driven divergence and, in turn, leads to more congestus outflow. We will refer to this as the *radiative-divergence feedback*.

The hatching in Fig. 4.2c indicates D_{rad} in excess of 0.05 day^{-1}. While every model produces widespread divergence above 300 hPa associated with the deep mode, hatching is only shown between 350-750 hPa for clarity. About half of the models have notable divergence within this pressure range. In the two ICON models, the divergence is associated with cloud radiative heating. In the others, it is coincident with the top of the congestus outflow layer, where the radiative cooling rate rapidly decreases with height. This shows that the patterns of radiative cooling produced by congestus detrainment are qualitatively consistent with the radiative-divergence feedback mechanism.

4.2.4 Static Stability and Aggregation

As previously discussed, static stability may also play an important role in congestus dynamics. Figure 4.3 shows the mean static stability for each RCEMIP model, which in pressure

	σ^2_{CRH}	$v_{\text{cong}}{}^a$	s^b	$D_{\text{rad}}{}^c$
σ^2_{CRH}	1.00	-0.82	0.52	0.84
$v_{\text{cong}}{}^a$	-0.82	1.00	-0.63	-0.81
s^b	0.52	-0.63	1.00	0.66
$D_{\text{rad}}{}^c$	0.84	-0.81	0.66	1.00

[a] v_{cong} decreases with increasing congestus strength
[b] 400-600-hPa mean.
[c] 400-750-hPa and 1-50th-CRH percentile mean.

Table 4.1: Correlation coefficients for measures of convective aggregation (σ^2_{CRH}), congestus strength (v_{cong}), midlevel stability (s), and radiatively driven divergence (D_{rad}) across the RCEMIP CRM ensemble.

coordinates is given by

$$s = -\frac{T}{\theta}\frac{\partial \theta}{\partial p} \tag{4.4}$$

All of the models produce relative maxima somewhere between 400-650 hPa. In a few of the models, the maxima are located very close to the freezing level (indicated by the colored dots), suggesting that they are directly related to microphysical phase transitions. In the other models, the maxima are generally located above the freezing level. Apart from large differences in stability at the top of the boundary layer, the intermodel spread is greatest near the midlevel maxima. This is likely due to differences in entrainment and microphysical processes between the models, which may in turn be related to the degree of convective aggregation. Vertical gradients in Q_{rad} may also contribute to the spread in stability, as will be discussed in section 4.4. There is much better model agreement in the upper troposphere (250-400 hPa), where water vapor is scarce and the lapse rate is constrained to be close to the dry adiabatic limit.

We turn now to the question of how stability, aggregation, and congestus strength covary across the RCEMIP ensemble. Correlation coefficients for these three factors, along with the midlevel D_{rad} in nonconvective regions, are provided in Table 4.1.

As expected from previous work, aggregation is generally associated with greater midlevel

stability. But σ^2_{CRH} explains only about a quarter of the variance in stability (r^2=0.52^2=0.27), suggesting that other factors are just as important. This is not particularly surprising; the many differences in model physics across the RCEMIP ensemble will impact the stability in a variety of ways, which limits the explanatory power of any single quantity such as σ^2_{CRH}.

Congestus strength is generally associated with greater aggregation and midlevel stability. Our *a priori* reasoning was that aggregation could invigorate the congestus circulation precisely through its impacts on stability. Therefore, it is somewhat surprising that v_{cong} is more tightly linked to σ^2_{CRH} than to s (Table 4.1). This alone does not dismiss the importance of stability, but it does invite us to consider alternative explanations for why the congestus circulation strengthens with aggregation.

One such explanation may be the radiative-divergence feedback identified in the previous section. Congestus-level D_{rad} and v_{cong} are strongly correlated across the RCEMIP ensemble, which is to be expected from basic mass continuity constraints. Less obvious is the strong relationship between D_{rad} and σ^2_{CRH}, which we may expect now given both variables' relationships with v_{cong} but which we did not expect *a priori*. These results raise the possibility that congestus invigoration is caused not by increasing stability but rather by the activation of the radiative-divergence feedback. If this is the case, the relationship between stability and v_{cong} may simply reflect underlying changes in aggregation rather than a causal link; this relationship will be revisited in section 4.4.

We have now identified two possible mechanisms of congestus invigoration: the stability mechanism—in which increasing stability with aggregation reduces updraft buoyancy and promotes congestus-level detrainment—and the radiative-divergence mechanism, in which aggregation activates the radiative-divergence feedback. This leaves us with two important questions: How, physically, does aggregation affect the radiative-divergence feedback? And what is the relative importance of the two mechanisms? It is difficult to pursue these questions further using the RCEMIP output, since the output variables are limited and the various relationships in question are complicated by myriad differences in model physics. For these reasons, we turn now to the new ensemble of 2D simulations.

4.2.5 Summary

- Some RCEMIP CRMs simulate trimodal convection, while others produce bimodal convection. One model produces a circulation with four modes.

- Through its impacts on moisture and radiative cooling, the congestus circulation is subject to a positive feedback (the radiative-divergence feedback).

- Aggregation is associated with congestus invigoration and with midlevel increases in stability and radiatively driven divergence.

4.3 Congestus invigoration in two-dimensional RCE

4.3.1 Model Simulations

Our goal with the new 2D simulations is to examine the relationship between aggregation, stability, and congestus strength in the absence of other changes in model physics. To do this, we will use a single model (SAM) and microphysics scheme (P3) to generate a range of equilibria with varying degrees of aggregation and tropospheric stability. The two-dimensional domain makes the runs computationally efficient and allows us to simulate a large number of aggregation states.

The control run is a normal RCE run with uniform 300-K SSTs. In the other runs, we apply small adjustments to the model physics or configuration that are thought to impact aggregation and stability in some way. The adjustments are listed in Table 4.2. With the exception of the control run, each simulation uses a unique combination of up to three adjustments. There are 20 runs in total.

This experimental approach allows us to interpret ensemble trends with confidence. On their own, each model adjustment may introduce confounding factors that would make it difficult to interpret changes in congestus strength. But any physical relationships gathered from the full ensemble of simulations are unlikely to be spurious, since the adjustments target completely different parts of the model setup and code. The full ensemble thus constitutes a

Notation	Description	Intended Effect
u0	Domain-averaged horizontal wind is nudged to zero on a one-hour timescale	promote aggregation[a]
SSTa1	Sinusoidal SST distribution (299 K at domain edges and 301 K in the center with a mean of 300 K)	promote aggregation since convection clusters over the warmest SSTs[b]
sfchomo	Interactively computed surface fluxes are horizontally homogenized to the domain average at each time step	inhibit aggregation[c]
radhomo	Interactively computed radiative heating rates are horizontally homogenized to the domain average at each time step	inhibit aggregation[c]
noacre	Cloud radiative effects are turned off.	inhibit aggregation[d]
5xVT	The fall speed of rain is multiplied by a factor of 5 to shorten the residence time of rain in the atmosphere and reduce evaporative cooling	promote aggregation by inhibiting the formation of cold pools[e]
5xACC	The rate of accretion of cloud droplets by rain is multiplied by a factor of 5 to decrease cloud droplet residence time	inhibit stable layer formation due to cloud droplet evaporation[f]
nomelt	Ice cannot melt; it must either sublimate (which can only occur at $T < 273.15$ K) or fall to the surface	inhibit stable layer formation due to melting[g]
RADCAM	Uses the radiation scheme from the Community Atmosphere Model 3[h] rather than RRTM	provide another possible climate realization

[a] *Held et al.* [1993]. [b] *Lindzen and Nigam* [1987]. [c] *Bretherton et al.* [2005]. [d] *Pope et al.* [2021]
[e] *Jeevanjee and Romps* [2013]. [f] *Posselt et al.* [2008]. [g] *Mapes and Houze* [1995]. [h] *Collins et al.* [2004].

Table 4.2: Model adjustments used in the 2D simulation ensemble

powerful tool for addressing our scientific questions. Moreover, it is not important whether each adjustment actually achieves its intended effect listed in Table 4.2, so long as the full ensemble encompasses a range of aggregation states.

Apart from the various adjustments, all other aspects of the 2D simulations follow the RCEMIP protocol. The domain is 5,832 km long with 3-km horizontal resolution. For computational reasons, the vertical grid excludes the uppermost two levels of the standard RCEMIP grid. The runs are initialized with an equilibrium sounding from a 3D RCE run with 300-K SSTs and are integrated for 150 days, with full instantaneous output collected every 3 hours. The final 60 days of each run are used to perform the transformation to

moisture space described in section 4.2.2. In some of the subsequent figures, results are shown for each individual run; in others, we split the 2D ensemble into terciles based on σ^2_{CRH} and compute averages for each tercile. The most and least aggregated terciles contain 7 runs each, while the middle tercile contains 6.

4.3.2 Circulation and Mean Climate

The various model adjustments used in the 2D runs successfully produce a range of aggregation states (Figs. 4.9 and 4.10), and the ensemble captures several known impacts of aggregation on mean climate. These trends are illustrated in Figure 4.4, in which the color of each line corresponds to degree of aggregation (red is high σ^2_{CRH}). Aggregation is associated with tropospheric warming (Fig. 4.4a), greater midlevel stability (4.4b), lower mean RH (4.4c), and reduced high cloud fraction (4.4d). The profiles shown in Fig. 4.4 are domain averages; Figures 4.12-4.16 show the complete distributions of RH, Q_{rad}, static stability, cloud fraction, and D_{rad} in moisture space.

The circulation response to aggregation can be seen in Figure 4.5, which shows the mean Ψ for each of the σ^2_{CRH}-based terciles (Figure 4.11 shows Ψ for each individual run). Nearly all of the simulations produce a trimodal circulation, and the relative strength of the three modes clearly changes with aggregation. As in the RCEMIP ensemble, the congestus cell strengthens with aggregation and even dominates the deep circulation in the most aggregated runs. Congestus invigoration evidently comes at the expense of the shallow circulation, which is also apparent in the profiles of v at the 50th CRH percentile (Fig. 4.4g). In the unaggregated runs, there is strong shallow outflow (negative v) at $\sim$900 hPa and very weak congestus outflow. In the aggregated runs, the congestus outflow strengthens by a factor of $\sim$5 and the shallow outflow weakens. This trade-off is unexpected considering the previous finding that shallow circulations promote aggregation [*Bretherton et al.*, 2005; *Muller and Held*, 2012]. We suspect that the weakening of the shallow circulation is in part due to the formation of a strong inflow (positive v) layer above the boundary layer in the aggregated runs, which may interfere with the shallow convective outflow that would otherwise occur

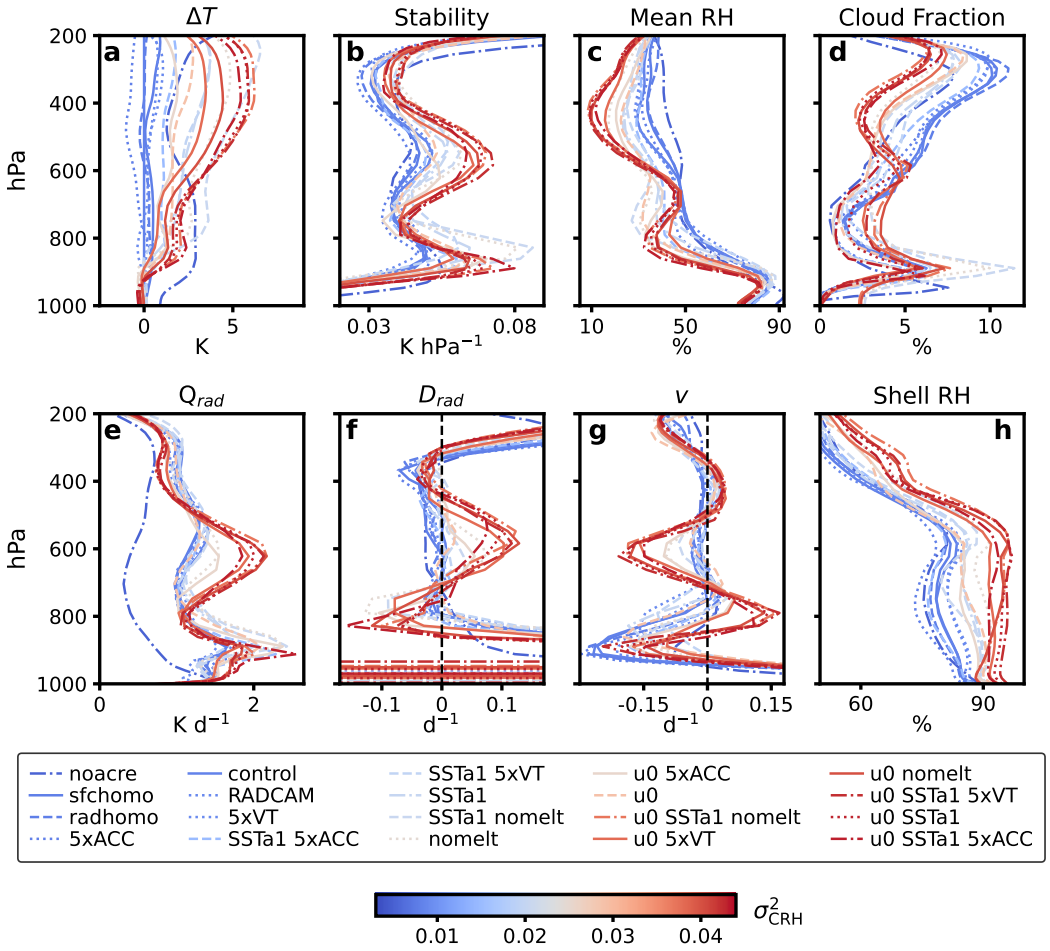

Figure 4.4: Selected profiles from the 2D SAM runs, with the color of each line corresponding to the degree of aggregation. (**a**) Temperature anomaly ΔT with respect to the control run, (**b**) static stability, (**c**) mean RH, (**d**) cloud fraction, (**e**) radiative cooling rate $Q_{\rm rad}$, (f) radiatively driven divergence $D_{\rm rad}$, (**g**) horizontal velocity v at the 50th CRH percentile, and (**h**) RH within 9 km of a convective updraft. With the exception of (**g**), all profiles are domain averages.

at a similar level. The inflow is seemingly forced by convergence of the radiatively driven subsidence (negative $D_{\rm rad}$) between 800-900 hPa at low CRH percentiles (Figs. 4.4f, 4.16). This convergence, which is weak or absent in the unaggregated runs, works against the radiatively driven divergence at the top of the boundary layer that normally draws outflow from the convecting regions. This competition between the shallow and congestus circulations

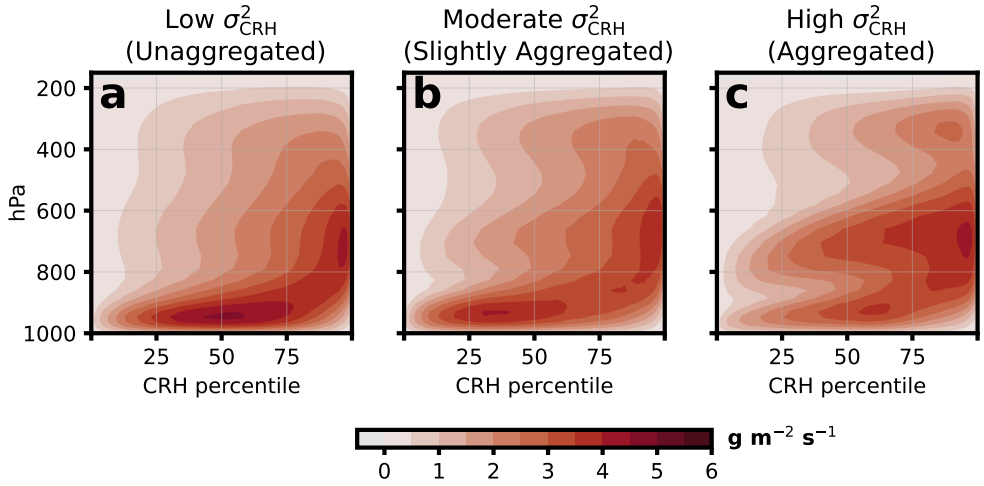

Figure 4.5: Streamfunctions for the 2D RCE ensemble, shown as the average of the streamfunctions from the 6-7 simulations falling within each σ^2_{CRH} tercile. **(a)** $\sigma^2_{\mathrm{CRH}} < 0.011$ **(b)** $0.011 < \sigma^2_{\mathrm{CRH}} < 0.028$ **(c)** $\sigma^2_{\mathrm{CRH}} > 0.028$

is worthy of closer study but is not our primary focus here.

The 2D ensemble exhibits the various components of the radiative-divergence feedback and allows us to assess why the feedback is amplified by aggregation. Fig. 4.4f shows that the aggregated runs have a peak in radiatively driven divergence at the congestus level, while the unaggregated runs are approximately nondivergent there. This difference arises from a change in the vertical structure of the radiative cooling rate Q_{rad} (Fig. 4.4e). In the unaggregated runs, Q_{rad} is relatively uniform above the boundary layer. As convection aggregates, Q_{rad} nearly doubles in the mid-troposphere and decreases slightly aloft, creating a sharp gradient between 400-600 hPa. The shift generally reflects changes in the nonconvective regions, which occupy a majority of the domain (Figs. 4.13, 4.16).

The changes in Q_{rad} and D_{rad} with aggregation are ultimately driven by changes in the distribution of moisture. Aggregation is associated with a reduction in RH throughout the free troposphere, but the 600-700 hPa layer is an important exception. At that level, the aggregated runs are moistened by congestus outflow and have a mean RH similar to the unaggregated runs (Fig. 4.4c). Despite similar RH there, the aggregated runs undergo much

stronger radiative cooling because aggregation reduces the emissivity of the upper troposphere. The reduction in emissivity results from upper tropospheric drying and reduced high cloud amount, which simultaneously allow the midlevel moist layer to cool more efficiently and inhibit cooling aloft, since there is less water vapor there to do the emission. The combination of stronger congestus-level cooling and weaker cooling aloft creates the large Q_{rad} gradient that ultimately generates midlevel divergence.

The important insight here is that changes in the distribution of moisture with aggregation allow the radiative-divergence feedback to flourish. The formation of a dry patch with aggregation is crucial because it fosters radiatively driven divergence at the congestus level. Without aggregation, the upper troposphere stays moist, congestus outflow plumes cannot cool as strongly, and there is little or no divergence.

4.3.3 Mechanisms of congestus invigoration

The radiative-divergence mechanism of congestus invigoration is distinct, but not mutually exclusive, from the stability mechanism. To understand the relative importance of the two, we conduct another 2D simulation in which we artificially inflate D_{rad} in the absence of aggregation and its associated increase in stability. To do so, the radiative cooling rate is prescribed as the mean Q_{rad} profile from one of the highly aggregated runs; here we use *u0 5xVT*, but the results are similar if another aggregated run is used. The prescribed radiative cooling is horizontally uniform, which prevents aggregation. The *u0* and *5xVT* adjustments are not actually applied, and everything else about the prescribed radiation (PR) run is identical to the control.

Results from the PR run are shown in Figure 4.6. The temperature profile in the PR run is free to vary but stays within 1 K of the control run profile up to 300 hPa. As a result, midlevel stability remains close to the control (Fig. 4.6a). On the other hand, the vertical structure of D_{rad} is more similar to the aggregated run, which is by design (Fig. 4.6c). So, the PR run captures the aggregation-related increase in meanD_{rad} without the increase in stability that would normally accompany it.

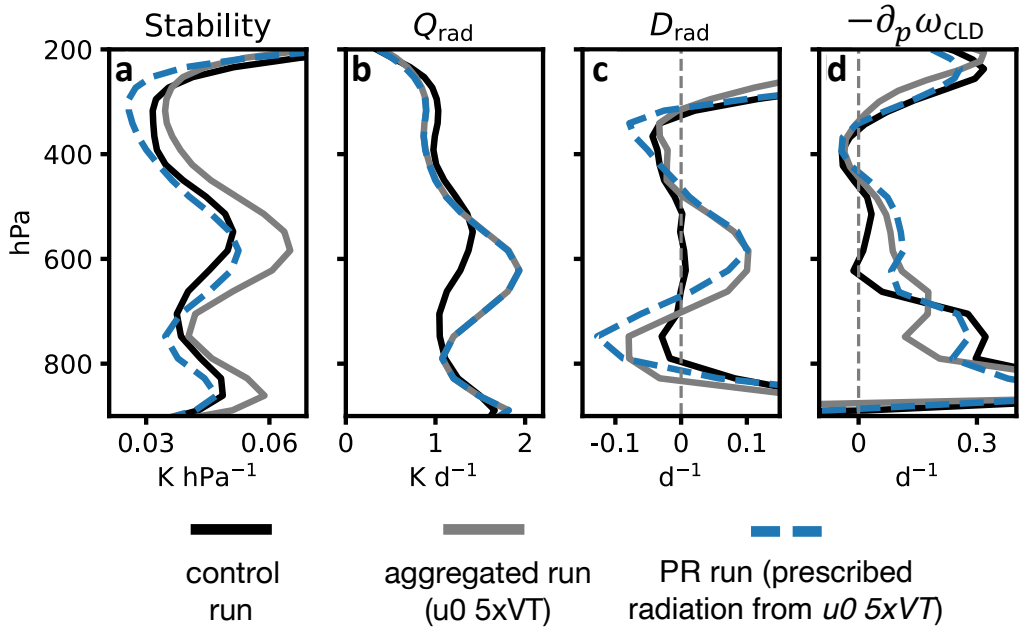

Figure 4.6: Results from the prescribed radiation (PR) run. (**a**) Static stability, (**b**) radiative cooling rate Q_{rad}, (**c**) radiatively driven divergence D_{rad}, and (**d**) convergence of the in-cloud mass flux $-\partial_p \omega_{\mathrm{CLD}}$. All profiles are domain averages. Clouds are defined as grid boxes with a cloud condensate mixing ratio exceeding 10^{-5} kg/kg.

How does this affect the congestus circulation? In the PR run, v_{cong} changes very little from its value in the control run, which seemingly suggests that the increase in D_{rad} alone does not invigorate the congestus circulation. However, it is important to remember that v_{cong} is simply a measure of the strength of the horizontal flow from high to low CRH. This is different than the amount of congestus-level detrainment from convection, which we quantify as the convergence of the in-cloud mass flux, $-\partial_p \omega_{\mathrm{CLD}}$. In the rest of the 2D ensemble, v_{cong} and $-\partial_p \omega_{\mathrm{CLD}}$ are tightly coupled (Figure 4.17) because strong radiatively driven divergence occurs in low-CRH regions while convection occurs in high-CRH regions; as a result, nearly all of the mass detrained from convection flows toward lower CRH to satisfy mass continuity there. This is not the case in the PR run, in which the prescribed cooling is horizontally uniform and D_{rad} is decoupled from CRH. While some of the mass detrained from convection must still flow towards low CRH to satisfy continuity there, some of it must also remain at

high CRH to satisfy the local divergence that we have imposed, resulting in a decrease in the magnitude of v_{cong} relative to $-\partial_p \omega_{\text{CLD}}$. Thus, for equal domain-averaged D_{rad}, the PR run will have similar $-\partial_p \omega_{\text{CLD}}$ but smaller v_{cong} than a run with interactive radiation. Fig. 4.6d shows that congestus-level $-\partial_p \omega_{\text{CLD}}$ in the PR run is similar to the aggregated run, which confirms that congestus-level detrainment scales with the mean D_{rad}. This result is to be expected for an atmosphere in RCE; since convective heating must exactly balance radiative cooling, the prescribed decrease in Q_{rad} with height between 600 and 400 hPa requires the convective heating rate to also decrease with height. This manifests as convective mass flux convergence (i.e., detrainment) at the same level.

The PR run shows that the increase in congestus-level *detrainment* with aggregation can be attributed to the concurrent increase in domain-averagedD_{rad}; the increase in midlevel stability is not necessary. However, invigoration of the congestus *circulation* in moisture space requires horizontal gradients in D_{rad} and does not occur when radiative cooling is horizontally uniform. When radiation is interactive, the formation of a dry patch with aggregation allows for both an increase in domain-averaged D_{rad} and the development of strong D_{rad} gradients. The takeaway here is that the radiative-divergence feedback, rather than the increase in midlevel stability, is responsible for congestus invigoration. This leads us to our final question: what is the nature of the stability response to aggregation? Does it have anything to do with congestus invigoration?

4.3.4 Summary

- In the 2D RCE ensemble, aggregation invigorates congestus overturning at the expense of the shallow circulation.

- Aggregation creates a favorable environment for the radiative-divergence feedback by reducing the emissivity of the upper troposphere.

- A simulation with prescribed radiation shows that greater radiatively driven divergence

leads to more congestus detrainment even when there is no increase in static stability.

4.4 Why does static stability increase with aggregation?

We focus now on the increase in tropospheric static stability that accompanies aggregation and congestus invigoration (Fig. 4.4b). While we have established that the stability increase is not critical for congestus invigoration in the 2D RCE runs, we remain interested in its causes and its relationship to the congestus mode.

To simplify our discussion, we compare the mean stability profiles for the most and least aggregated terciles of the 2D ensemble runs. The yellow line in Fig. 4.7b shows the change in domain-averaged stability between the unaggregated and aggregated terciles. Stability increases everywhere between 250-950 hPa, with the largest increases at the congestus level and the top of the boundary layer. Our goal here is to determine the causes of the stability increase and to explain its vertical structure.

Previous work has typically attributed the stability increase to changes in convective processes (we will discuss the exact mechanisms shortly). The red line in Fig. 4.7b shows the change in stability within portions of the model domain that are actively convecting, which we define as those with a 400-600-hPa mean ω less than -5 Pa s^{-1} and total condensate mixing ratio greater than 10^{-5} kg kg^{-1}. Within active convection, stability increases with aggregation at all tropospheric levels. But the vertical structure of the stability change looks nothing like that of the change in domain-averaged stability. At the congestus level and at the top of the boundary layer, the increase in domain-averaged stability is much greater than one would expect from the changes within active convection, while the opposite is true other levels. This tells us that the mean RCE temperature profile is not simply "set" by deep convection. While changes in convective processes provide a baseline increase in stability throughout the troposphere, radiative processes are also important, and the effect of these processes on the mean temperature profile evidently changes with aggregation. In the remainder of this section, we discuss and evaluate the convective and radiative sources of enhanced stability.

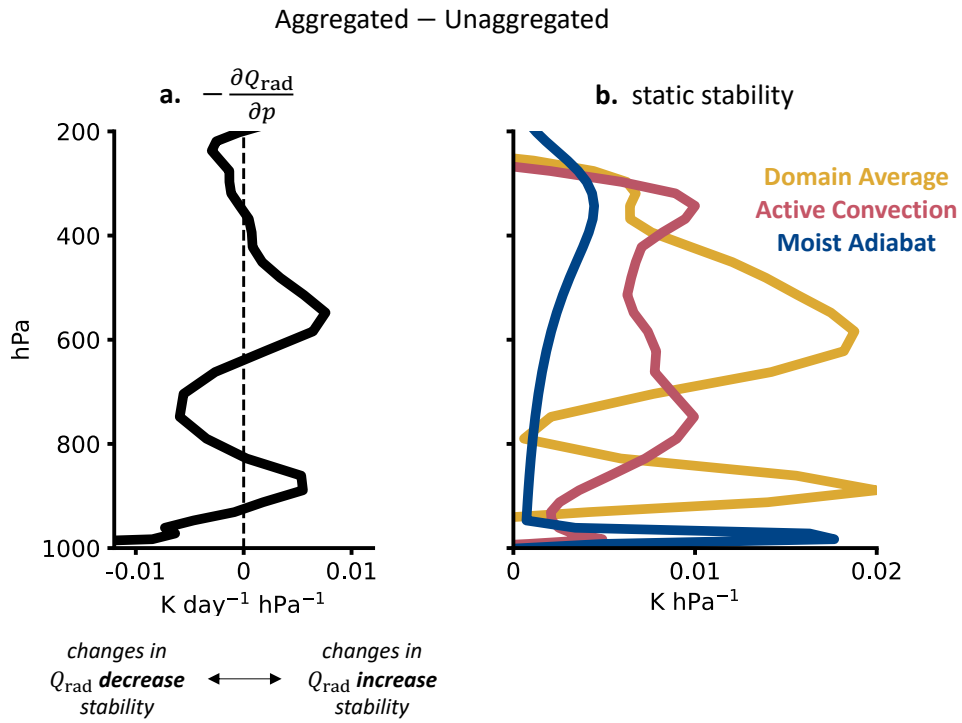

Figure 4.7: Difference between aggregated and unaggregated 2D runs in (**a**) differential radiative cooling and (**b**) three different static stability profiles. Yellow: domain-averaged stability; red: stability in grid boxes containing active convection; blue: stability of a undiluted moist adiabat computed as described in the text.

4.4.1 Convective Sources

Why does the static stability within active convection increase with aggregation? Here, we discuss two explanations from the literature and evaluate their importance in the 2D ensemble.

The first explanation is that aggregation increases the initial moisture content of convective updrafts, which causes convection to follow a warmer, more stable moist adiabat. *Held et al.* [1993] suggested that the increase in initial moisture content occurs because convection begins closer to the surface, where it more humid. But in the 2D ensemble, aggregation is associated with a *decrease* in the fraction of actively convecting columns that have upward motion throughout the boundary layer, so this mechanism does not explain the present

results. Alternatively, *Bretherton et al.* [2005] found that the near-surface RH in convective regions increases with aggregation, which would boost the initial moisture content of updrafts without any change in their initiation height. In the 2D ensemble, aggregation is indeed associated with an increase in boundary layer RH in convective regions. We assess the impact of this increase on stability by computing moist adiabatic temperature profiles (and associated stability profiles) for each run, using as the starting point the 1000-hPa temperature and RH in the top CRH percentile, where most of the upward convective mass flux occurs. The moist adiabats are computed using the MetPy Python package, which computes saturated pseudoadiabats neglecting the difference in saturation vapor pressure over liquid and ice [*May et al.*, 2008]. The blue line in Figure 4.7b shows the change in moist adiabatic stability between the aggregated and unaggregated terciles. The magnitude of the increase is far too small to account for the increase in stability within active convection, so we can conclude that changes in surface RH play only a minor role in the stability response to aggregation. This result is not sensitive to the exact level at which the moist adiabats are initialized.

The second explanation deals not with the initial moisture content of convection but with the impact of entrainment mixing once convection has begun. The tropical temperature profile deviates from a perfect moist adiabat due to the entrainment of unsaturated air into convective updrafts, which leads to evaporation and causes the lapse rate to exceed that of an undiluted plume [*Singh and O'Gorman*, 2013]. It has been hypothesized that aggregation mitigates this entrainment cooling [*Mapes and Neale*, 2011; *Feng et al.*, 2015], leading to an increase in stability. Large-eddy and convection-permitting simulations support this prediction, but with an important caveat: the reduction in entrainment cooling does not occur because entrainment itself is reduced (in fact, the opposite occurs) but rather because the entrained environmental air is more humid and thus cannot cause as much evaporative cooling [*Becker et al.*, 2018; *Becker and Hohenegger*, 2021]. In essence, aggregation creates a "moist shell" that protects convective plumes from entrainment cooling [*Becker et al.*, 2018]. This is physically intuitive, considering that what it means to be aggregated in the first place

is that convection occurs in the vicinity of other convection, where it is already likely to be moist. But aggregation as indicated by large σ^2_{CRH} by no means guarantees the presence of a moist shell. First of all, CRH is skewed towards the RH of the warm lower troposphere and therefore provides limited information about RH at higher levels. Furthermore, as shown by Figs. 4.1 and 4.9, variability in σ^2_{CRH} is driven mostly by how dry the dry regions are, which tells us nothing about the RH distribution in moist regions.

Is a moist shell detectable in our 2D simulations? We define the convective shell as the portion of the model domain that is within three grid boxes (9 km) of active convection but is not actively convecting itself. Fig. 4.4h shows that the mean shell RH increases with aggregation throughout the entire troposphere. It is not surprising to see this result at the level of congestus detrainment, since congestus invigoration itself moistens the convective shell there. But the greatest difference in shell RH (10-15%) is found below this level, between 700-900 hPa. Relative to a unaggregated shell RH of 80%, a 10-15% increase constitutes a 50-75% reduction in saturation deficit, suggesting that the moist shell effect has a substantial impact on the efficiency of entrainment cooling. Within the 700-900 hPa layer, the within-convection stability becomes increasingly sensitive to aggregation with height (Fig. 4.7b), which is consistent with the accumulating impact of the moist shell on a rising parcel. Of course, some of the impact may be offset if the entrainment rate increases with aggregation, as was found by *Becker et al.* [2018]. While an in-depth study of entrainment rates is beyond our scope here, the development of a moist shell with aggregation and the insufficiency of the alternative explanations both suggest that the moist shell plays an important role in stability enhancement. These results are not sensitive to the threshold used to define the convective shell.

4.4.2 Radiative Sources

We have now shown that decreases in entrainment cooling are likely more important than increases in surface RH when it comes to the increase in stability within active convection. We now turn to radiative sources of increased stability.

Posselt et al. [2008] suggested that differential radiative cooling at the top of congestus outflow layers could lead to enhanced stability, as the moist outflow layer cools more rapidly than the dry air immediately above. As we have already shown, the vertical gradient of Q_{rad} in the mid-troposphere is stronger when convection is aggregated. This is illustrated again in Fig. 4.7a, which shows the difference in $-\partial_p Q_{\mathrm{rad}}$ (where $\partial_p = \partial/\partial p$) between the aggregated and unaggregated terciles. At levels where $-\partial_p Q_{\mathrm{rad}}$ increases with aggregation (350-650, 825-900 hPa), changes in the Q_{rad} profile are acting to increase stability. Comparison of Figs. 4.7a and 4.7b shows that this occurs where the increase in domain-averaged stability exceeds that within active convection. The opposite is true where changes in $-\partial_p Q_{\mathrm{rad}}$ act to decrease stability. The structural similarity between the changes in differential radiative cooling and the changes in domain-averaged stability suggests that the former plays an important role in shaping the latter.

How can we be sure that the link between differential radiative cooling and enhanced mean stability is causal? Examining their association over space and time provides compelling evidence. Fig 4.8a shows an instantaneous snapshot of stability and Q_{rad} in one of the highly aggregated runs (*u0 SSTa1 5xVT*). The convective region is in the center of the domain, where the SST is slightly elevated. The sloping bands of strong radiative cooling mark the top of the congestus outflow layer. Stable layers, enclosed by the black contours, are found at the top of the outflow layer and remain linked to it as it subsides. In the driest regions (both ends of the periodic domain), the stable layer has detached from the outflow layer and is located just above it. We speculate that this has to do with the horizontal spreading of stability anomalies by gravity waves emanating out from convection. After detrainment, stability anomalies grow via differential cooling at the top of the outflow layer as it subsides. Eventually, the stability anomalies are "ripped off" of the outflow layer by gravity waves, which work to erase the horizontal temperature gradients that develop from the vertical displacement of the stability anomaly.

The link between stability and differential radiative cooling can also be seen over time. Fig. 4.8b shows the domain-averaged stability and Q_{rad} over a 10-day period in the same

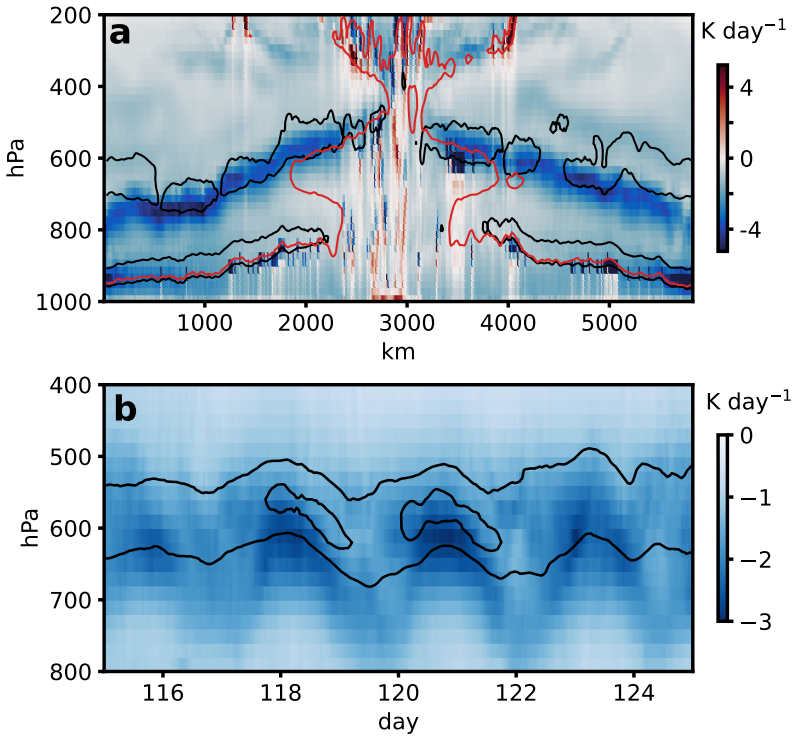

Figure 4.8: Stability and radiative cooling in a highly aggregated run (*u0 SSTa1 5xVT*). (**a**) Colored shading shows the instantaneous radiative heating rate. The black contour indicates static stability in excess of 0.075 K hPa^{-1} and the red contour relative humidity above 60%. (**b**) Blue shading shows the domain-averaged radiative heating rate over a ten-day period. Black contours indicate domain-averaged stability of 0.065 and 0.073 K/day.

aggregated run. Bands of strong radiative cooling originate at the congestus outflow level approximately every 2.5 days. These oscillations have been noted in previous work and have a period that depends on the size of the model domain [*Grabowski et al.*, 2000]. Stability anomalies can be seen growing at the top of the outflow plumes and subsiding with them. At a fixed pressure level, stability is greatest when there is strong differential radiative cooling.

4.4.3 Summary

- The static stability response to aggregation in the 2D ensemble is shaped by both convective and radiative processes; both are of similar importance.

- In convective regions, a reduction in entrainment cooling with aggregation is a more plausible driver of increased stability than changes in surface RH. These changes are not directly related to congestus invigoration.

- In nonconvective regions, strong differential Q_{rad} at the top of congestus outflow plumes act to increase midlevel stability. This change is directly tied to congestus invigoration.

4.5 Discussion

This chapter began with a discussion of the third mode of tropical convection: the congestus mode. We examined congestus representation and variability in the RCEMIP CRM ensemble and in a new ensemble of 2D RCE simulations conducted with SAM, a widely used cloud-resolving model. A wide variety of congestus representations were found in both ensembles, underscoring the need to better understand the nature of the congestus mode in cloud-resolving RCE.

The most significant finding of this work is that the congestus mode is invigorated by large-scale convective aggregation. The invigoration mechanism is, at its core, very similar to that which is thought to drive shallow circulations at the top of the boundary layer. Both rely on the presence of sharp vertical gradients in the longwave cooling rate, which are ultimately caused by sharp gradients in moisture. In the shallow circulation case, these gradients are found at the top of the moist boundary layer, whereas in the congestus case they are found at the top of congestus outflow plumes. Aggregation is an important part of this process because it dries out the upper troposphere in nonconvecting regions, which allows for stronger cooling at the top of the moist layer. This invigoration mechanism relies on basic principles of radiative transfer and mass conservation, and its components are present in both the RCEMIP and 2D RCE ensembles. While the impact of aggregation on congestus overturning is clear, whether or not the congestus mode affects initiation and development of aggregation remains uncertain.

Notably, congestus invigoration in the 2D ensemble is accompanied by a slowdown of the

shallow circulation. This may be explained by radiatively driven convergence just above the dry-region boundary layer, which drives dry-to-moist convective inflow at the level where shallow convective outflow would otherwise be found. Further study of this apparent competition between the shallow and congestus modes would be worthwhile and would improve our understanding of convective dynamics.

This work also examined how static stability affects and is affected by congestus invigoration. Previous work has largely assumed that mid-tropospheric stable layers are the cause of congestus-level detrainment. With this logic, congestus invigoration might be attributed to an increase in midlevel stability. But the results presented in sections 4.3.3 and 4.4 suggest that enhanced stability is largely the result, rather than the cause, of congestus invigoration. The crux of this finding was a model experiment showing that congestus-level detrainment increases without any change in stability in response to a prescribed increase in the mean radiatively driven divergence. It is important to reiterate that this result may be inevitable in simple RCE simulations such as these, in which any imposed gradient in radiative cooling must be matched by a gradient in convective heating. For this reason, we caution that this specific result may be limited in scope, and it is unclear to what extent it applies to the real tropics, where approximate RCE is realized only on large spatial and time scales [*Jakob et al.*, 2019].

In section 4.4, we asked why the mean static stability increases as convection aggregates. Much of this stability enhancement can be attributed to congestus invigoration: stability anomalies grow by differential radiative cooling atop congestus outflow plumes before being smoothed out by gravity waves. The stability increase is likely supported by a moistened convective shell, which reduces the efficiency of entrainment cooling and allows convecting parcels to adhere more closely to a moist adiabatic temperature profile. Aggregation also increases the surface RH in convecting regions, but this has a relatively small impact on stability compared to the other factors. These results are helpful for understanding the sensitivity of mean climate to aggregation, and they illustrate how the response to aggregation can be significantly affected by congestus dynamics. Our understanding of the stability re-

sponse to aggregation would benefit from simulations with finer horizontal resolution, which would provide a more complete picture of entrainment processes.

This work leaves us with many questions worthy of further study. How is congestus overturning affected by climate warming? The answer to this question will almost certainly depend on how warming affects the degree of convective aggregation, which remains very uncertain. And how may the congestus circulation itself affect the climate sensitivity of the RCE state? Given its impacts on moisture and radiative transfer, we suspect that congestus strength has a direct bearing on the surface and top-of-atmosphere energy budgets. Perhaps most importantly, how realistic are model representations of the congestus mode? Without a doubt, the findings reported here are helpful for understanding RCE simulated by cloud-resolving models. Their applicability to the real world remains an open question.

Deepening our knowledge of how clouds, convection, and circulation interact is a pressing priority within climate science and is critical to the advancement of the field [*Bony et al.*, 2016]. Cloud-resolving RCE simulations, such as those discussed here, have proven to be a valuable research tool in this endeavor. As we have shown, RCE climates can be greatly affected by the congestus mode. Careful interpretation of cloud-resolving RCE therefore requires continued study of the "forgotten mode" of tropical convection.

4.6 Supplementary Figures

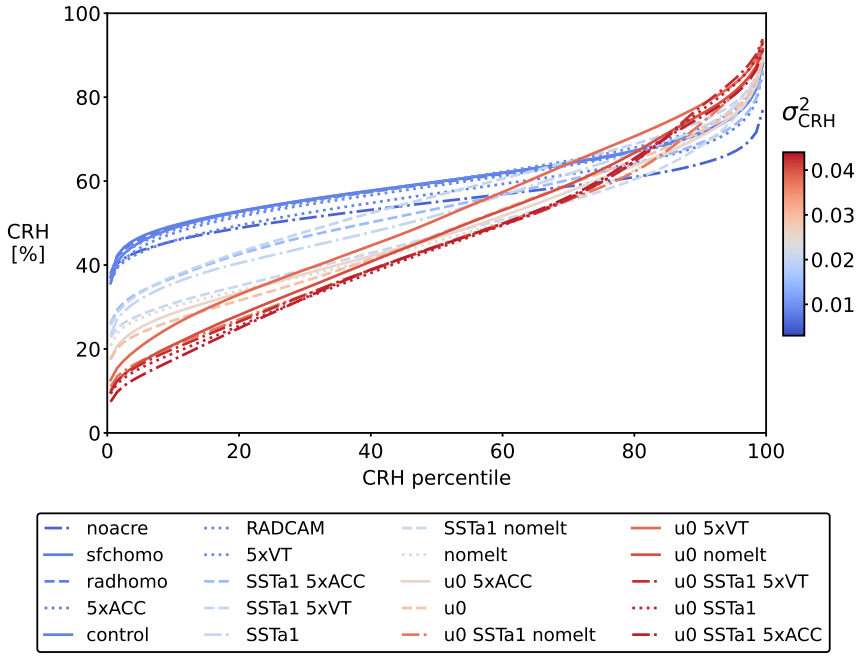

Figure 4.9: Column relative humidity (CRH) distributions for each run in the 2D RCE ensemble. The color of each line corresponds to the degree of aggregation (red is high σ^2_{CRH}).

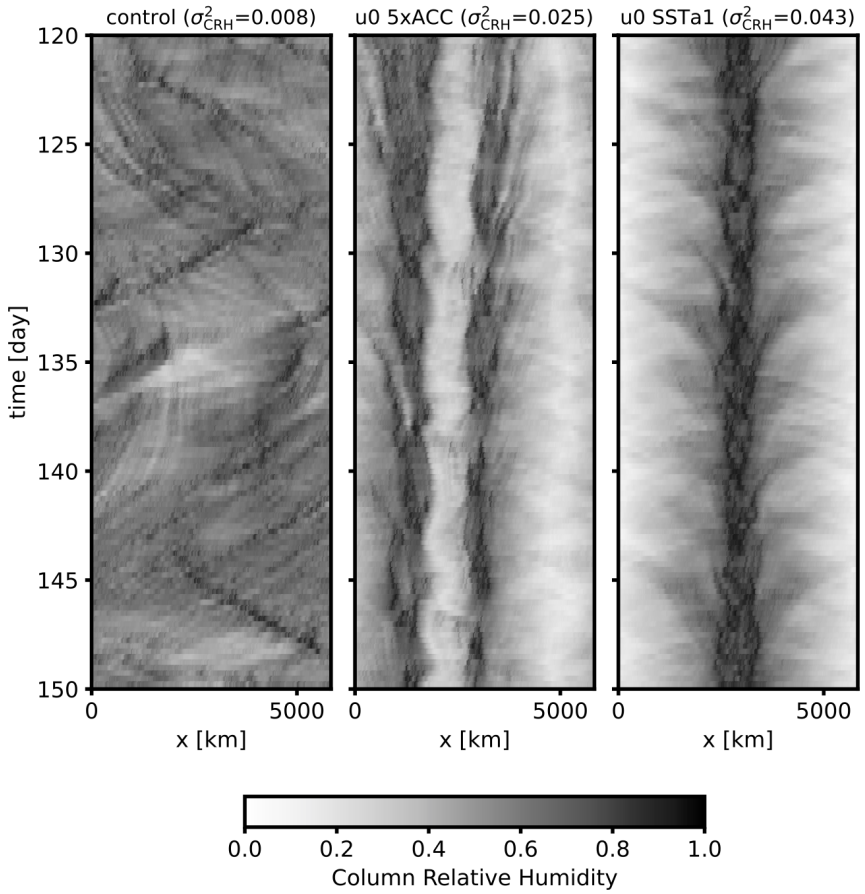

Figure 4.10: Hovmöller diagrams of column relative humidity for three of the simulations in the 2D ensemble. The three runs were chosen because they illustrate low, moderate, and high degrees of aggregation. Data are coarsened to 12-km horizontal and 6-hour time resolution before plotting.

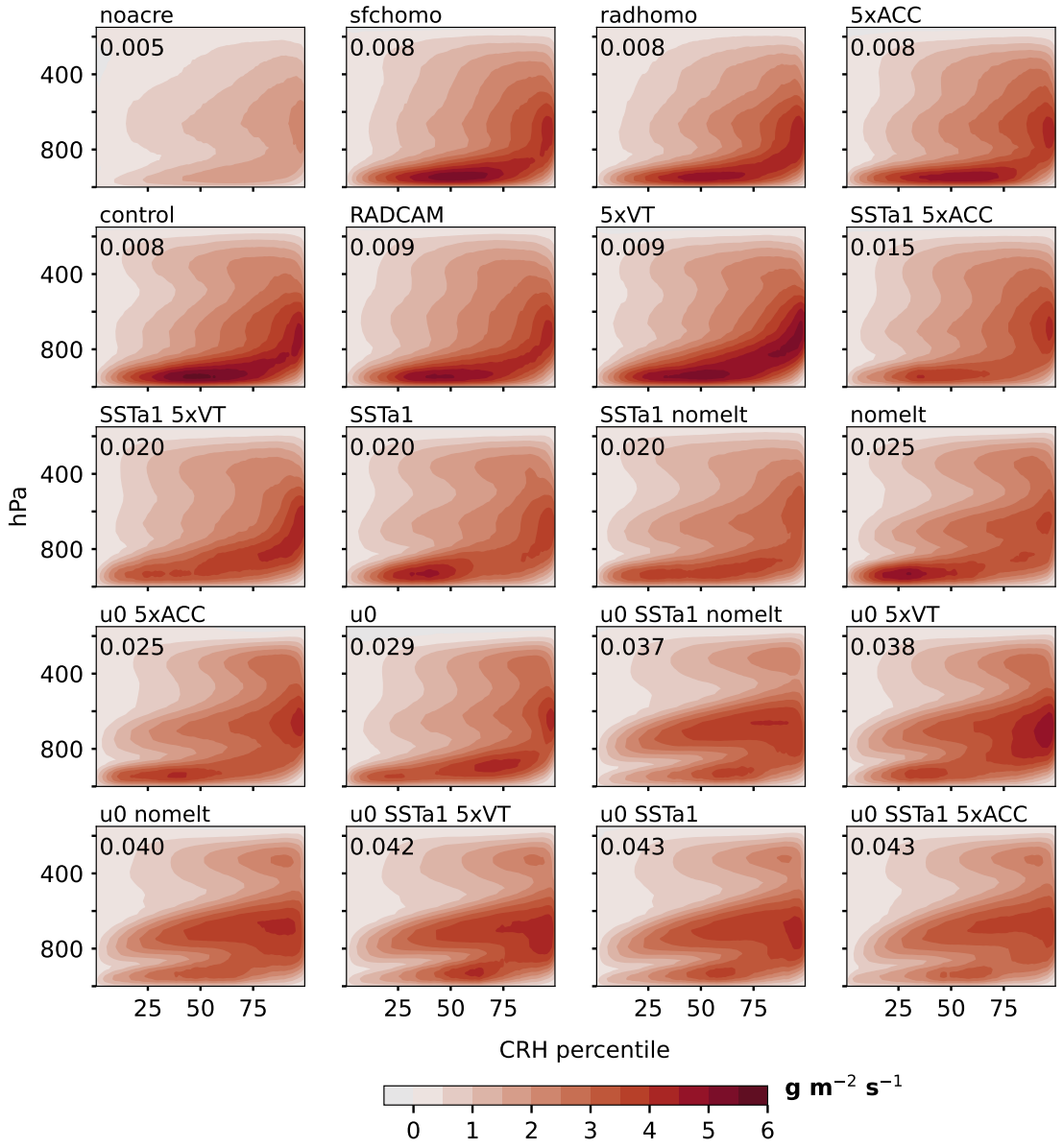

Figure 4.11: Streamfunctions for each simulation the 2D RCE ensemble. The simulations are ordered by increasing σ^2_{CRH}, which is given in the top left corner of each plot.

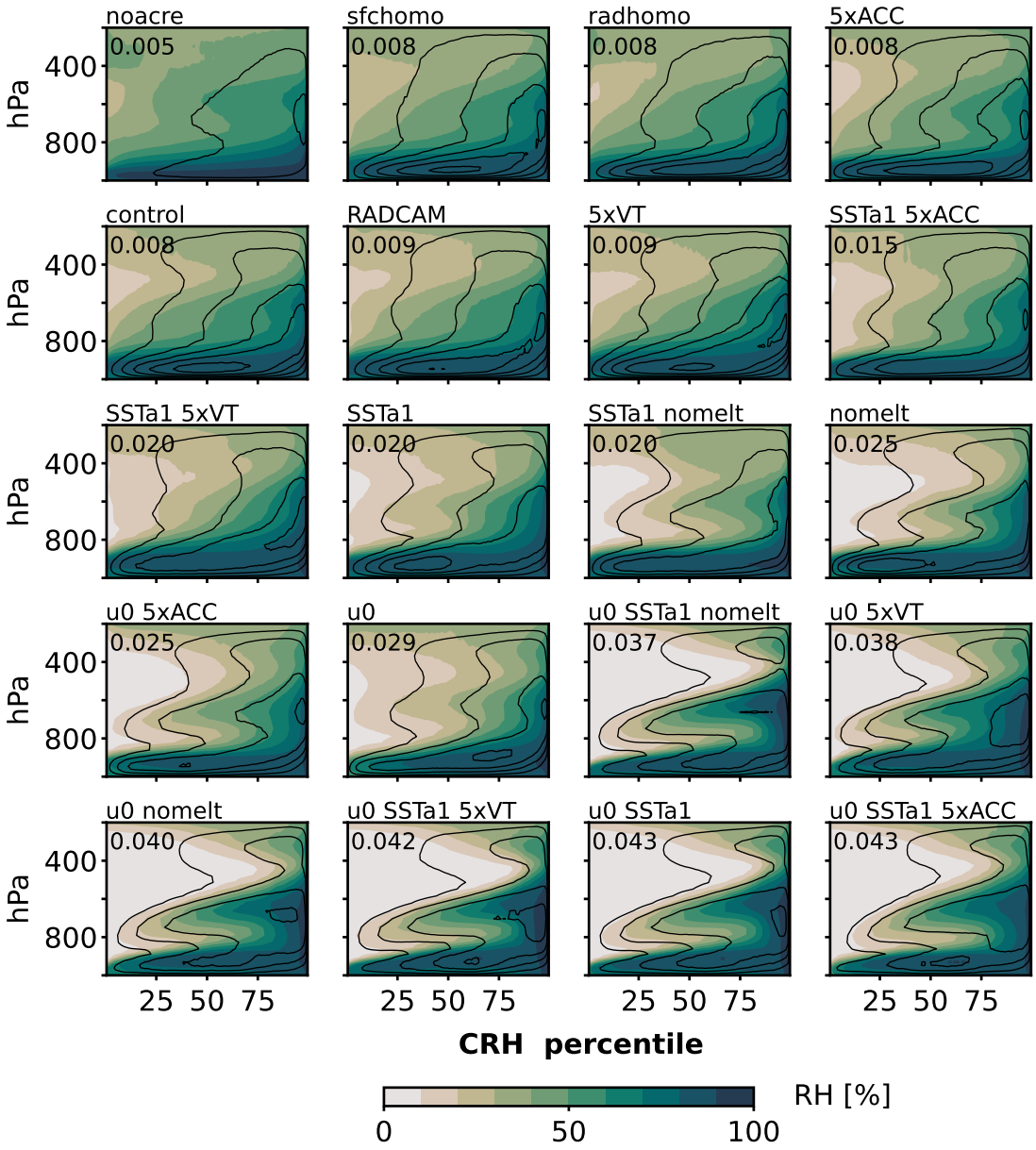

Figure 4.12: Relative humidity as function of pressure and CRH percentile for each simulation in the 2D RCE ensemble. Black contours show the streamfunction Ψ reproduced from Fig. 4.11 and have a spacing of 1 g m^{-2} s^{-1} (the outermost contour is 1 g m^{-2} s^{-1}).

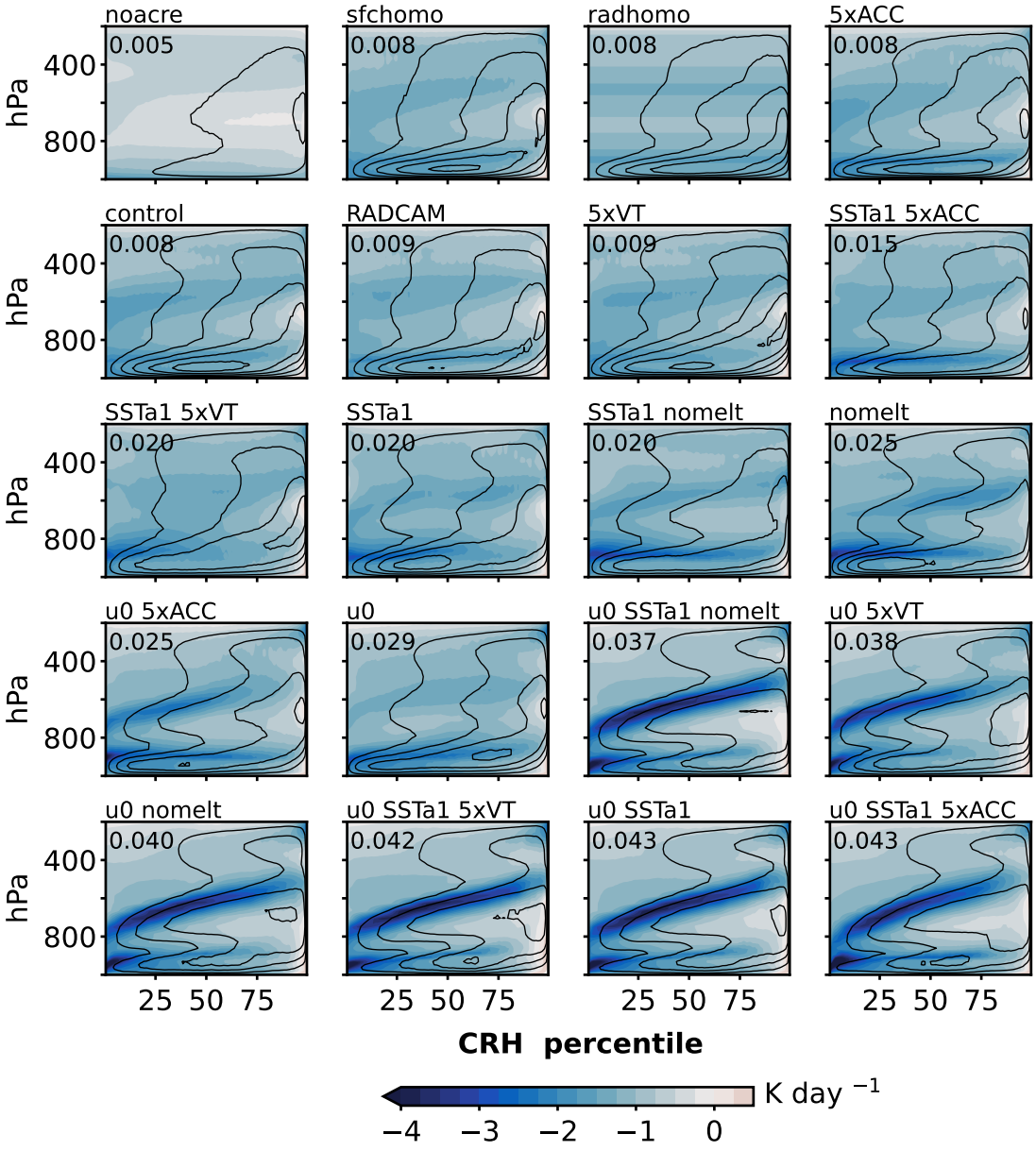

Figure 4.13: As in Fig. 4.12 but for the radiative heating rate.

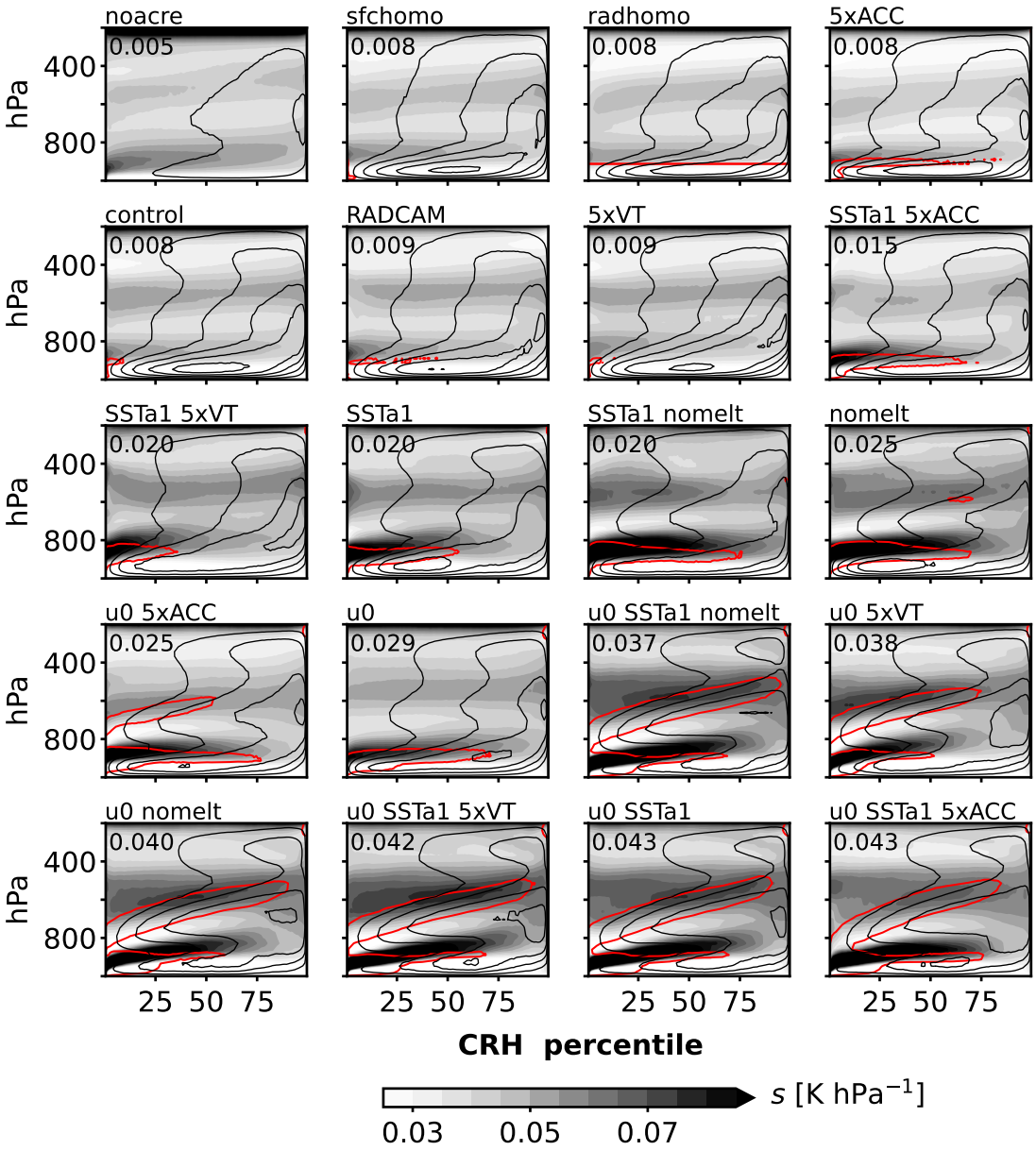

Figure 4.14: As in Fig. 4.12 but for static stability. The color scale is intended to accentuate differences in stability in the mid-troposphere. The red contours enclose regions where the radiative cooling rate exceeds 2 K day^{-1}.

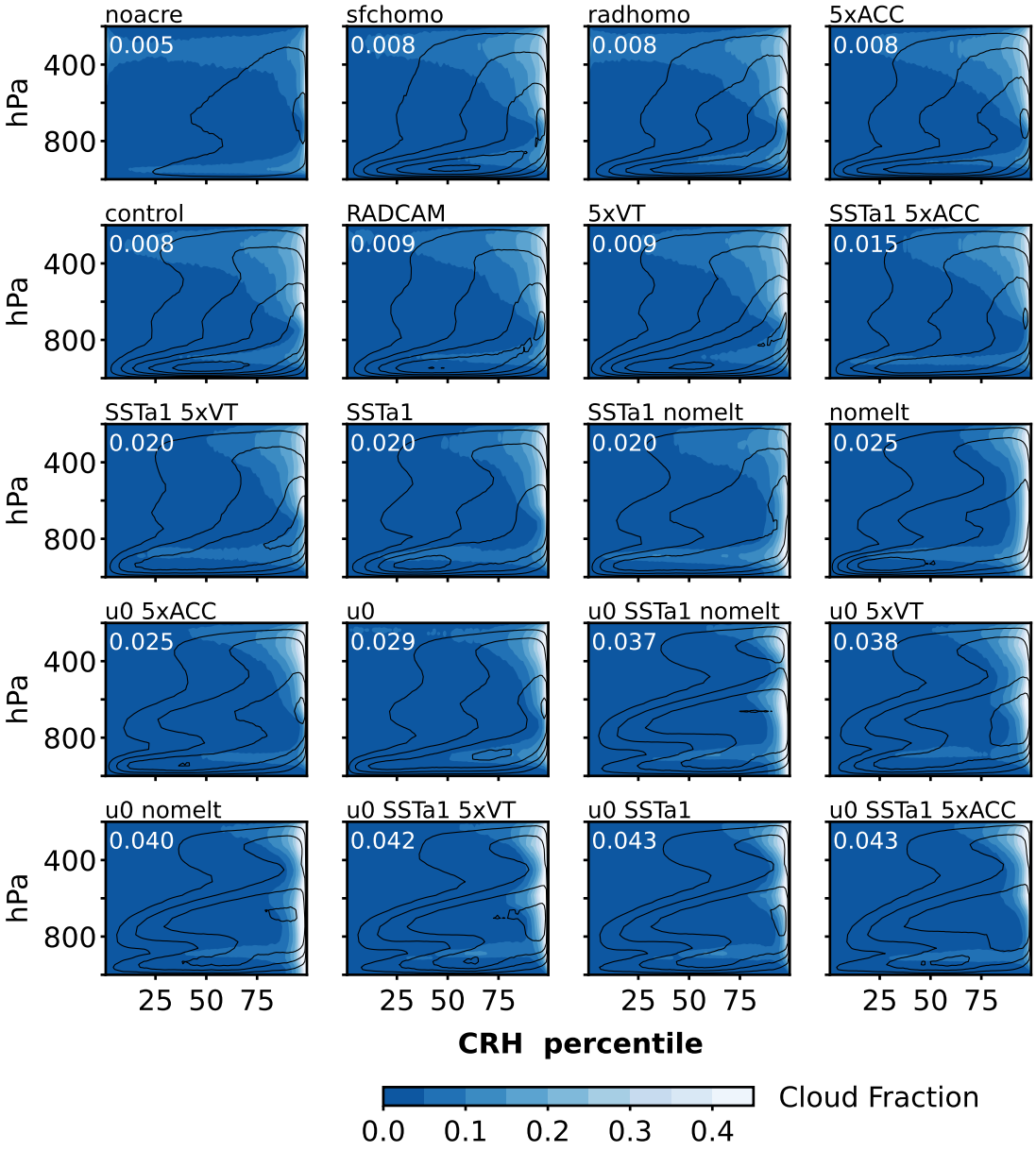

Figure 4.15: As in Fig. 4.12 but for cloud fraction.

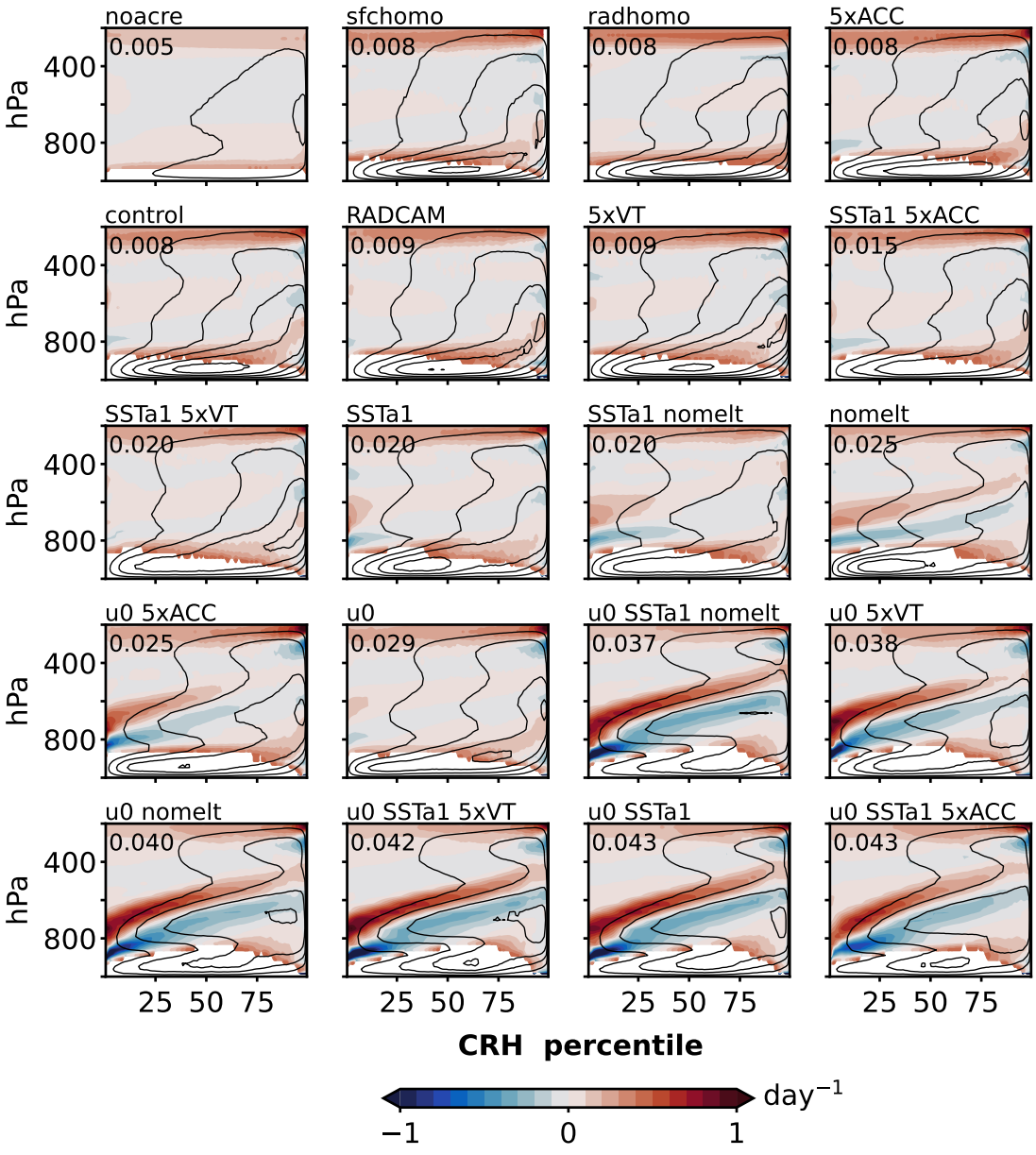

Figure 4.16: As in Fig. 4.12 but for the radiatively driven divergence D_{rad}. D_{rad} is not shown within the boundary layer, where it is undefined due to near-zero stability.

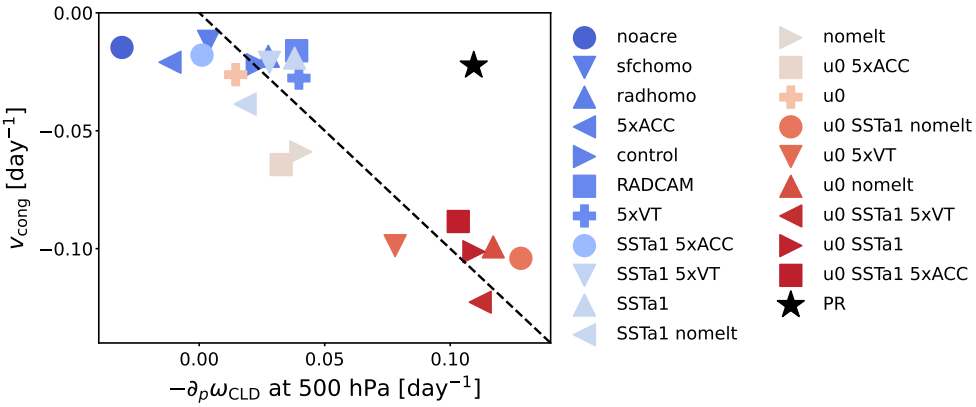

Figure 4.17: Relationship between two measures of congestus strength in the 2D ensemble. v_{cong} is defined in section 2.2 and $-\partial_p \omega_{\text{CLD}}$ is the convergence of the in-cloud mass flux. $r^2 = 0.81$ excluding the prescribed radiation (PR) run.

Chapter 5

INTERNAL VARIABILITY IN KILOMETER-SCALE SIMULATIONS OF COUPLED RADIATIVE-CONVECTIVE EQUILIBRIUM

I acknowledge the contributions of the following co-authors to the work in this chapter: Vlad Munteanu, Pedro Angulo-Umana, Peter N. Blossey, and Dennis L. Hartmann.

5.1 Introduction

The spatial distribution of sea surface temperature (SST) in the tropical Pacific plays a critical role in the internal variability of Earth's climate as well as its response to forcing [*Bjerknes*, 1969; *Andrews et al.*, 2018]. The tropical SST pattern is set not only by ocean dynamics, but also by interactions between tropical convection, clouds, and the large-scale atmospheric circulation [*Knutson and Manabe*, 1995; *Vecchi and Soden*, 2007; *Latif et al.*, 2023; *Ramanathan and Collins*, 1991; *Deser et al.*, 2010]. Understanding these interactions and their role in internal climate variability is critical for making sense of future climate projections [*Wills et al.*, 2022]. Our primary focus here is on the atmospheric component of that variability, which we explore using a model in which ocean dynamics are neglected but SST is responsive to atmospheric processes.

The upward transport of mass by tropical deep convection is an important factor in tropical variability. The strength and organization of convective mass flux affects large-scale overturning circulations such as the east-west Walker circulation in the equatorial Pacific. Walker circulation strength can, in turn, impact the spatial pattern of SST [*Vecchi and Soden*, 2007], which feeds back on the large-scale organization of convection. Even in the absence of SST feedbacks, convective organization may affect the climatological convective mass

flux and circulation via its impact on the structure of the tropical troposphere. Convective organization is known to affect the dry static stability of the troposphere [*Bony et al.*, 2016; *Becker et al.*, 2018], which in models has important implications for circulation strength [*Knutson and Manabe*, 1995; *Ma et al.*, 2012; *Sohn et al.*, 2016]. Organization also impacts the area covered by convectively generated anvil clouds, which themselves affect the large-scale circulation via cloud radiative heating [*Voigt et al.*, 2019]. In fully coupled general circulation models (GCMs) with parameterized convection and realistic geometry, it can be difficult to disentangle these intertwined pathways of SST-convection-circulation interactions. Idealized modeling paradigms, such as the radiative-convective equilibrium (RCE) approach taken here, are useful for understanding the fundamental processes at play.

Several previous studies have examined the mean state and internal variability of coupled RCE using GCMs with parameterized convection. These simulations have typically adopted some variation of a "Tropic World" protocol [*Hartmann and Dygert*, 2022], in which the Earth is a non-rotating, spherical aquaplanet with horizontally uniform insolation. In the first of such experiments, *Popke et al.* [2013] found that convection organized into features of various size and that the mixed-layer SST varied by 6-9 K across the globe, depending on the convection scheme. *Reed et al.* [2015] found that interactive SSTs were associated with a reduced degree of convective organization compared to fixed-SST runs, although there were clearly defined convective and subsiding regions in both configurations. In their simulations, the global mean SST was relatively steady after the initial equilibration period. In contrast, experiments by *Coppin and Bony* [2017] featured oscillations in global mean SST, SST contrast, convective aggregation, and low cloudiness with a timescale dependent on mixed-layer depth. Mean SST and convective organization were out-of-phase with one another, and periods of enhanced SST contrast were associated with global mean cooling. *Drotos et al.* [2020] performed experiments with varying CO_2 levels and found irregular oscillations in global mean SST of $\sim$8 K. The cycles were driven by variability in inversion strength at the top of the planetary boundary layer (PBL), which drove the rather abrupt formation and collapse of low stratiform cloud decks. Notably, this large-amplitude variability only occurred

for CO_2 concentrations of at least 8 times the preindustrial reference of 278 ppm. *Dygert and Hartmann* [2023] described a unique mode of variability in which the SST contrast varied substantially but the mean SST was relatively steady. In those cycles, SST contrast developed due to spatial contrasts in low cloud amount, surface evaporation, and free tropospheric moisture content and collapsed due to the transport of energy from warm to cool regions by the large-scale atmospheric circulation, among other factors.

In this work, we examine internal variability in coupled RCE simulations using a cloud-resolving model (CRM) that explicitly resolves convection. CRMs are widely used to investigate tropical cloud and convective processes but, in contrast to the GCM studies described above, are most often run for short integration times on limited-area, doubly periodic domains with fixed, uniform SSTs [e.g., *Wing et al.*, 2018]. Mixed-layer oceans have been used in a handful of experiments [*Hohenegger and Stevens*, 2016; *Chen and Wu*, 2019; *Shamekh et al.*, 2020; *Tompkins and Semie*, 2021], most of which investigated the impact of interactive SSTs on the initial onset of convective aggregation. Here, we focus on much longer timescales by integrating a coupled CRM for over 21 years on a domain that is as long as the equatorial Pacific basin. On these timescales, the coupled system develops an internal cycle in which SST (both its mean value and its spatial distribution), convective organization, and the atmospheric circulation vary coherently.

In the first part of this chapter, we describe the CRM simulation (section 5.2) and the cycles of coupled variability that it produces (section 5.3). In the second part, we leverage this variability and a simple entraining plume model to investigate the convectively driven overturning circulation (section 5.4) and the stratification of the tropical troposphere (section 5.5). Along the way, we use atmospheric and SST reanalyses to contextualize the simulation within the observed Tropics. Finally, we explore the sensitivity of the internal cycle to domain length (section 5.6) and mean climate (section 5.7). Section 5.8 offers a summary and conclusions.

5.2 Data and Methods

5.2.1 Model Simulations

We use the System for Atmospheric Modeling [*Khairoutdinov and Randall*, 2003, SAM;] with the P3 microphysics scheme [*Morrison and Milbrandt*, 2015]. The model domain is two-dimensional (x and z), has 3-km horizontal resolution, and has a length of 13,122 km—similar to the size the tropical Pacific basin. The variable-resolution vertical grid has 81 levels with a spacing of 80 m near the surface, 333 m throughout most of the troposphere, and ∼1 km near the model top at 29.4 km. The mean horizontal wind is nudged to zero on a one-day timescale to avoid oscillations in the mean wind that are known to develop in two-dimensional RCE [*Held et al.*, 1993].

The atmosphere is coupled to a 25-m mixed-layer ocean. At each model time step, the SST at each grid point evolves in response to local energy fluxes at the surface:

$$\rho_w C_w H \frac{d}{dt} SST(x,t) = SW(x,t) + LW(x,t) - LHF(x,t) - SHF(x,t) - Q \qquad (5.1)$$

Here, ρ_w and C_w are the density and specific heat capacity of water, and $H = 25$m is the ocean depth. SW and LW are the net downward shortwave and longwave fluxes at the surface, respectively. LHF and SHF are surface latent and sensible heat fluxes, respectively, and Q is the parameterized ocean heat export (i.e., the Q-flux), which is applied uniformly in space and time. The Q-flux is intended to mimic the export of heat from the Tropics to the midlatitudes, and it is necessary for achieving reasonable SSTs under realistic tropical insolation, which in these experiments follows a diurnal cycle with a mean of 413.8 W/m^2. The simulation described here uses $Q = 35$ W/m^{-2}.

To speed up the initial ocean adjustment process, we first integrated a run with $H = 10$ m for 100 days. This run was initialized with uniform SST. At day 100, we switch H to 25 m (without changing the spatial SST field) and began the main run examined in this chapter which was integrated for 7,900 days (more than 21 years). Unless stated otherwise, results

generally reflect the last 4,900 days of the simulation, over which the time-averaged SST is 301.2 K. Results requiring full, vertically resolved model output (x, z, and t) rely on the last 900 days, during which the full output was collected every six (day 7000-7500) or every two (day 7500-7900) hours.

5.2.2 Analysis tools and metrics

We use several metrics to quantify various aspects of the SST distribution throughout the simulation. We first define the domain-averaged SST as $\overline{SST}$. In conceptual models of the tropical atmosphere, the temperature of the free troposphere is tightly linked to the sub-cloud entropy in regions of active convection [*Emanuel et al.*, 1994], which itself depends on the underlying SST. We may therefore expect the thermodynamic variability of the free troposphere to be more directly tied to the SST in actively convecting regions than to $\overline{SST}$. For this reason, we define SST_c as the mean SST in the warmest 30% of the model domain, which we take to represent regions of active convection. The 30% threshold was selected based on the SST percentile-sorted precipitation rate and 500-hPa vertical velocity, shown in Fig. 5.1a. The warmest 30% of the domain accounts for 73% of the total precipitation and undergoes mean ascent at 500 hPa, compared to mean subsidence elsewhere. Indeed, Fig. 5.1b shows that SST_c is significantly more predictive of free tropospheric temperatures than $\overline{SST}$. We thus adopt SST_c in lieu of $\overline{SST}$ for certain parts of the subsequent analysis.

We quantify the degree of spatial SST contrast using the standard deviation of SST across the domain, which we denote as σ_{SST}. To understand variability in SST contrast, we compute the budget for the spatial variance of SST, σ^2_{SST}. Following [*Tompkins and Semie*, 2021] and [*Hartmann and Dygert*, 2022], the prognostic equation for σ^2_{SST} is

$$\frac{d}{dt}\sigma^2_{SST} = (\rho_w C_w H)^{-1}(\overline{SST'SW'} + \overline{SST'LW'} - \overline{SST'LHF'} - \overline{SST'SHF'}) \tag{5.2}$$

where bars denote the domain mean and primes the deviation from that mean. The terms on the rhs are computed from instantaneous 2D output collected every 2 hours.

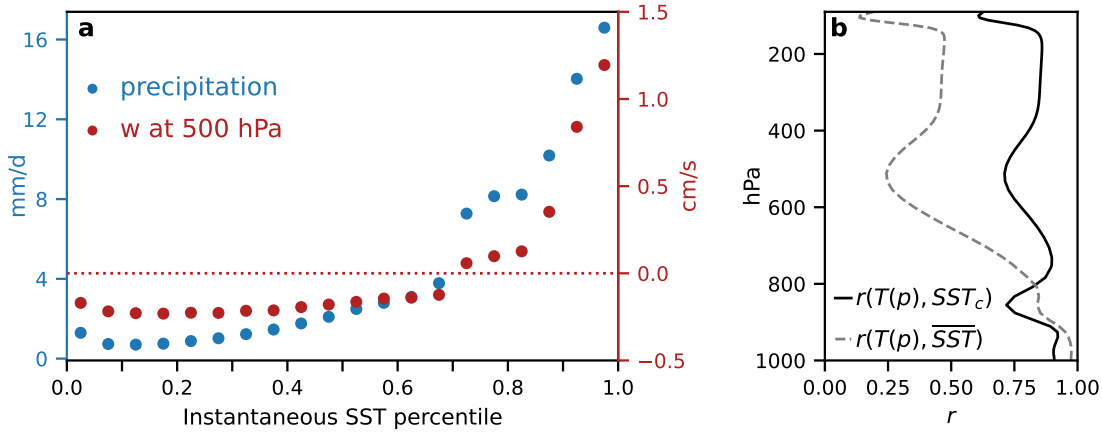

Figure 5.1: (a) Mean (blue) precipitation and (red) 500-hPa vertical velocity sorted by SST percentile. SST percentiles are computed for each day of the simulation such that 0 and 1 represents the coldest and warmest SSTs on any given day, regardless of the domain-averaged SST. Bin widths: 0.05. (b) Correlation coefficients between the daily mean temperature at each model level and (black) SST_c and (dashed grey) $\overline{SST}$.

5.2.3 Reanalysis

As a point of comparison throughout this chapter, we use the ERA5 reanalysis produced by the European Centre for Medium-Range Weather Forecasts [*Hersbach et al.*, 2020]. Monthly mean temperature and SST were retrieved at a horizontal resolution of 0.25°x0.25°. We use data from 1998-2013 and limit our analysis to the equatorial Pacific (15S-15N, 140E-258E). The study region was selected such that its zonal extent is approximately equal to the length of the model domain. The 1998-2013 mean SST for the region is 300.9 K, only 0.3 K cooler than the model simulation.

In section 5.5, we will investigate the relationship between static stability, surface temperature, and convective organization. For the reanalysis, we compute dry static stability from monthly mean temperature data. As for the model output, SST_c is computed as the mean SST in the warmest 30% of the study area and is intended to approximate the SST in convectively active regions.

We also compute two proxies for convective organization, the use of which is justified in

section 5.5:

1. σ^2_{CRH}: the spatial variance of column relative humidity (CRH) across the study region

2. σ_{SST}: the spatial standard deviation of SST across the study region

Monthly mean reanalysis is not well suited for the calculation of these two metrics, since forms of convective organization in the real Tropics, such as tropical waves, operate on faster timescales. To this end, we retrieve hourly temperature and specific humidity reanalyses, compute the two metrics for four times each day (0000, 0800, 1200, and 1600 UTC), and compute the monthly mean by averaging together all samples from each month. For σ^2_{CRH}, we compute the column-integrated water vapor (CWV) and the saturation column-integrated water vapor (CWV*) from the specific humidity and temperature data, respectively. CRH is then calculated as CWV/CWV* and the spatial variance of CRH across the study is taken.

5.3 Description of the cycle of internal variability

Figure 5.2 provides an overview of the cycle and time series of its important components. The cycle is defined by two phases, which are seen clearly in Fig. 5.2a: a cooling phase, in which σ_{SST} is high and $\overline{SST}$ steadily declines, and a warming phase, in which SSTs are relatively uniform and $\overline{SST}$ increases. In other words, uniform SSTs are associated with mean warming, while spatially varying SSTs are associated with mean cooling. σ_{SST} hovers around 0.28 and 1.2 K, respectively, during the warming and cooling phases of the cycle. The latter is similar to the typical standard deviation of SST across the equatorial Pacific study region (0.93 K). The boxcar-like variability of σ_{SST} (Fig. 5.2a) indicates that the transitions between the two phases are fast relative to the timescale of the full cycle. The period of the cycle, which we expect to be dependent on H [*Coppin and Bony*, 2017], is 680 days on average but ranges from 500 to 900 days. The warming and cooling phases are approximately equal in duration.

Over the 4,900-day simulation period used for results, there are seven full iterations of the cycle. Two iterations were completed prior to this period. During the results period, the

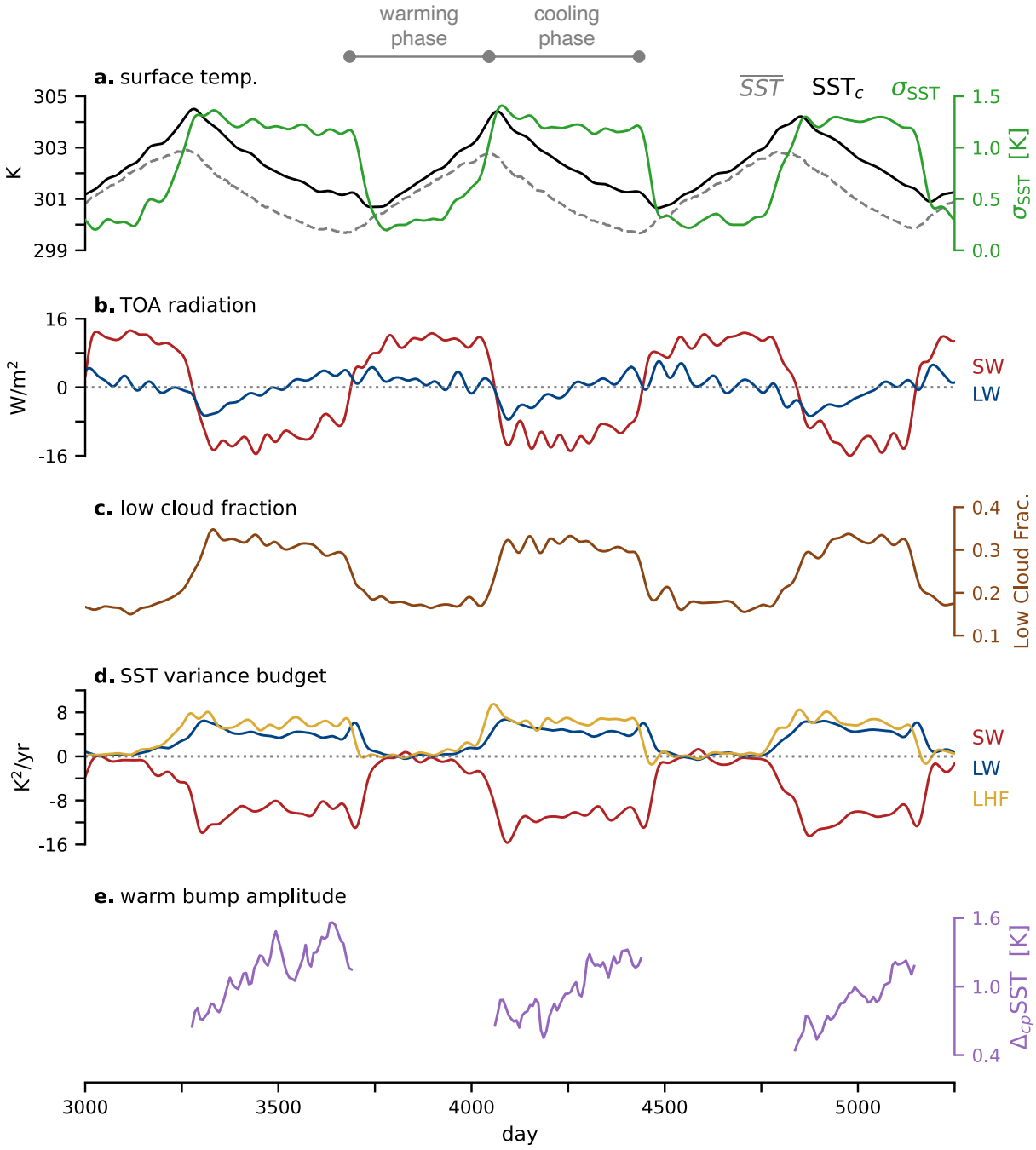

Figure 5.2: Time series of various quantities for a 2250-day period of the simulation. **(a)** various SST metrics; **(b)** net top-of-atmosphere downward radiation; **(c)** low cloud fraction; **(d)** the three leading terms of SST variance budget; **(e)** $\Delta_{cp}SST$, the metric developed in section 5.3.1 that quantifies the SST difference between the warmest and coldest parts of the cold, nonconvective region. For clarity, all time series except $\overline{SST}$ and $\Delta_{cp}SST$ are low-pass filtered using a 4th-order Butterworth filter with a 50-day cutoff.

typical amplitude of the $\overline{SST}$ cycle is 2.8 K (range: 2.0-3.6 K), greater than the 1.7 K range of monthly mean SSTs in the equatorial Pacific over the 16-year reanalysis period. Notably, the iteration immediately preceding the results period had an anomalously large amplitude of 4.6 K. The evolution of σ_{SST} was typical during this iteration, but the maximum value of $\overline{SST}$ achieved during this iteration was nearly 2 K higher than most subsequent iterations. This suggests that the transition from the warming to the cooling phase of the cycle does *not* occur at a fixed SST. Nevertheless, we exclude this period from our analysis due to its outsized influence on variability statistics.

The $\overline{SST}$ cycle is almost entirely driven by variability in absorbed shortwave (SW) radiation. Fig. 5.2b shows that, like σ_{SST}, top-of-atmosphere SW anomalies follow boxcar-like variability, with a difference of about 25-30 W/m^2 between the warming and cooling phases of the cycle. The dramatic shifts in SW reflectance are driven by changes in low cloud cover (Fig. 5.2c); during the cooling phase of the cycle, low cloud fraction is about a factor of two greater than during the warming phase. Compared to SW, variability in the top-of-atmosphere longwave (LW) flux is subtle ($\sim$10 W/m^2). LW anomalies are dominated by the Planck response to $\overline{SST}$ variability and, unlike SW, are not tightly coupled to σ_{SST}.

Throughout the cycle, spatial contrasts in SST are associated with similar contrasts in deep convective activity and precipitation (Figure 5.3). It is important to distinguish here between convective *aggregation*—which describes the tendency of convection to cluster into a well defined region(s) in numerical simulations [*Wing et al.*, 2017]—and convective *organization*, which refers to broader, non-specific ways in which convection clusters in space and time [*Pendergrass*, 2020]. Figure 5.3b shows that convection remains aggregated throughout the entire cycle, as there are always well defined regions of moisture and precipitation amidst a domain that is otherwise dry. The large-scale organization of convection, however, varies systematically throughout the cycle. During the high-σ_{SST} cooling phase, deep convection and heavy precipitation are confined to a single region over the warm pool. Regions of enhanced low cloudiness are found over the cooler SSTs on both side of the convective region. During the low-σ_{SST} warming phase, there are two convective regions and, as previously

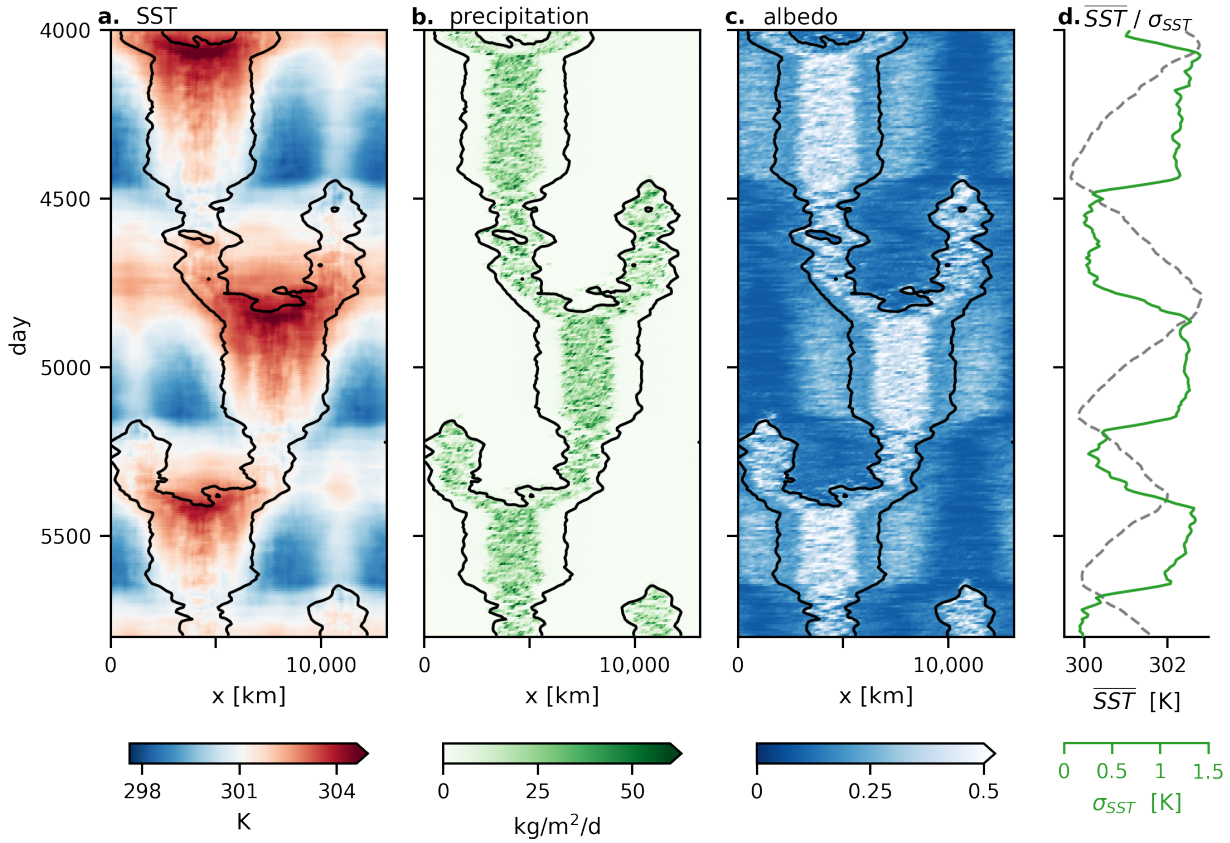

Figure 5.3: Hovmöller diagrams of weekly mean (a) SST, (b) precipitation, and (c) albedo for a 1800-day period of the simulation. Data are coarsened to a horizontal resolution of 81 km for plotting. The black contour indicates a column relative humidity of 0.6 and is intended to loosely enclose regions of active convection. (d) Time series of $\overline{SST}$ and σ_{SST} reproduced from Figure 5.2a.

mentioned, low clouds are less abundant. The relationship between σ_{SST} and the number of large-scale convective regions (one or two) is one-to-one throughout the cycle, which allows σ_{SST} to be used as a proxy for large-scale convective organization going forward.

The variability described so far is similar in some respects to previously described experiments and different in others. As in our simulation, GCM simulations of global, non-rotating RCE by *Drotos et al.* [2020] featured an irregular cycle of global mean SST driven by low cloud variability. A caveat is that this variability only occurred once the time-averaged SST

reached 305.8 K and was not present in simulations with a similar time-averaged SST to ours. Similarly, *Coppin and Bony* [2017] described a cycle in which enhanced SST contrast and convective organization was associated with global mean cooling, although it was not specified whether this cooling was primarily SW or LW driven. On the other hand, *Dygert and Hartmann* [2023] described cycles of SST contrast that did not involve significant variability of global mean SST. As in our simulation, greater SST contrast was associated with enhanced low cloudiness and more organized convection.

The remainder of this section examines the cooling and warming phases of the cycle in detail. The cooling phase is also referred to as the "high-contrast" or "high-σ_{SST}" phase, while the warming phase is also referred to as the "low-contrast" or "low-σ_{SST}" phase.

5.3.1 High-Contrast Cooling phase

The cooling phase of the cycle is broadly analogous to the equatorial Pacific during La Niña conditions, when the zonal SST gradient and Walker circulation are anomalously strong. The model domain features distinct warm and cold regions, with a difference of ∼3-3.5 K between the minimum and maximum SSTs (Fig. 5.4e). Deep convection, precipitation, and large-scale ascent are confined to a single region over the warmest SSTs, while cooler SSTs and large-scale subsidence occupy the rest of the domain (Fig. 5.4a,c,e).

The SST variance budget, given by Eq. 5.2 and shown in Fig. 5.2d, shows that spatial contrasts in SST are maintained by longwave and latent heat fluxes and damped by shortwave fluxes. In the warm region, longwave cooling of the surface is ineffective due to a stronger greenhouse effect there, and latent heat fluxes are weak due to high near-surface humidity and relatively weak surface winds (Fig. 5.4e). In the cold region, the surface cools more effectively by LW emission due to the dryness of the free troposphere above. In addition, strong surface winds and reduced near-surface humidity generate enhanced latent heat fluxes that cool the surface. Shortwave fluxes act to reduce σ_{SST} at all times, since deep convective clouds shade the warmest SSTs.

Within the cool, subsiding region of the domain, SST is far from uniform (Figs. 5.3a,

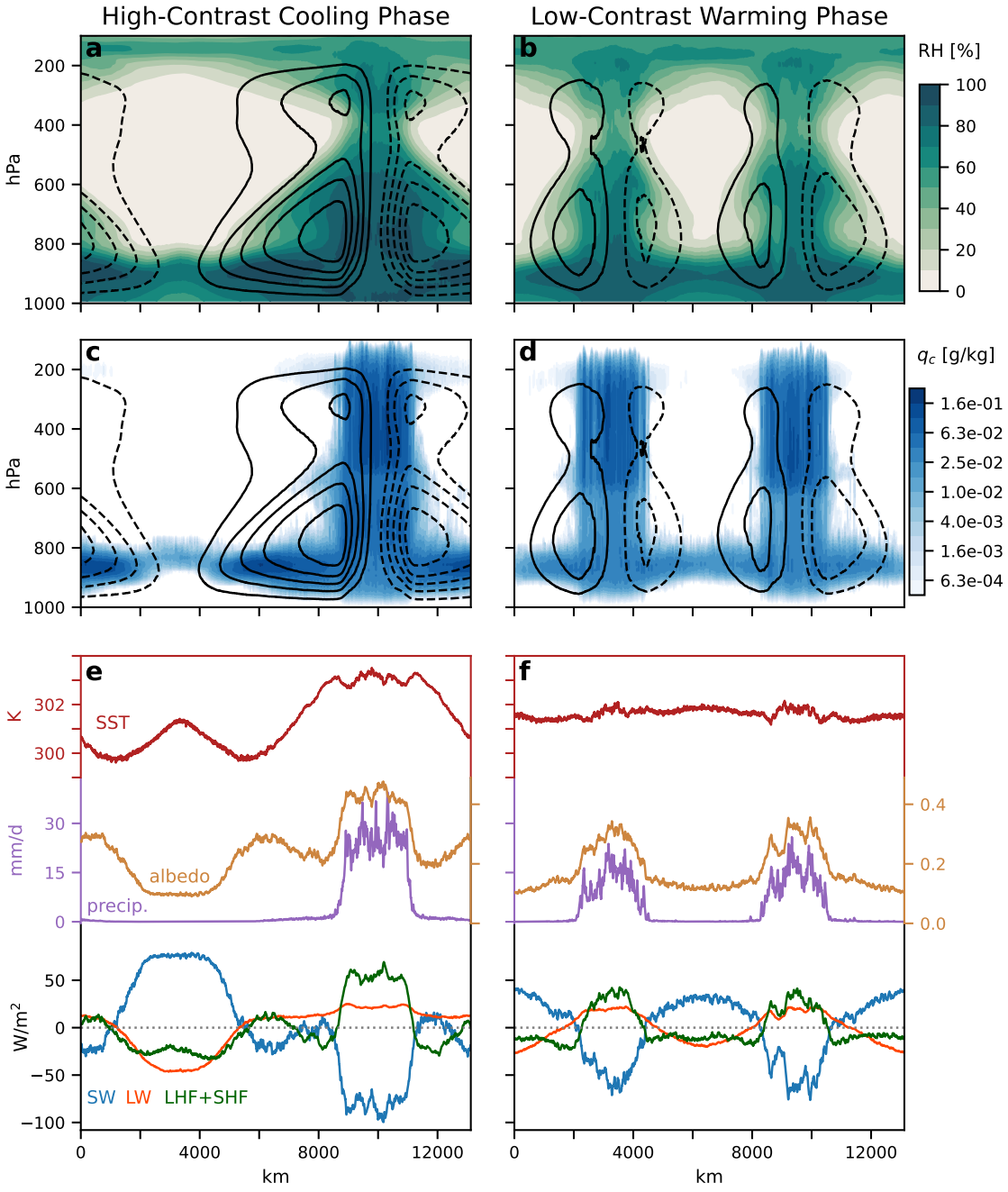

Figure 5.4: Characteristics of the (a,c,e) high-contrast cooling phase and (b,d,f) low-contrast warming phase. (a, b) Relative humidity. (c, d) Total nonprecipitating cloud condensate. Contours in (a-d) show the mass streamfunction with an interval of 4,000 kg m^{-1} s^{-1} (solid are positive; dashed are negative; zero contour not shown). (e,f) SST, albedo, precipitation, and the surface energy budget terms. Energy budget terms are expressed as anomalous fluxes with respect to the domain average, with positive values indicating downward energy flux into the surface. Data reflect the average of 2-hourly instantaneous output over 50-day periods within each phase of the cycle.

5.4e). The coldest SSTs are found at the edges of the subsiding region, while the center of the subsiding region is ∼1 K warmer than the edges (albeit still colder than the warmer convecting region; Fig. 5.4e). This "cold edge-warm center" pattern, as we shall see later on, is a critical component of the cycle of internal variability. It arises due to the contrast in SW absorption between the edges of the subsiding region, which are shaded by abundant low clouds, and the center, which is nearly cloud-free. These spatial contrasts can be understood by examining the profiles in Fig. 5.5. In the center of the subsiding region, where the large-scale circulation drives horizontal divergence near the surface, mean subsidence extends deep into the PBL, drying it out (Fig. 5.5b). As the large-scale, near-surface flow accelerates from the center of the cool region toward the convective region, the PBL becomes more turbulent and is gradually moistened, as shown by the difference in the standard deviation of w and the RH, respectively (Fig. 5.5c,d). Differences in temperature and RH at the lowest model level suggest that the lifting condensation level (LCL) decreases from 1300 m at the center of the cold region to ∼600 m at the edges, consistent with a marked increase in low cloudiness (Fig. 5.5e).

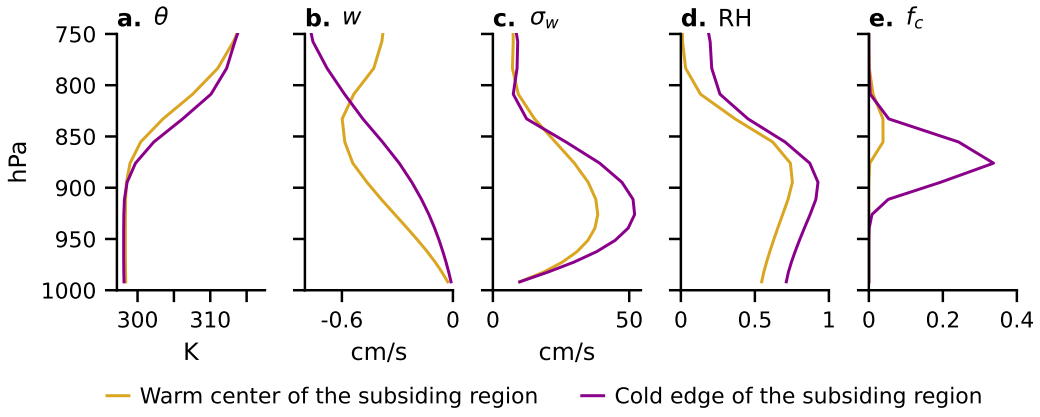

Figure 5.5: Profiles of (a) potential temperature, (b) vertical velocity, (c) the standard deviation of the vertical velocity, (d) RH, and (e) cloud fraction averaged over the (gold) relatively warm, cloud-free center and (purple) the cold, cloudy edges of the cold region. Profiles are computed from 3D output over a 50-day period during the high-contrast phase.

Because the contrast in low cloudiness across the subsiding region is relatively steady, the amplitude of the "cold edge-warm center" pattern gradually grows throughout the cooling phase of the cycle. We quantify this amplitude as $\Delta_{cp}SST$, which we define as the SST difference between the warmest 25% and the coldest 50% of the subsiding region. For this calculation, we define the subsiding region as the part of the domain where the 15-day column relative humidity is less than 0.5, which closely traces the part of the domain with below-average SST. Figure 5.2e shows that $\Delta_{cp}SST$ increases by nearly 1 K over the course of the cooling phase.

The end of the cooling phase is marked by the appearance of a second convective cell over the relatively warm center of the subsiding region. Figure 5.2e shows that this generally occurs once $\Delta_{cp}SST$ reaches $\sim$1.4 K. The new convective region begins as an organized, shallow cell with compensating subsidence on both of its sides. The subsidence causes the PBL to shoal near the cold pool edges, eroding the low clouds there. The reduction in low cloud area reduces the domain-averaged albedo, flips the sign of the net surface energy balance, and kicks off the warming phase of the cycle. This transition takes 30-50 days, and by the time the warming phase begins, the new convective region has developed mature, deep convection, and the domain-averaged low cloud fraction has been reduced by half (Fig. 5.2a-c).

5.3.2 Low-Contrast Warming phase

The warming phase is characterized by the relatively rapid homogenization of SSTs over $\sim$50 days, followed by domain-wide warming. The homogenization is achieved by the warming of the coldest SSTs at the edges of the cool, subsiding region. To understand this rapid warming, we examine the SST variance budget composited around the minimum $\overline{SST}$ for seven iterations of the cycle (Fig. 5.6a). This shows that the homogenization of SSTs, which begins at the same time that $\overline{SST}$ reaches its minimum value, is initially driven by the LHF term. The appearance of the second convective region interrupts the large-scale circulation, slowing the surface winds over the cold edges of the subsiding region and dampening surface

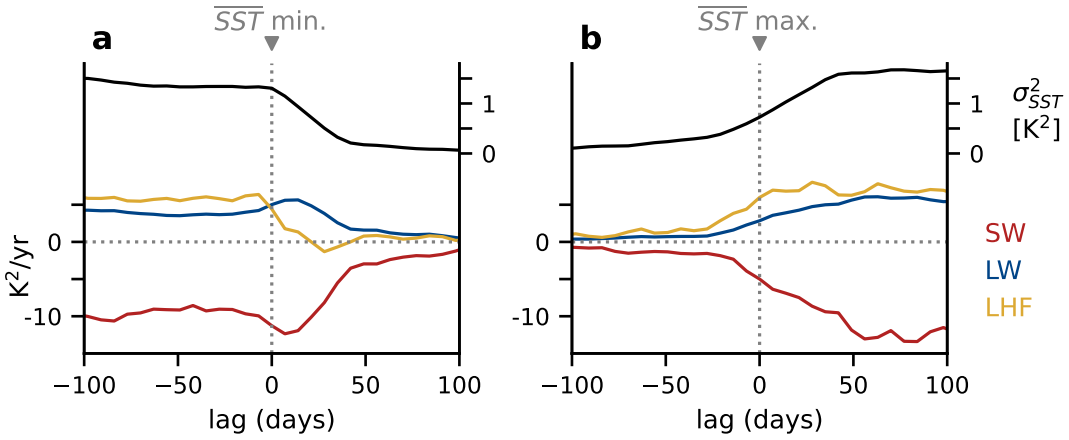

Figure 5.6: The three principal terms of the SST variance budget composited around the point in the cycle where $\overline{SST}$ reaches its **(a)** minimum and **(b)** maximum; i.e., $t = 0$ marks the end of the cooling phase in **(a)** and the end of the warming phase in **(b)**. The black lines show the composited time series of σ^2_{SST}. The composite represents the average of seven iterations of the cycle.

evaporation there. The reduction in σ_{SST} is further supported by delayed changes in the LW term: the second convective region moistens the atmosphere over the cool SSTs, inhibiting LW cooling there.

Once SSTs have been homogenized, the remainder of the warming phase is characterized by the presence of two distinct convective regions (Figs. 5.3, 5.4b) and domain-wide warming. As in the cooling phase, the convective regions are flanked by areas low cloudiness on both sides, but these areas are small and the cloud cover within them is low compared to the cooling phase. As a result, the mean low cloud fraction is smaller, albedo is lower, and the domain warms. The reduced low cloudiness relative to the cooling phase is associated with drier conditions within the PBL (Fig. 5.4a,b). The reduction in PBL moisture is consistent with the expected influence of the large-scale circulation on PBL moistening. During the warming phase, the large scale circulation is split into two overturning cells that are weaker and half as wide as the single cell present during the cooling phase. Wind shear within the PBL is greatly reduced, which would be expected to hinder the turbulent transport of

moisture up from the surface. Moreover, because each overturning cell is half as wide as during the cooling phase, the fetch of the low-level flow over the sea surface is reduced by half. Both of these factors would be expected to slow the moistening of the PBL, making it a less favorable environment for low cloud formation.

The transition out of the warming phase of the cycle is more gradual than the abrupt termination of the cooling phase. At the start of the warming phase, the conditions in the two subsiding regions are similar. As time progresses, a modest SST difference typically develops between the two subsiding regions (Fig. 5.3a), giving rise to a modest difference in surface pressure. This affects the large-scale flow in such a manner that the two convective regions drift toward one another, allowing the subsiding region with higher surface pressure to expand at the expense of that with lower surface pressure. As the two convective regions near, the large-scale circulation in the growing subsiding region strengthens, which cools the SST there via enhanced surface evaporation. As a result, SST contrast begins to develop. Fig. 5.6b shows that, on average, LHF-driven contrast starts developing about ∼30 days prior to the $\overline{SST}$ maximum at $t = 0$. The growth in SST contrast is enhanced by LW radiation as the two convective regions converge over the warmer SSTs, enhancing the water vapor greenhouse there. The large-scale circulation continuously dries the subsiding region, allowing for more efficient LW cooling over cool SSTs. When the two convective regions finally join, the large-scale circulation is again comprised of a single overturning cell, and the cooling phase starts anew.

5.4 Circulation throughout the cycle

Having generally described the cycles of internal variability, we turn now to variability in the overturning circulation, which we examine using the vertical profile of the convective mass flux M. In simple conceptual models of the tropical atmosphere, the net detrainment from convection is approximately balanced by the radiatively driven divergence in clear-sky regions, D_r:

$$\partial_p M \approx D_r \tag{5.3}$$

where M is defined as positive when the convective mass flux is upward and

$$D_r = \partial_p \omega_r \tag{5.4}$$

$$\omega_r = -Q_r / s \tag{5.5}$$

where ω_r is the radiatively driven subsidence in clear-sky regions, Q_r is the clear-sky radiative heating rate, and s is the dry static stability. Note that Eq. 5.3 is only an approximation, since radiation is not the only source of diabatic heating in clear-sky regions [*Jeevanjee*, 2022]. This conceptual model has long been used to understand the dynamics of RCE, and the vertical structure of this system is well documented in previous work [e.g., *Knutson and Manabe*, 1995; *Hartmann and Larson*, 2002; *Zelinka and Hartmann*, 2010; *Bony et al.*, 2016; *Jeevanjee*, 2022]. Briefly, there is a peak in D_r around the $\sim$220 K level arising from the rapid decline in radiative cooling rate with height there. M decreases rapidly with height at this same level, resulting in upper-level maximum in net detrainment that approximately balances the peak in D_r. The maximum in net detrainment corresponds closely to the level of peak anvil cloud formation.

Previous work has also identified robust responses of this system to surface warming. M is expected to broadly decrease with warming [*Knutson and Manabe*, 1995; *Jeevanjee*, 2022], and the upper-level maximum in D_r is expected to decrease in magnitude [*Bony et al.*, 2016; *Saint-Lu et al.*, 2020] and shift upward to lower pressure such that it maintains roughly the same temperature [*Hartmann and Larson*, 2002; *Zelinka and Hartmann*, 2010]. If Eq. 5.3 is valid, these changes in D_r would be accompanied by a similar decrease and upward shift in the upper-level $\partial_p M$ maximum. This is the basis of the Fixed Anvil Temperature and Proportionally Higher Anvil Temperature hypotheses, which specify that changes in the temperature of anvil cloud *top* are small compared to changes in surface temperature.

We use this conceptual framework to understand variability in circulation and cloudiness throughout the cycle. M is set equal to $-\omega$ for cloudy grid cells and zero elsewhere, then averaged across space and time at each vertical level. Grid cells are considered cloudy if the

total condensed water mixing ratio exceeds 10^{-5} kg/kg; precipitating condensate is included here to avoid non-physical patterns arising from the fact that the P3 microphysics scheme distinguishes between precipitating and nonprecipitating condensate for liquid but not ice.

We first examine variability in M by finding the empirical orthogonal functions (EOFs) of the daily mean profile of M from 100-850 hPa. The PBL is excluded in order to focus on free tropospheric convection. Prior to computing the EOFs, M is low-pass filtered (4th-order Butterworth filter with a 50-day cutoff) to remove the high-frequency variability associated with fast gravity wave propagation. The EOFs thus explain variability of free-tropospheric M on timescales similar to that of the internal cycle. The first two EOFs are shown in Fig. 5.7c, and their vertical gradients, which indicate net detrainment, are shown in Fig. 5.7d. Corresponding principal components (PCs) are shown in Fig. 5.7f.

The first EOF accounts for 51% of the low-frequency variance in M and represents variability driven by changes in large-scale convective organization. The corresponding PC is highly correlated with σ_{SST} (r=0.93; Fig. 5.7f), suggesting that EOF1 represents the sensitivity of M to SST contrast and the number of convective regions present across the domain. Its vertical structure shows reduced mass flux between 250-650 hPa and only minor changes in M elsewhere, which implies an increase in net midlevel (600-700 hPa) detrainment at the expense of deep detrainment aloft (Fig. 5.7c-d). This shift toward a more bottom-heavy circulation is accompanied by a decrease in anvil cloud area (not shown), as would be expected from reduced upper-level detrainment [*Zelinka and Hartmann*, 2010; *Bony et al.*, 2016]. That the circulation is more bottom-heavy when there is only one convective region is consistent with the finding by *Sokol and Hartmann* [2022] that midlevel detrainment is enhanced by convective organization in idealized RCE simulations.

To understand these changes in vertical structure, we turn to the conceptual model described earlier in this section. Figure 5.8 shows profiles of relevant quantities from the conceptual model averaged over the high- and low-σ_{SST} phases of the cycle. The averaging is done so that the mean SST_c during the two averaging periods is roughly equal (within 0.1 K), such that differences between the two periods result solely from differences in σ_{SST}

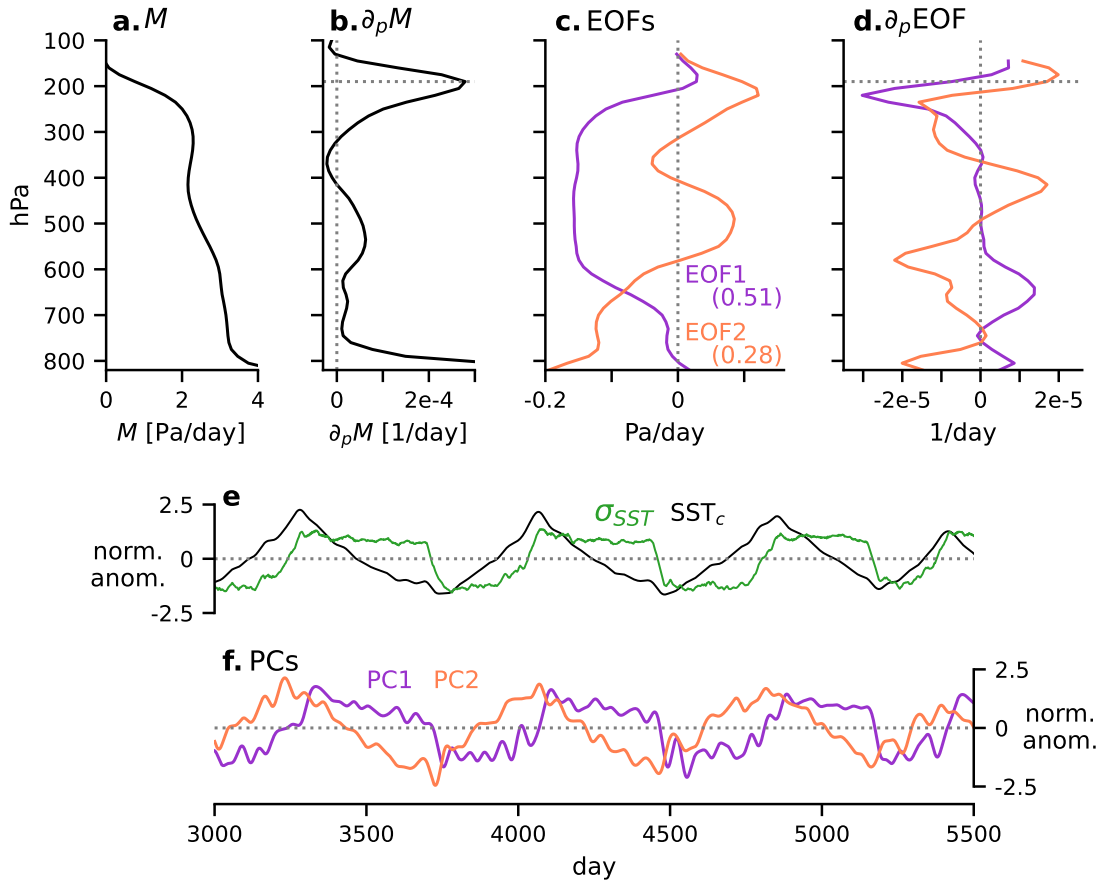

Figure 5.7: **(a)** the mean convective mass flux M and **(b)** its vertical gradient $\partial_p M$. **(c)** The first two EOFs of M and **(d)** their vertical gradient. The numbers in the EOF labels show the fraction of variance explained, and the horizontal dashed lines in (b) and (d) indicate the level of maximum $\partial_p M$. **(e)** Time series of the normalized anomalies of SST_c and σ_{SST}. **(f)** The first two principal components (PCs) corresponding to the EOFs shown in (c).

and large-scale convective organization. To achieve this balance, we only consider periods when SST_c is between 301.1-303.0 K (∼70% of the simulation). The resulting profiles of M (Fig. 5.8d) are in line with the expectations from EOF1: M is lower during the high-contrast phase between 250-650 hPa and relatively insensitive to σ_{SST} above and below that layer. This pattern is also seen in profiles of ω_r (Fig. 5.8c), which in equilibrium should roughly balance M. The reduction in ω_r during the high-σ_{SST} phase can arise from

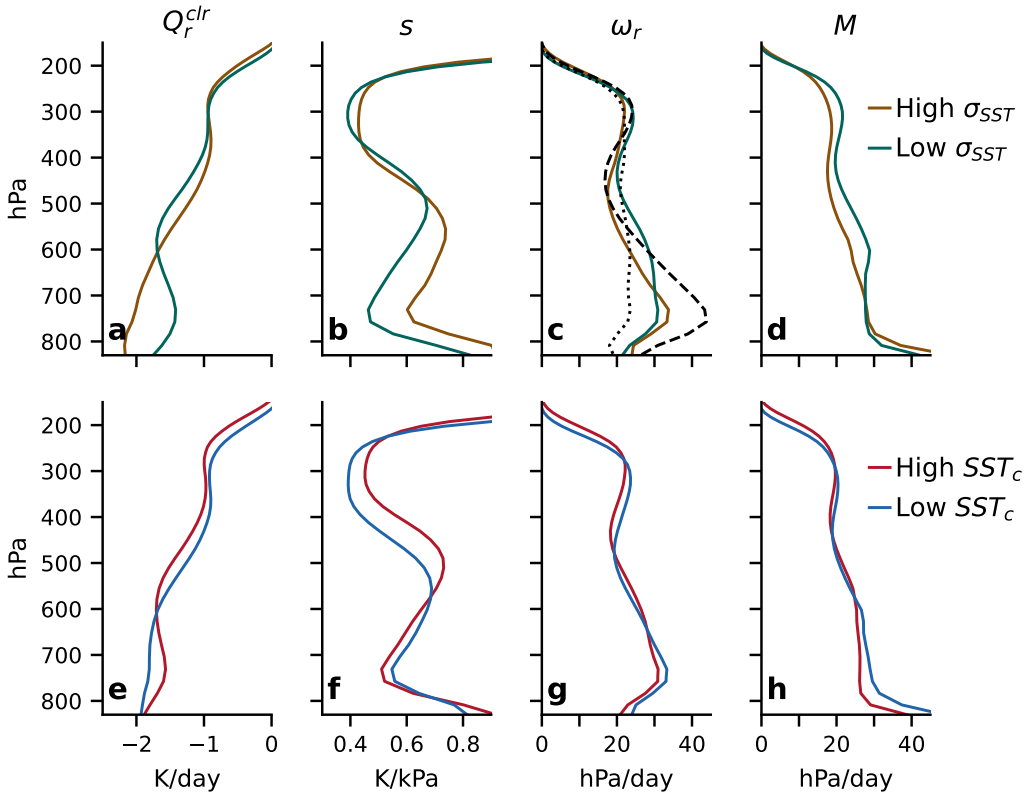

Figure 5.8: Vertical profiles comparing the (top) high-σ_{SST} and low-σ_{SST} phases and (bottom) high-SST_c and low-SST_c parts of the cycle. **(a,e)** clear-sky radiative cooling rate, **(b,f)** static stability, **(c,g)**, radiatively driven subsidence, and **(d,h)** convective mass flux. In (c), the dotted black line shows ω_r computed using Q_r from the low-σ_{SST} phase and s from the high-σ_{SST} phase; vice versa for the dashed black line.

weakened radiative cooling and/or greater stability (Eq. 5.5). The dotted line in Fig. 5.8c shows the impact of enhanced stability on ω_r during the low-σ_{SST} phase. The increase in 500-850 hPa s during the high-σ_{SST} phase acts to slow the circulation throughout all the troposphere, with the exception of a narrow layer between 350-450 hPa. The reduction in ω_r is largest at lower levels, meaning the change in s acts to reduce the bottom-heaviness of the circulation. The dashed line in Fig. 5.8c shows the impact of changes in the radiative cooling profile: the change in Q_r strengthens low-level subsidence and weakens mid-level subsidence, making the circulation more bottom-heavy. These changes result from a shift in

radiative cooling to lower levels during the high-contrast phase (Fig. 5.8a), which is a known impact of convective organization [*Emanuel et al.*, 2014]. Thus, during the high-contrast phase, changes in stability act to slow the circulation while changes in Q_r affect its vertical structure. The notable, ∼20% increase in mid- and low-level stability during the high-σ_{SST} phase will be explored in the next section.

The second EOF of M accounts for 28% of its low-frequency variance. PC2 is well correlated with SST_c (r=0.89), suggesting that EOF2 represents temperature-driven variability, that is, the impact of absolute SST on the convective mass flux. The vertical structure of EOF2 (Fig. 5.7c) contains two important features. First, it shows the expected upward shift of the M profile to lower pressure in response to SST_c warming. The upward shift is evident in the vertical gradient of EOF2 (Fig. 5.7d), which represents net detrainment and has two dipoles centered at 210 and 500 hPa. These levels coincide with the mid- and upper-level maxima in the mean detrainment profile (Fig. 5.7b), indicative of an upward shift. The shift can also be seen in Fig. 5.8e-h, in which the high-SST_c and low-SST_c averages each reflect 30% of the total simulation time and include equal time from the high- and low-contrast phases of the cycle. The second important feature of EOF2 is the general decrease in M between 600-850 hPa associated with warmer SST_c, which is also seen in Fig. 5.8h. This, too, is in line with the expectation that M decreases as the surface warms. Here, the decrease in M applies only from 600-850 hPa; at higher levels, warmer surface temperatures drive compensating changes in radiative cooling and static stability such that ω_r and M are relatively unaffected. As a result, the profile of M is more bottom-heavy during the cooler parts of the cycle, although the difference in vertical structure is significantly smaller than that associated with changes in σ_{SST} and convective organization.

The EOF analysis shown here provides a convenient separation between σ_{SST}-driven and SST_c-driven variability in the convective mass flux, which we interpret here as variability driven by convective organization and temperature, respectively. The dominant mode of low-frequency M variability is the organization-driven trade-off between the deep and congestus modes of the large-scale overturning circulation. SST_c-driven variability is secondary and

acts primarily to shift the profile of M such that its main features maintain roughly constant temperature. It seems likely that the relative importance of organization- and temperature-driven variability is sensitive to the organization and SST_c cycle amplitudes. For example, if the range of SST_c realized throughout the cycle were doubled but the cycle of convective organization remained the same, SST_c could feasibly overtake convective organization as the dominant driver of M variability.

5.5 Tropospheric stratification throughout the cycle

We now examine how the dry static stability, s, of the free troposphere varies throughout the internal cycle. Stability affects many important tropical phenomena, such as convective intensity and overturning circulation strength [*Singh and O'Gorman*, 2015; *Knutson and Manabe*, 1995; *Sohn et al.*, 2016]. Here, we are interested in stability because of its role in modulating the M variability discussed in the previous section.

In pressure coordinates, the static stability s is given by

$$S = -\frac{T}{\Theta}\frac{\partial \Theta}{\partial p} = (\Gamma_d - \Gamma)/\rho g. \tag{5.6}$$

where θ is potential temperature, Γ the lapse rate, and Γ_d the dry adiabatic lapse rate. Free-tropospheric s is known to be affected by several factors. The first is the temperature and humidity of the sub-cloud layer in the convecting region, which determine the moist adiabatic temperature profile assumed by rising convective updrafts [*Betts*, 1982; *Xu and Emanuel*, 1989]. The convective temperature profile is efficiently transmitted across the Tropics by gravity waves [*Bretherton and Smolarkiewicz*, 1989], which couples the Tropics-wide s to the SST in the convective region. Because warmer moist adiabats are more stable, we expect warmer SSTs to be associated with greater s [*Knutson and Manabe*, 1995; *Bony et al.*, 2016]. Second, s is affected by the deviations of rising updrafts from an undiluted moist adiabat. These deviations, which decrease s, arise from the entrainment of dry air into convective updrafts [*Bao and Stevens*, 2021; *Becker and Hohenegger*, 2021; *Keil et al.*, 2021; *Wing and*

Singh, 2024]. Their magnitude depends on the entrainment rate, ϵ, and the saturation deficit of the entrained air. If ϵ is large and/or ambient air is dry, updrafts will follow a less stable temperature profile. When convection is highly organized, updrafts are surrounded by air that is, on average, moister. Therefore, under constant ϵ, greater convective organization is associated with reduced entrainment drying, and convective updrafts adhere more closely to an undiluted moist adiabat. Following *Becker et al.* [2018], we refer to this effect as the "moist shell" effect, which implies an increase in s with greater convective clustering. Finally, vertical gradients in Q_r are thought to affect s, both in the real Tropics [*Mapes and Zuidema*, 1996] and idealized RCE simulations [*Sokol and Hartmann*, 2022]. We diagnose the tendency of s due to radiative heating as $(\partial_t S)_r = -\partial_p Q_r$. While other processes may also affect s, we will show that the s variability examined here can be largely explained by these three factors.

Figure 5.9a-b shows that s variability throughout the cycle has different drivers in different parts of the troposphere. Between the freezing level and ∼250 hPa, monthly mean s anomalies closely follow those in SST_c (r^2=0.7-0.9, depending on the pressure level; Fig. 5.9b). The association of warmer SST_c with enhanced upper-level stability is consistent with the expectations outlined above: when SST_c is anomalously warm, isotherms shift upward to lower pressure. Since the moist adiabatic lapse rate is primarily a function of temperature, the lapse rate at fixed pressure decreases (s increases) as the surface warms.

On the other hand, between the top of the PBL and the freezing level, monthly mean s is entirely uncorrelated with SST_c (Fig. 5.9b). Rather, variability in s at these levels follows variability in σ_{SST} (r^2 =0.6-0.7). s is large during the high-contrast phase of the cycle, when there is one convective region, and small during the low-contrast phase, when there are two. This pattern is seemingly consistent with the "moist shell" effect described above, in which greater convective clustering mitigates the effects of entrainment on the temperature profile. In the remainder of this section, we consider whether the moist shell effect can indeed account for this pattern of s variability. For this analysis, we compare two 50-day periods for which the full, vertically resolved model output is available: one high-contrast period (day

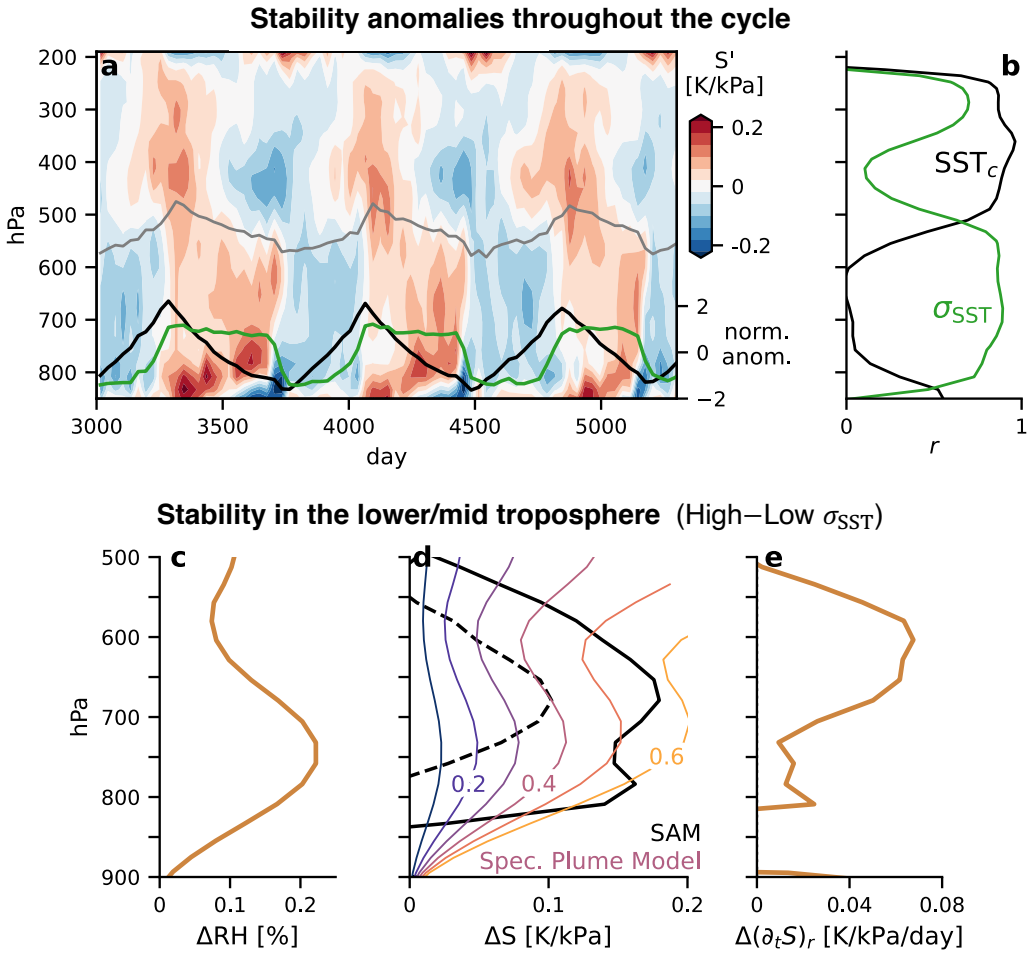

Figure 5.9: **(a)** Shading shows monthly s anomalies. The grey line shows the freezing level. Normalized anomalies of SST_c (black) and σ_{SST} (green) are shown on a separate y-axis. **(b)** Correlation coefficients between monthly mean s and (black) SST_c and (green) σ_{SST}. **(c)** Difference in convective-region RH between the high- and low-contrast phases. **(d)** Black: difference in (solid) the domain mean stability $\Delta\overline{s}$ and (dashed) the convective-region stability Δs_c. Colored lines: difference in s predicted by the spectral plume model for various entrainment rates (expressed in km^{-1}.) and a LCL of 500 m. **(e)** difference in domain-averaged $(\partial_t S)_r$. Note the difference in y-axis limits between the top and bottom rows.

7620-7670) and one low-contrast period (day 7800-7850). The two periods were chosen to have equal SST_c, ensuring that differences in s reflect differences in large-scale convective

organization. To identify convective regions, we compute the 50-day, 400-700 hPa mean ω at each grid point then block-average the domain into 162-km blocks. Blocks with mean ascent are defined as the convective regions, and our results are not very sensitive to the details of this procedure.

Figure 5.9d shows the difference in domain-averaged stability ($\Delta\overline{s}$) and convective-region stability (Δs_c) between the high- and low-contrast periods. Surprisingly, $\Delta\overline{s}$ is significantly larger than Δs_c throughout the 500-800 hPa range. This indicates (1) that the model domain is long enough to support non-negligible horizontal temperature gradients, and (2) that convective-region processes can only explain some of the relationship between s and σ_{SST}. At $\sim$800 hPa, $\overline{s}$ is affected by the stability at the top of the PBL in nonconvecting regions, which varies throughout the cycle due to low cloud variability. Above this level, the difference between $\Delta\overline{s}$ and Δs_c must arise from diabatic processes in the subsiding region(s), which are limited to radiative cooling. Fig. 5.9e shows that $(\partial_t s)_r$ is greater during the high-contrast period, meaning that changes in the profile of Q_r act to enhance s during the high-contrast phase. As discussed in section 5.4, this results from a shift in the Q_r profile to lower levels, a known effect of convective aggregation [*Emanuel et al.*, 1994].

Recognizing that radiative cooling plays a significant role in s variability, we now focus exclusively on Δs_c and consider whether it can be attributed to the moist shell effect. The basis of the moist shell effect is that the ambient air entrained into convective updrafts is more humid when convection is more aggregated. Indeed, Fig. 5.9c shows that the mean convective-region RH is significantly greater during the high-contrast phase, with the largest difference of 0.22 found at 750 hPa. To test whether this RH enhancement can explain Δs_c, we employ the spectral plume model (SPM) developed by *Zhou and Xie* [2019]. The SPM can be used to construct the equilbrium temperature profile resulting from a spectrum of convective plumes with varying entrainment rates and levels of neutral buoyancy. We use the SPM to find the Δs_c resulting from the environmental RH enhancement shown in Fig. 5.9c, assuming negligible changes in the ϵ_0 between the high- and low-contrast phases. Our implementation of the SPM takes as inputs a cloud-base entrainment parameter ϵ_0 and a

profile of environmental RH, among others, and outputs a profile of s. The full details of our model implementation and experimental protocol can be found in section 5.9.1. Since the entrainment rate cannot be diagnosed directly from out model output, we test a range of reasonable values for ϵ_0 informed by a recent analysis by *Hu et al.* [2023], which used the same model and a similar horizontal resolution (4 km rather than our 3 km) as our simulation.

The colored lines in Fig. 5.9d show the SPM-estimated Δs_c due to the moist shell effect for various values of ϵ_0. The SPM-predicted profiles and the SAM-simulated Δs_c (dotted black line) have different shapes throughout the lower troposphere, which is to be expected due to the many simplifying assumptions made by the SPM. Our goal here is simply to determine whether the SPM predicts stability enhancement of the same order of magnitude as the SAM-simulated Δs_c. For $\epsilon_0 = 0.2$-0.4 km^{-1}, the SPM-predicted stability enhancement is on par with the SAM-simulated Δs_c between 550-750 hPa. This range of ϵ_0 overlaps with the diagnosed entrainment rate of 0.25 km^{-1} in *Hu et al.* [2023] for SAM simulations with a horizontal resolution of 4 km. This suggests that the enhancement of RH within convective regions can, under typical entrainment rates, produce an increase in midlevel s that is commensurate with the change in midlevel s throughout the cycle. We therefore find support for the moist shell explanation of midlevel s variability, with two important caveats. First, we have assumed constant entrainment rates between the high- and low-contrast phases of the cycle. Second, while the moist shell effect may plausibly explain s variability within the convective region, variability in domain-averaged s cannot be explained by convective processes alone and is very likely influenced by radiative cooling.

5.5.1 Summary of s variability and applicability to the real Tropics

We have found that internal s variability is controlled by different factors at different levels, with a clear split between SST_c-modulated and organization-modulated parts of the troposphere (Fig. 5.9b). This finding, however, is likely sensitive to the amplitude of internal variability in SST_c and convective organization; for example, the effect of SST_c on midlevel

S could feasibly overtake that of convective organization if the amplitude of the SST_c cycle were greatly increased but the cycle of organization remained unchanged. To understand the applicability of these findings to the real Tropics, we examine S variability in ERA5 reanalysis. Using 4x daily reanalysis data from the equatorial Pacific, we compute monthly mean SST_c and two proxy metrics for convective organization. The first is σ^2_{CRH}—the spatial variance of the column relative humidity (CRH)—which is a well established metric of large-scale convective organization [e.g., *Wing et al.*, 2017]. The second is σ_{SST}, which has been used as a metric of organization in modeling studies [e.g., *Tompkins and Semie*, 2021] but not, to our knowledge, in observational assessments. While σ_{SST} and convective organization track each other very closely in our simulation, we caution that a relationship between σ_{SST} and organization in the real world has not been established. Nevertheless, we include it here for comparison with the simulation. A description of how these metrics are calculated from the reanalysis data is given in 5.2.3.

The relationships between s and the three predictor variables (SST_c, σ_{SST}, and σ^2_{CRH}), shown in Figure 5.10, are generally weaker in ERA5 than in the model simulation. This is to be expected, since there are many factors that may affect s in the real world that are not included in the idealized RCE simulation. However, as in the model simulation, the strength of the s-SST_c relationship in ERA5 is strongest in the upper troposphere (250-500 hPa), while the relationships with the two organization proxies are strongest in the mid-troposphere (400-700 hPa). That the SST_c- and organization-modulated levels align so well with the simulation is somewhat surprising given the simplicity of our analysis and the indirect nature of the two proxies for convective organization. While the dependence of upper-level s on surface temperature has been documented in previous work [*Saint-Lu et al.*, 2020], the dependence of midlevel s on convective organization has not, to our knowledge, been examined in any observationally derived data. Because σ_{SST} and σ^2_{CRH} are only indirect proxies of organization, and because tropospheric temperature in the equatorial Pacific could be affected by factors outside of our reanalysis study region, we caution against a causal interpretation of this result. Nevertheless, this finding is consistent with the simulation

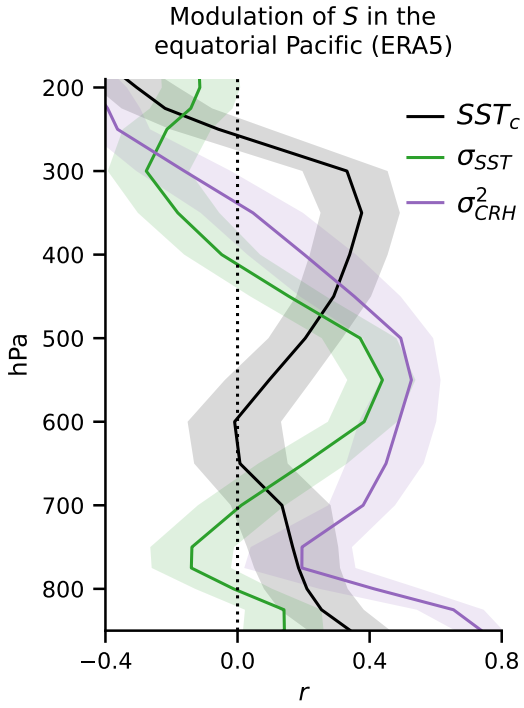

Figure 5.10: Vertical profiles of the correlation coefficient between monthly mean s and (black) SST_c, (green) σ_{SST}, and (purple) σ^2_{CRH}in ERA5. Data reflect the equatorial Pacific. Shading shows the 95% confidence interval generated from 10,000 bootstrapped samples.

results, and it underscores the fact that the physical mechanisms connecting s, SST_c, and convective organization are rooted in first principles and may therefore be expected to apply to the real Tropics. This can be summarized by the following two insights:

1. The impact of surface temperature on tropospheric temperature and stratification is amplified aloft. This has long been known [*Manabe and Stouffer*, 1980] and arises from the physics of idealized, moist adiabatic ascent.

2. The influence of the "moist shell" effect on stratification decreases with height. At upper levels, cold temperatures reduce the saturation deficit of environmental air entrained into convective updrafts. Since the impact of entrainment on the temperature profile is weaker at the cold temperatures, the same amount of environmental RH en-

hancement should have less of an effect in the upper troposphere than at lower levels.

As we shall see in the next section, these insights into tropospheric stratification can help understand the internal variability of the convectively driven overturning circulation.

5.6 Sensitivity of the cycle to domain length

5.6.1 Additional model runs

To test the sensitivity of the cycle to the length L of the 2D model domain, we conducted similar simulations with various values of L, all shorter than the control run described above (L=13,122 km). The exact values of L, shown in Table 5.1, were chosen to provide a spread in domain sizes while meeting computational requirements.

These simulations are configured as similarly to the control run as possible, with a few exceptions. First, the sensitivity runs are only integrated for 2,000 days after the initial 100-day spin-up period that uses a shallower mixed-layer. Second, to meet SAM's computational requirements, the run with L =10,800 km uses 90 vertical levels instead of 81. The 90-level grid is constructed by extending the 81-level grid upwards using a layer depth equal to the uppermost layer of the 81-level grid. The bottom of the damping layer is kept at the same altitude in all simulations. Lastly, the Q-flux is adjusted for the sensitivity runs in order to keep the time-averaged SST as similar to the control as possible (Table 5.1). These values were selected based on trial and error.

5.6.2 Sensitivity test results

We find that the cycle of internal variability described in the sections above is present in the runs with L = 13,122 and 11,664 km but absent in the runs with smaller domains (Table 5.1, Fig. 5.11). For the smallest domain (L =7,776 km), SST is nearly uniform in space and time. But for L = 10,800 and 9,720 km, there is significant SST variance across the domain, yet $\overline{SST}$ is steady over time. These runs resemble the high-σ_{SST}, cooling phase of the control run, with well defined warm and cold regions, a single convective region over the warm SSTs,

and two regions of enhanced low cloudiness flanking the convective region. But, unlike in the control run, this state is stable over the integration times tested here. We therefore seek to understand why the cycle disappears as L decreases even when high σ_{SST} persists.

It was shown in section 3.1 that, in the control run, the end of the cooling phase occurs when the "cold edge-warm center" SST pattern within the cold region reaches a certain amplitude. The center of the cold region becomes progressively warmer than its edges until a second convective region develops in the relatively warm center. The cold edge-warm center pattern is present in all of the runs with significant σ_{SST}, but its amplitude greatly diminishes as L becomes smaller. Figure 5.11c shows $\Delta_{\mathrm{cp}}SST$ for all of the runs in which the cold edge-warm center pattern is present. In the two cycling runs (L =13,122 and 11,664 km), $\Delta_{\mathrm{cp}}SST$ grows throughout the cooling phase until the appearance of a second convective region, whereas in the non-cycling runs $\Delta_{\mathrm{cp}}SST$ remains relatively steady at low values, reflecting more homogeneous SSTs within the cold region. We hypothesize that the stunted growth of this SST pattern in smaller model domains inhibits the instability that brings about the end of the high-σ_{SST} phase, shutting down the cycle of internal variability.

We must then ask why the cold edge-warm center SST pattern weakens as L decreases. Fig. 5.11d shows the contrast in surface energy flux terms between the warm center and cool edges of the subsiding region. For these calculations, we compare the high-σ_{SST} cooling phase

L (km)	Q-flux (W/m^2)	SST (K)	σ_{SST} (K)	Cycle?
13,122*	35	301.2	0.83	Yes
11,664	40	300.2	0.75	Yes
10,800	27.5	299.7	1.08	No
9,720	32.5	298.9	0.95	No
7,776	45	302.6	0.38	No

*control run.

Table 5.1: Details for the sensitivity tests of varying domain length L. SST and σ_{SST} represent averages over time (not including the equilibration period).

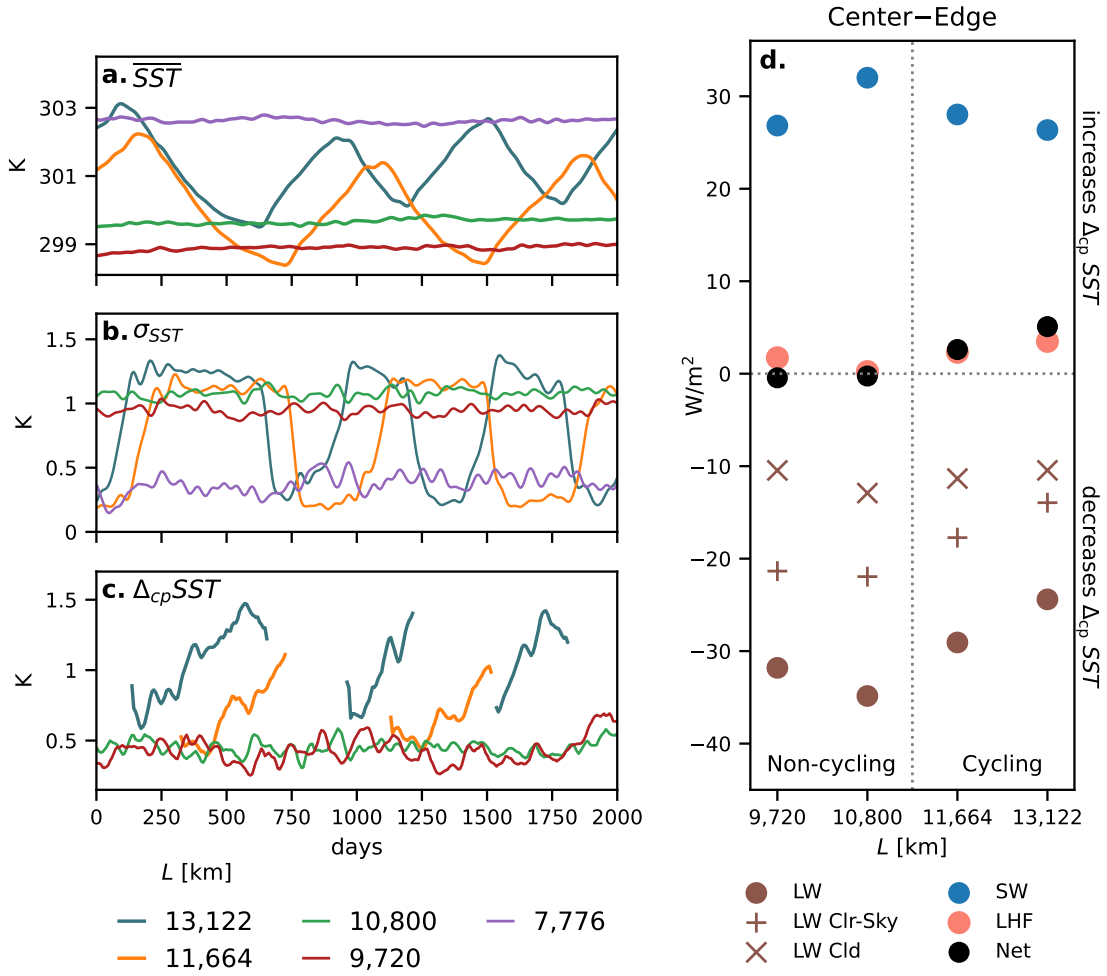

Figure 5.11: Weekly average (a) $\overline{SST}$, (b) σ_{SST} and (c) $\Delta_{cp}SST$ for model runs with various domain lengths (L). The run with L =7,776 km is not shown in (c) because it does not have the cold edge-warm center SST pattern, so $\Delta_{cp}SST$ is undefined. Note that the beginning of the 2,000-day record shown in the figure corresponds not to the beginning of each simulation but to the beginning of the selected study period for each run. (d) Contrast in surface energy budget terms between the warm center and cold edges of the subsiding region; positive values act to increase the amplitude of the cold edge-warm center SST pattern and negative values act to dampen it.

of the cycling runs with the steady state of the two non-cycling runs that have substantial σ_{SST}. We first compute the time-averaged surface fluxes over an entire iteration of the cooling phase for the cycling runs (a 275-day period for L = 13, 122 km and a 391-day

period for $L = 11{,}664$ km) and over an arbitrary 275-day period for the non-cycling runs. We then normalize the x coordinate of each run by the total domain length L such that $0 < x < 1$. We determine the location of the relatively warm center of the cold region, x', by locating the local SST maximum. Mean surface flux terms are computed over the interval $x' - 0.03 < x < x' + 0.03$, which we take to be representative of the relatively warm center of the cold region. We then compute mean fluxes for the colder edges of the cold region by averaging over $x' - 0.15 < x < x' - 0.09$ and $x' + 0.09 < x < x' + 0.15$, which corresponds to the local SST minimum in the control simulation.

Since the cold edge-warm center pattern itself is caused by a contrast in low cloudiness, we may first suspect that changes in pattern amplitude are driven by changes in SW contrast. However, Fig. 5.11d shows that this is not the case; rather, changes in SW flux at the surface act to *increase* the amplitude of the SST pattern as L decreases from the control run to 10,800 km. On the other hand, changes in LW and, to a much lesser degree, LHF both act to weaken the pattern over this range of L. The changes in LW contrast between the center and edges of the cold region are mostly due to clear-sky effects, with clouds playing a very minor role. The physical interpretation of this is that, as L decreases from the control run to 10,800 km, the greenhouse effect over the center of the cold region weakens relative to that over the edges, and LW cooling of the surface becomes more efficient over the center. This change results from a drying of the free troposphere over the center of the cold region as L decreases (not shown). This enhanced surface cooling prevents the growth in amplitude of the cold edges-warm center SST pattern.

The important takeaway from this sensitivity analysis is that SST patterns within the subsiding region are a critical component of the cycle of internal variability in the control run. The high-σ_{SST} state associated with the cooling phase of the cycle is stable on longer timescales if the cold edge-warm center SST pattern is reduced in amplitude or absent entirely. Changes in the amplitude of the SST pattern can be brought about by changes in the moisture content of the free troposphere in the subsiding region; understanding the dynamic and thermodynamic controls on humidity in tropical clear-sky regions may thus be

of interest in studies of tropical variability.

5.7 Sensitivity of the cycle to mean climate

In these section we provide a brief overview of the sensitivity of internal variability to forced changes in $\overline{SST}$. We conducted several additional simulations in which we perturb the mean climate by changing the value of the Q-flux (Table 5.2). The simulations are identical to the control run in all other respects, and all use the same domain length (L= 13,122 km). Two of the runs are initialized from day 4,000 of the run with Q=32.5 W/m^2 (Table 5.2, Fig. 5.12); the remainder are initialized in the same manner as the control run: beginning with uniform SST, the model is run for 100 days with a 10-m mixed layer before the mixed-layer depth is switched to 25 m, marking day 0.

As shown in Fig. 5.12, the character of internal variability is very sensitive to the mean climate. The internal cycle described in this chapter is present in all of the runs that have a mean SST close to that of the control run, regardless of the Q-flux. In the cooler climate (Q=50 W/m^2), there is an internal cycle that is clearly different in nature from that in

Q-flux (W/m^2)	SST (K)	σ_{SST} (K)	Cycle?
25[1]	N/A[2]	0.86	No
30	309.9	0.89	No
30[1]	301.8	0.98	Yes
32.5	301.7	0.83	Yes
35*	301.2	0.83	Yes
50	299.2	0.56	Yes (modified)

*control. [1]branched from day 4,000 of the run with Q=32.5 W/m^2 (Fig. 5.12).
[2]equilibrium SST was not reached.

Table 5.2: Details for the sensitivity tests with different mean climates achieved by changing the Q-flux. Results reflect the last 2,000 days of each run with the exception of the control run (Q=35 W/m^2), for which we use the same time period used for the rest of the chapter.

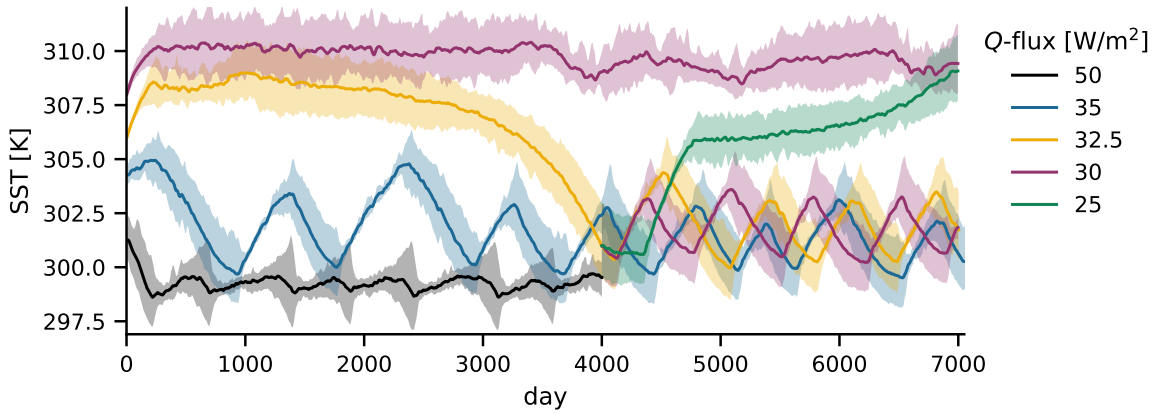

Figure 5.12: $\overline{SST}$ (lines) for the sensitivity tests with different Q-fluxes. The blue line is the control run that is the primary subject of this chapter. Shading is between the 10th and 90th SST percentiles found across the domain.

the control (black line in Fig. 5.12). The amplitude of $\overline{SST}$ variability is greatly reduced compared to the control, and the warming phase is significantly longer than the cooling phase. SST contrast grows gradually throughout the warming phase and continues to grow throughout the onset of the short cooling phase. The contrast then abruptly collapses, at which point the warming phase starts again. This suggests that the coupling between $\overline{SST}$ and σ_{SST} in this model setup is dependent on the mean state.

In warmer climates, such as that achieved in the run with Q=30 W/m^2 (purple line in Fig. 5.12), there is high SST contrast but no regular cycle of variability; rather, $\overline{SST}$ is relatively steady for the entire 7,000-day simulation period. We refer to this warmer run as SST310. In the control run, high SST contrast is associated with decreasing $\overline{SST}$ due to the abundance of low clouds that form in high-contrast conditions. That $\overline{SST}$ is steady in SST310 run despite high contrast suggests that low cloud fraction is smaller in SST310 than in the control. Indeed, low cloud fraction in SST310 is $\sim$0.19 (not shown), much smaller than the mean of $\sim$0.31 during the high-contrast phase of the control run. Why is this the case? Further investigation of SST310 reveals a significant shift in the relationship between deep convection and SST. This can be seen in Figure 5.13, which shows Hovmöller diagrams of

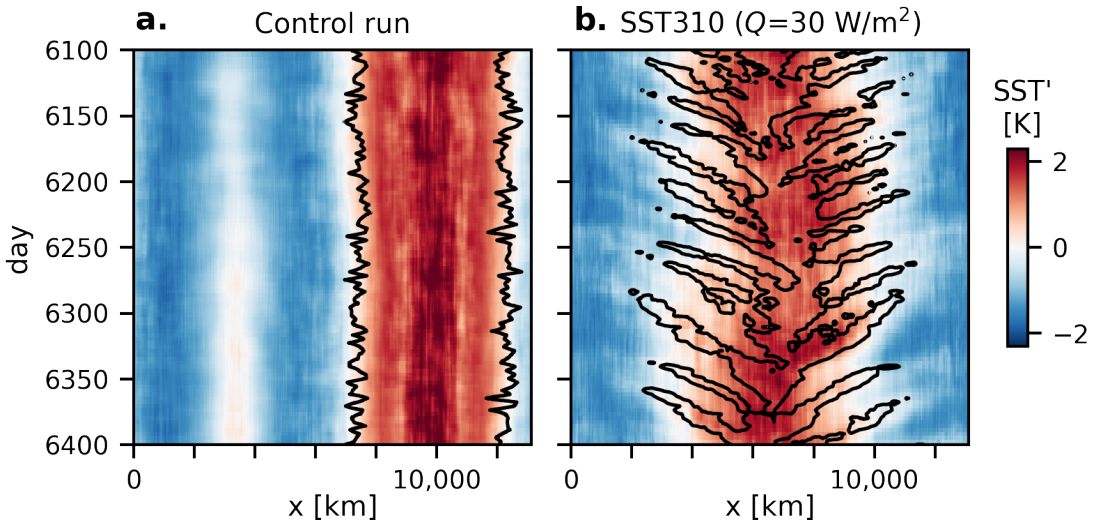

Figure 5.13: Hovmöller diagrams of SST', the SST anomaly relative to the instantaneous domain average, for (a) the control run and (b) SST310, the warm, non-cycling run with Q=30 W/m^2. The black contour shows CRH above 0.6 and is intended to loosely trace the parts of the domain with active convection. Note: domain-average SSTs vary with time and between the two panels, so the same SST' does not indicate the same absolute SST.

SST and the moist convective envelope for a 300-day period of the control run and SST310. In the high-contrast phase of the control run, the moist region remains parked over the warmest SSTs. On the other hand, in SST310, convection develops as a narrow cell over relatively moderate SSTs and is advected by the mean flow towards the warm pool. New convective regions develop on each side of the warm pool every ∼25 days, giving rise to the fishbone pattern seen in Fig. 5.13b. The systems develop on the edges of the cool, subsiding region, exactly where low clouds are most abundant in the control run. This inhibits the development of a moist, capped PBL and suppresses low cloud formation, ultimately allowing $\overline{SST}$ to reach a steady state. Thus, in a warmer climate, a shift in SST-convection dynamics leads to a fundamental change in the nature of internal variability. Future work will seek to explain this shift in dynamics and understand its applicability to the real Tropics.

These sensitivity tests demonstrate several other interesting properties of the coupled

RCE system. First, multiple equilibria are possible for the same Q-flux depending on initial conditions. Whereas SST310 enters a warm, non-oscillatory state of high contrast, a run with the same Q-flux (30 W/m^2) initialized in the cool, oscillatory regime remains in that regime. Second, time-averaged SSTs between ∼303 and ∼309 K are unstable on long timescales. Fig. 5.12 shows that the runs with SSTs in this range eventually enter the warmer, non-oscillatory regime or the cooler-oscillatory regime. It seems exceedingly likely that this result is specific to this model and/or experimental configuration; nevertheless, understanding why it is the case may lead to valuable insights and may be explored in future work.

5.8 Summary and Conclusion

This chapter has examined internal variability in a ∼20-year, cloud-resolving, coupled RCE simulation. The model produces internal oscillations in which the mean SST, the spatial pattern of SST, and the large-scale organization of deep convection vary systematically. These oscillations are summarized in Figure 5.14. Strong spatial contrasts in SST are associated with enhanced convective organization, greater low cloudiness, and mean SST cooling. On the contrary, uniform SSTs are associated with reduced convective organization, suppressed low cloudiness, and mean warming. The internal oscillations generated by these two regimes share certain characteristics with previously described GCM experiments [*Coppin and Bony*, 2017; *Drotos et al.*, 2020; *Dygert and Hartmann*, 2023] but are unique amongst them, and this is the first description of such variability in a cloud-resolving model.

In addition to describing the cycle in detail, we have also leveraged the model's internal variability to understand various aspects of the tropical overturning circulation and the stratification of the free troposphere. When convection is highly organized during the cooling phase of the cycle, the overturning circulation is more bottom heavy and the lower half of the free troposphere is more stable than during the warming phase. Both of these shifts are due in part to changes in the vertical profile of radiative cooling. We further found that the moist shell effect could plausibly explain part of the enhanced stratification. A key takeaway from this analysis was that organization-driven variability in the strength and structure

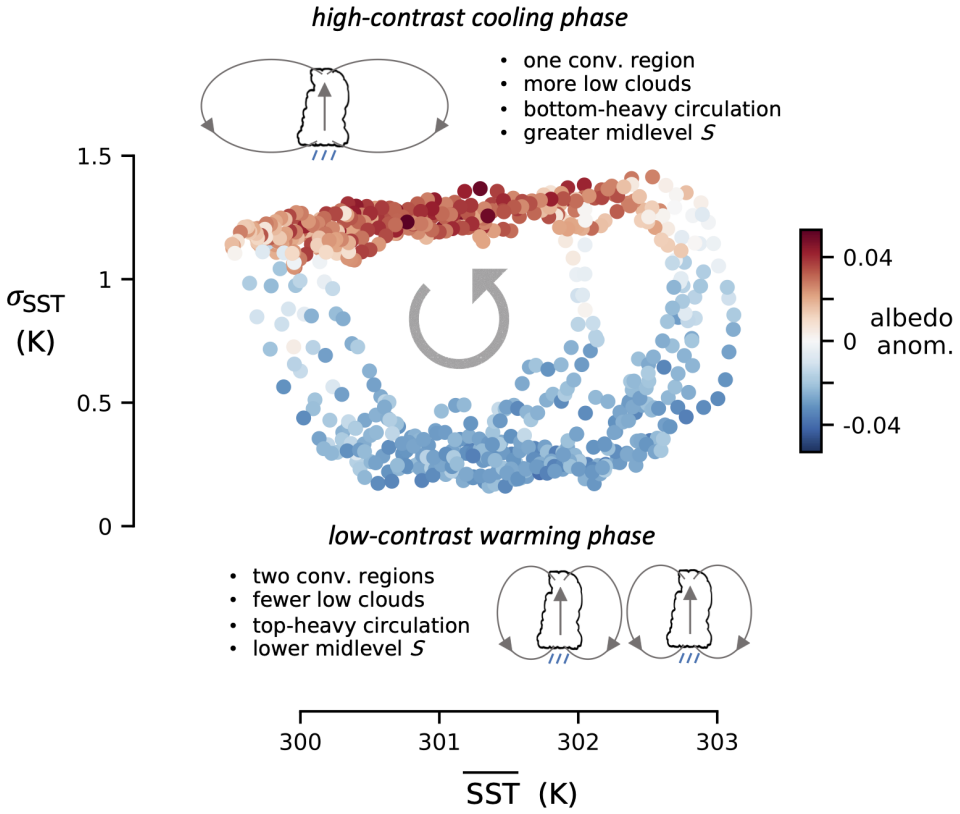

Figure 5.14: Overview of the cycle in $\overline{SST}$-σ_{SST} phase space. Each scatter point represents a 7-day period and is shaded according to the domain-averaged albedo anomaly. Low-contrast and high-contrast refer to the amount of SST variability across the domain. The circular arrow represents the direction in which the cycle progresses over time.

of the tropical circulation can be just as, if not more, significant than temperature-driven variability.

An additional source of uncertainty in this analysis is the degree to which 2D simulations are representative of the 3D tropical atmosphere. Fully understanding the dimensional dependence of convective organization is beyond our scope here, but a previously published result suggests that differences between 2D and 3D simulations of convective organization are minor [*Yao and Yang*, 2023].

The sensitivity tests discussed in sections 5.6 and 5.7 have generated several questions

that remain unanswered. What sets the lengthscale of the tropical overturning circulation cell? What is the role of SST patterns in setting this lengthscale? And what explains the strong and abrupt dependence of internal variability on the mean SST? These questions will be investigated in future work.

5.9 Supplementary Information

5.9.1 Spectral Plume Model Calculations

To understand changes in static stability throughout the cycle, we employ the spectral plume model (SPM) developed by *Zhou and Xie* [2019] (hereafter ZX19). The SPM builds on the zero-buoyancy plume model developed by *Singh and O'Gorman* [2013] and can be used to understand the vertical structure of the atmosphere resulting from a spectrum of entraining plumes with different levels of neutral buoyancy. Its equations predict the deviation of the mean moist static energy (h) profile from an undiluted moist adiabat. The formulation used here, copied from ZX19, is

$$\frac{d\Delta h}{dz} - \lambda \Delta h = -\epsilon(z)(1 - RH)\frac{L_v \overline{q_v^*}}{C_p} \tag{5.7}$$

$$\lambda \cong \frac{1}{1 + \eta\epsilon(z)(z - z_b)}\frac{d\ln\epsilon}{dz} \tag{5.8}$$

where Δh is the deviation of the mean h profile from that of an undiluted moist adiabat, $\overline{q_v^*}$ is the saturation vapor pressure of the entrained environmental air, L_v is the latent heat of vaporization, and C_p is the specific heat capacity of air at constant pressure. η is a constant equal to 0.75, as shown in ZX19. $\epsilon(z)$ is the entrainment rate of a plume reaching its level of neutral buoyancy at height z and is given by

$$\epsilon(z) = \begin{cases} \epsilon_0 \left(\frac{z_t - z}{z_t - z_b}\right)^k, & z_b < z < z_t \\ 0, & \text{elsewhere} \end{cases} \tag{5.9}$$

where ϵ_0 is the cloud-base entrainment rate, z_t is the top of the convectively mixed layer, z_b is the height of cloud base (i.e., the LCL), and, following ZX19, $k = 1$.

As shown in ZX19, Eq. 5.7 can be integrated upward to find the vertical profile of Δh. The deviation of the mean temperature profile from the undiluted moist adiabat can then be found by

$$\Delta T(z) = -\left(1 + \frac{L_v}{R_v \overline{T}^2} \frac{L_v \overline{q_v^*}}{C_p}\right)^{-1} \Delta h \tag{5.10}$$

where R_v is the gas constant for water vapor and $\overline{T}$ is the environmental temperature profile equal to $T^u + \Delta T$, where T^u is the temperature of the undiluted moist adiabat.

Our implementation of the SPM takes the following paramters as inputs: the near-surface air temperature T_0, the LCL, ϵ_0, and a vertical profile of environmental RH. We find T_0 by extrapolating the temperature at the lowest model level to the surface along a dry adiabat. We then use T_0 to construct the undiluted moist adiabat $T^u[z]$ with LCL $= z_b = 500$m. The moist adiabatic lapse rate transitions linearly from liquid to ice saturation between 273.15 and 253.15 K. Then, we compute $\epsilon(z)$ from Eq. 5.9 and integrate Eq. 5.7 upwards to get Δh(z). To find $\Delta T(z)$ using Eq. 5.10, we must make a first guess of $\overline{T}(z)$, which we have not yet solved for. We use $T^u(z)$ as a first guess, solve for $\Delta T(z)$ via Eq. 5.10, then recompute $\overline{T}(z) = T^u(z) + \Delta T(z)$. We then solve for $\Delta T(z)$ again using the updated $\overline{T}(z)$ and iterate until convergence. The resulting profile of $\overline{T}(z)$ is then used to compute s.

Our goal is to determine whether the RH enhancement shown in Fig. 5.9c can account for the difference in convective-region s between the low- and high-contrast phases of the cycle. We first run the SPM using inputs from the 50-day, low-contrast sample period. The input RH profile is set to the mean RH within the convective parts of the domain, and a profile of s is generated for each test value of ϵ_0. We then run the model again using the same near-surface air temperature but the RH profile from the high-contrast sample period, which allows us to compute the change in s resulting from RH enhancement within the convecting regions. Results are shown in Figure 5.9d, with each line corresponding to a different value of ϵ_0.

BIBLIOGRAPHY

Andrews, T., et al., Accounting for Changing Temperature Patterns Increases Historical Estimates of Climate Sensitivity, *Geophysical Research Letters*, *45*(16), 8490–8499, doi:10.1029/2018GL078887, _eprint: https://onlinelibrary.wiley.com/doi/pdf/10.1029/2018GL078887, 2018.

Arnold, N. P., and W. M. Putman, Nonrotating Convective Self-Aggregation in a Limited Area AGCM, *Journal of Advances in Modeling Earth Systems*, *10*(4), 1029–1046, doi:10.1002/2017MS001218, 2018.

Bao, J., and B. Stevens, The Elements of the Thermodynamic Structure of the Tropical Atmosphere, *Journal of the Meteorological Society of Japan. Ser. II*, *99*(6), 1483–1499, doi:10.2151/jmsj.2021-072, 2021.

Becker, T., and C. Hohenegger, Entrainment and Its Dependency on Environmental Conditions and Convective Organization in Convection-Permitting Simulations, *Monthly Weather Review*, *149*(2), 537–550, doi:10.1175/MWR-D-20-0229.1, 2021.

Becker, T., C. S. Bretherton, C. Hohenegger, and B. Stevens, Estimating Bulk Entrainment With Unaggregated and Aggregated Convection, *Geophysical Research Letters*, *45*(1), 455–462, doi:10.1002/2017GL076640, 2018.

Berry, E., and G. G. Mace, Cloud properties and radiative effects of the Asian summer monsoon derived from A-Train data, *Journal of Geophysical Research*, *119*(15), 9492–9508, doi:10.1002/2014JD021458, 2014.

Betts, A. K., Saturation Point Analysis of Moist Convective Overturning, *Journal of the Atmospheric Sciences*, *39*(7), 1484–1505, doi:10.1175/1520-

0469(1982)039¡1484:SPAOMC¿2.0.CO;2, publisher: American Meteorological Society Section: Journal of the Atmospheric Sciences, 1982.

Beydoun, H., and C. Hoose, Aerosol-Cloud-Precipitation Interactions in the Context of Convective Self-Aggregation, *Journal of Advances in Modeling Earth Systems*, *11*(4), 1066–1087, doi:10.1029/2018MS001523, 2019.

Beydoun, H., P. M. Caldwell, W. M. Hannah, and A. S. Donahue, Dissecting Anvil Cloud Response to Sea Surface Warming, *Geophysical Research Letters*, *48*(15), e2021GL094,049, doi:10.1029/2021GL094049, 2021.

Bjerknes, J., ATMOSPHERIC TELECONNECTIONS FROM THE EQUATORIAL PACIFIC, *Monthly Weather Review*, *97*(3), 163–172, doi:10.1175/1520-0493(1969)097¡0163:ATFTEP¿2.3.CO;2, 1969.

Bony, S., and B. Stevens, Clouds, Circulation, and Climate Sensitivity: How the interactions between clouds, greenhouse gases and aerosols affect temperature and precipitation in a changing climate, *White Paper on WCRP Grand Challenge #4*, 2012.

Bony, S., B. Stevens, D. Coppin, T. Becker, K. A. Reed, A. Voigt, and B. Medeiros, Thermodynamic control of anvil cloud amount, *Proceedings of the National Academy of Sciences*, *113*(32), 8927–8932, doi:10.1073/pnas.1601472113, 2016.

Bony, S., et al., Clouds, circulation and climate sensitivity, *Nature Geoscience*, doi:10.1038/ngeo2398, 2015.

Bretherton, C. S., and P. K. Smolarkiewicz, Gravity Waves, Compensating Subsidence and Detrainment around Cumulus Clouds, *Journal of the Atmospheric Sciences*, *46*(6), 740–759, doi:10.1175/1520-0469(1989)046¡0740:GWCSAD¿2.0.CO;2, publisher: American Meteorological Society Section: Journal of the Atmospheric Sciences, 1989.

Bretherton, C. S., P. N. Blossey, and M. Khairoutdinov, An energy-balance analysis of deep convective self-aggregation above uniform SST, *Journal of the Atmospheric Sciences*, doi: 10.1175/JAS3614.1, 2005.

Bretherton, C. S., P. N. Blossey, and M. E. Peters, Interpretation of simple and cloud-resolving simulations of moist convection–radiation interaction with a mock-Walker circulation, *Theoretical and Computational Fluid Dynamics*, *20*(5), 421–442, doi: 10.1007/s00162-006-0029-7, 2006.

Cazenave, Q., M. Ceccaldi, J. Delanoë, J. Pelon, S. Groß, and A. Heymsfield, Evolution of DARDAR-CLOUD ice cloud retrievals: New parameters and impacts on the retrieved microphysical properties, *Atmospheric Measurement Techniques*, *12*(5), 2819–2835, doi: 10.5194/amt-12-2819-2019, 2019.

Cess, R. D., and G. L. Potter, A methodology for understanding and intercomparing atmospheric climate feedback processes in general circulation models, *Journal of Geophysical Research: Atmospheres*, *93*(D7), 8305–8314, doi:10.1029/JD093iD07p08305, 1988.

Chambers, L. H., B. Lin, and D. F. Young, Examination of New CERES Data for Evidence of Tropical Iris Feedback, *Journal of Climate*, *15*(24), 3719–3726, doi:10.1175/1520-0442(2002)015¡3719:EONCDF¿2.0.CO;2, 2002.

Chen, Y.-C., and J.-Y. Yu, Modes of tropical convection and their roles in transporting moisture and moist static energy: contrast between deep and shallow convection, *Climate Dynamics*, doi:10.1007/s00382-021-05777-x, 2021.

Chen, Y.-T., and C.-M. Wu, The Role of Interactive SST in the Cloud-Resolving Simulations of Aggregated Convection, *Journal of Advances in Modeling Earth Systems*, *11*(10), 3321–3340, doi:https://doi.org/10.1029/2019MS001762, 2019.

Chen, Y.-W., T. Seiki, C. Kodama, M. Satoh, A. T. Noda, and Y. Yamada, High Cloud Responses to Global Warming Simulated by Two Different Cloud Microphysics Schemes

Implemented in the Nonhydrostatic Icosahedral Atmospheric Model (NICAM), *Journal of Climate*, *29*(16), 5949–5964, doi:10.1175/JCLI-D-15-0668.1, 2016.

Choi, Y.-S., W. Kim, S.-W. Yeh, H. Masunaga, M.-J. Kwon, H.-S. Jo, and L. Huang, Revisiting the iris effect of tropical cirrus clouds with TRMM and A-Train satellite data, *Journal of Geophysical Research: Atmospheres*, *122*(11), 5917–5931, doi:10.1002/2016JD025827, 2017.

Collins, W. D., et al., Description of the NCAR Community Atmosphere Model (CAM 3.0), *Tech. Rep. NCAR Tech. Note NCAR/TN-464+STR*, 2004.

Coppin, D., and S. Bony, Internal variability in a coupled general circulation model in radiative-convective equilibrium, *Geophysical Research Letters*, *44*(10), 5142–5149, doi: https://doi.org/10.1002/2017GL073658, 2017.

Coppin, D., and S. Bony, On the Interplay Between Convective Aggregation, Surface Temperature Gradients, and Climate Sensitivity, *Journal of Advances in Modeling Earth Systems*, *10*(12), 3123–3138, doi:10.1029/2018MS001406, _eprint: https://onlinelibrary.wiley.com/doi/pdf/10.1029/2018MS001406, 2018.

Cronin, T. W., and A. A. Wing, Clouds, Circulation, and Climate Sensitivity in a Radiative-Convective Equilibrium Channel Model, *Journal of Advances in Modeling Earth Systems*, *9*(8), 2883–2905, doi:10.1002/2017MS001111, _eprint: https://onlinelibrary.wiley.com/doi/pdf/10.1002/2017MS001111, 2017.

Delanoë, J., and R. J. Hogan, Combined CloudSat-CALIPSO-MODIS retrievals of the properties of ice clouds, *Journal of Geophysical Research: Atmospheres*, *115*(D4), doi: 10.1029/2009JD012346, 2010.

Deng, M., G. G. Mace, Z. Wang, and H. Okamoto, Tropical Composition, Cloud and Climate Coupling Experiment validation for cirrus cloud profiling retrieval using CloudSat

radar and CALIPSO lidar, *Journal of Geophysical Research: Atmospheres*, *115*(D10), doi:10.1029/2009JD013104, 2010.

Deser, C., M. A. Alexander, S.-P. Xie, and A. S. Phillips, Sea Surface Temperature Variability: Patterns and Mechanisms, *Annual Review of Marine Science*, *2*(Volume 2, 2010), 115–143, doi:10.1146/annurev-marine-120408-151453, 2010.

Dobbie, S., and P. Jonas, Radiative influences on the structure and lifetime of cirrus clouds, *Quarterly Journal of the Royal Meteorological Society*, *127*(578), 2663–2682, doi:10.1002/qj.49712757808, publisher: Wiley, 2001.

Dong, Y., C. Proistosescu, K. C. Armour, and D. S. Battisti, Attributing Historical and Future Evolution of Radiative Feedbacks to Regional Warming Patterns using a Green's Function Approach: The Preeminence of the Western Pacific, *Journal of Climate*, *32*(17), 5471–5491, doi:10.1175/JCLI-D-18-0843.1, publisher: American Meteorological Society Section: Journal of Climate, 2019.

Drotos, G., T. Becker, T. Mauritsen, and B. Stevens, Global variability in radiative-convective equilibrium with a slab ocean under a wide range of CO2 concentrations, *Tellus A: Dynamic Meteorology and Oceanography*, *72*(1), 1–19, doi:10.1080/16000870.2019.1699387, publisher: Taylor & Francis _eprint: https://doi.org/10.1080/16000870.2019.1699387, 2020.

Dygert, B. D., and D. L. Hartmann, The Cycle of Large-Scale Aggregation in Tropical Radiative-Convective Equilibrium, *Journal of Geophysical Research: Atmospheres*, *128*(7), e2022JD037,302, doi:10.1029/2022JD037302, _eprint: https://onlinelibrary.wiley.com/doi/pdf/10.1029/2022JD037302, 2023.

Emanuel, K., A. A. Wing, and E. M. Vincent, Radiative-convective instability, *Journal of Advances in Modeling Earth Systems*, *6*(1), 75–90, doi:https://doi.org/10.1002/2013MS000270, 2014.

Emanuel, K. A., J. D. Neelin, and C. S. Bretherton, On large-scale circulations in convecting atmospheres, *Quarterly Journal of the Royal Meteorological Society*, *120*(519), 1111–1143, doi:https://doi.org/10.1002/qj.49712051902, 1994.

Feng, Z., S. Hagos, A. K. Rowe, C. D. Burleyson, M. N. Martini, and S. P. de Szoeke, Mechanisms of convective cloud organization by cold pools over tropical warm ocean during the AMIE/DYNAMO field campaign, *Journal of Advances in Modeling Earth Systems*, *7*(2), 357–381, doi:10.1002/2014MS000384, 2015.

Fritts, D. C., and M. J. Alexander, Gravity wave dynamics and effects in the middle atmosphere, *Reviews of Geophysics*, *41*(1), doi:10.1029/2001RG000106, _eprint: https://onlinelibrary.wiley.com/doi/pdf/10.1029/2001RG000106, 2003.

Gasparini, B., P. N. Blossey, D. L. Hartmann, G. Lin, and J. Fan, What Drives the Life Cycle of Tropical Anvil Clouds?, *Journal of Advances in Modeling Earth Systems*, *11*(8), 2586–2605, doi:10.1029/2019MS001736, 2019.

Gasparini, B., P. J. Rasch, D. L. Hartmann, C. J. Wall, and M. Dütsch, A Lagrangian Perspective on Tropical Anvil Cloud Lifecycle in Present and Future Climate, *Journal of Geophysical Research: Atmospheres*, *126*(4), e2020JD033,487, doi:https://doi.org/10.1029/2020JD033487, 2021.

Gasparini, B., S. C. Sullivan, A. B. Sokol, B. Kärcher, E. Jensen, and D. L. Hartmann, Opinion: Tropical cirrus – from micro-scale processes to climate-scale impacts, *Atmospheric Chemistry and Physics*, *23*(24), 15,413–15,444, doi:10.5194/acp-23-15413-2023, 2023.

Grabowski, W. W., J.-I. Yano, and M. W. Moncrieff, Cloud Resolving Modeling of Tropical Circulations Driven by Large-Scale SST Gradients, *Journal of the Atmospheric Sciences*, *57*(13), 2022–2040, doi:10.1175/1520-0469(2000)057¡2022:CRMOTC¿2.0.CO;2, 2000.

Harrop, B. E., and D. L. Hartmann, Testing the role of radiation in determining tropical cloud-top temperature, *Journal of Climate*, doi:10.1175/JCLI-D-11-00445.1, 2012.

Hartmann, D. L., Tropical anvil clouds and climate sensitivity, *Proceedings of the National Academy of Sciences*, *113*(32), 8897–8899, doi:10.1073/pnas.1610455113, 2016.

Hartmann, D. L., and S. E. Berry, The balanced radiative effect of tropical anvil clouds, *Journal of Geophysical Research*, *122*(9), 5003–5020, doi:10.1002/2017JD026460, 2017.

Hartmann, D. L., and B. D. Dygert, Global Radiative Convective Equilibrium With a Slab Ocean: SST Contrast, Sensitivity and Circulation, *Journal of Geophysical Research: Atmospheres*, *127*(12), e2021JD036,400, doi:10.1029/2021JD036400, _eprint: https://onlinelibrary.wiley.com/doi/pdf/10.1029/2021JD036400, 2022.

Hartmann, D. L., and K. Larson, An important constraint on tropical cloud - climate feedback, *Geophysical Research Letters*, *29*(20), 12–1–12–4, doi: https://doi.org/10.1029/2002GL015835, 2002.

Hartmann, D. L., and M. L. Michelsen, No evidence for Iris, *Bulletin of the American Meteorological Society*, *83*(2), 249–254, doi:10.1175/1520-0477(2002)083¡0249:NEFI¿2.3.CO;2, 2002.

Hartmann, D. L., L. A. Moy, and Q. Fu, Tropical Convection and the Energy Balance at the Top of the Atmosphere, *Journal of Climate*, *14*(24), 4495–4511, doi:10.1175/1520-0442(2001)014¡4495:TCATEB¿2.0.CO;2, publisher: American Meteorological Society Section: Journal of Climate, 2001.

Hartmann, D. L., B. Gasparini, S. E. Berry, and P. N. Blossey, The Life Cycle and Net Radiative Effect of Tropical Anvil Clouds, *Journal of Advances in Modeling Earth Systems*, *10*(12), 3012–3029, doi:10.1029/2018MS001484, 2018.

Hartmann, D. L., B. D. Dygert, P. N. Blossey, Q. Fu, and A. B. Sokol, The Vertical Profile of Radiative Cooling and Lapse Rate in a Warming Climate, *Journal of Climate*, *35*(19), 2653–2665, doi:10.1175/JCLI-D-21-0861.1, publisher: American Meteorological Society Section: Journal of Climate, 2022.

Held, I. M., and B. J. Soden, Robust Responses of the Hydrological Cycle to Global Warming, *Journal of Climate*, *19*(21), 5686–5699, doi:10.1175/JCLI3990.1, publisher: American Meteorological Society Section: Journal of Climate, 2006.

Held, I. M., R. S. Hemler, and V. Ramaswamy, Radiative-Convective Equilibrium with Explicit Two-Dimensional Moist Convection, *Journal of the Atmospheric Sciences*, *50*(23), 3909–3927, doi:10.1175/1520-0469(1993)050¡3909:RCEWET¿2.0.CO;2, publisher: American Meteorological Society Section: Journal of the Atmospheric Sciences, 1993.

Hersbach, H., et al., The ERA5 global reanalysis, *Quarterly Journal of the Royal Meteorological Society*, *146*(730), 1999–2049, doi:10.1002/qj.3803, 2020.

Heymsfield, A. J., G.-J. v. Zadelhoff, D. P. Donovan, F. Fabry, R. J. Hogan, and A. J. Illingworth, Refinements to Ice Particle Mass Dimensional and Terminal Velocity Relationships for Ice Clouds. Part II: Evaluation and Parameterizations of Ensemble Ice Particle Sedimentation Velocities, *Journal of the Atmospheric Sciences*, *64*(4), 1068–1088, doi:10.1175/JAS3900.1, 2007.

Hohenegger, C., and B. Stevens, Coupled radiative convective equilibrium simulations with explicit and parameterized convection, *Journal of Advances in Modeling Earth Systems*, *8*(3), 1468–1482, doi:10.1002/2016MS000666, _eprint: https://onlinelibrary.wiley.com/doi/pdf/10.1002/2016MS000666, 2016.

Holloway, C. E., and S. J. Woolnough, The sensitivity of convective aggregation to diabatic processes in idealized radiative-convective equilibrium simulations, *Journal of Advances in Modeling Earth Systems*, *8*(1), 166–195, doi:https://doi.org/10.1002/2015MS000511, 2016.

Hong, Y., G. Liu, and J.-L. F. Li, Assessing the Radiative Effects of Global Ice Clouds Based on CloudSat and CALIPSO Measurements, *Journal of Climate*, *29*(21), 7651–7674, doi:10.1175/JCLI-D-15-0799.1, 2016.

Hu, Z., N. Jeevanjee, and Z. Kuang, From Grid to Cloud: Understanding the Impact of Grid Size on Simulated Anvil Clouds and Atmospheric Profiles, *preprint*, Preprints, doi: 10.22541/essoar.169755531.19575121/v1, 2023.

Höjgård-Olsen, E., H. Chepfer, and H. Brogniez, Satellite Observed Sensitivity of Tropical Clouds and Moisture to Sea Surface Temperature on Various Time and Space Scales: 1. Focus on High Level Cloud Situations Over Ocean, *Journal of Geophysical Research: Atmospheres*, *127*(6), e2021JD035,438, doi:10.1029/2021JD035438, 2022.

Iacono, M. J., E. J. Mlawer, S. A. Clough, and J.-J. Morcrette, Impact of an improved longwave radiation model, RRTM, on the energy budget and thermodynamic properties of the NCAR community climate model, CCM3, *Journal of Geophysical Research: Atmospheres*, *105*(D11), 14,873–14,890, doi:https://doi.org/10.1029/2000JD900091, 2000.

Igel, M. R., A. J. Drager, and S. C. van den Heever, A CloudSat cloud object partitioning technique and assessment and integration of deep convective anvil sensitivities to sea surface temperature, *Journal of Geophysical Research: Atmospheres*, *119*(17), 10,515–10,535, doi:10.1002/2014JD021717, 2014.

Ito, M., and H. Masunaga, Process-Level Assessment of the Iris Effect Over Tropical Oceans, *Geophysical Research Letters*, *49*(7), e2022GL097,997, doi:10.1029/2022GL097997, 2022.

Jakob, C., M. S. Singh, and L. Jungandreas, Radiative Convective Equilibrium and Organized Convection: An Observational Perspective, *Journal of Geophysical Research: Atmospheres*, *124*(10), doi:10.1029/2018JD030092, 2019.

Jeevanjee, N., Three Rules for the Decrease of Tropical Convection With Global Warming, *Journal of Advances in Modeling Earth Systems*, *14*(11), e2022MS003,285, doi:10.1029/2022MS003285, _eprint: https://onlinelibrary.wiley.com/doi/pdf/10.1029/2022MS003285, 2022.

Jeevanjee, N., and S. Fueglistaler, Simple spectral models for atmospheric radiative cooling, *Journal of the Atmospheric Sciences*, *77*(2), 479–497, doi:10.1175/JAS-D-18-0347.1, 2020.

Jeevanjee, N., and D. M. Romps, Convective self-aggregation, cold pools, and domain size, *Geophysical Research Letters*, *40*(5), 994–998, doi:10.1002/grl.50204, 2013.

Jeevanjee, N., and D. M. Romps, Mean precipitation change from a deepening troposphere, *Proceedings of the National Academy of Sciences of the United States of America*, *115*(45), 11,465–11,470, doi:10.1073/pnas.1720683115, 2018.

Jenney, A. M., D. A. Randall, and M. D. Branson, Understanding the Response of Tropical Ascent to Warming Using an Energy Balance Framework, *Journal of Advances in Modeling Earth Systems*, *12*(6), e2020MS002,056, doi:10.1029/2020MS002056, _eprint: https://onlinelibrary.wiley.com/doi/pdf/10.1029/2020MS002056, 2020.

Jensen, E. J., S. C. van den Heever, and L. D. Grant, The Life Cycles of Ice Crystals Detrained From the Tops of Deep Convection, *Journal of Geophysical Research: Atmospheres*, *123*(17), 9624–9634, doi:10.1029/2018JD028832, publisher: Blackwell Publishing Ltd, 2018.

Johnson, R. H., P. E. Ciesielski, and K. A. Hart, Tropical Inversions near the 0°C Level, *Journal of the Atmospheric Sciences*, *53*(13), 1838–1855, doi:10.1175/1520-0469(1996)053¡1838:TINTL¿2.0.CO;2, 1996.

Johnson, R. H., T. M. Rickenbach, S. A. Rutledge, P. E. Ciesielski, and W. H. Schubert, Trimodal Characteristics of Tropical Convection, *Journal of Climate*, *12*(8), 2397–2418, doi:10.1175/1520-0442(1999)012¡2397:TCOTC¿2.0.CO;2, 1999.

Kang, H., Y.-S. Choi, J. Hwang, and H.-S. Kim, On the cloud radiative effect for tropical high clouds overlying low clouds, *Geoscience Letters*, *7*(1), 7, doi:10.1186/s40562-020-00156-6, 2020.

Keil, P., H. Schmidt, B. Stevens, and J. Bao, Variations of Tropical Lapse Rates in Climate Models and Their Implications for Upper-Tropospheric Warming, *Journal of Climate*, *34*(24), 9747–9761, doi:10.1175/JCLI-D-21-0196.1, publisher: American Meteorological Society Section: Journal of Climate, 2021.

Khairoutdinov, M. F., and D. A. Randall, Cloud Resolving Modeling of the ARM Summer 1997 IOP: Model Formulation, Results, Uncertainties, and Sensitivities, *Journal of the Atmospheric Sciences*, *60*(4), 607–625, doi:10.1175/1520-0469(2003)060¡0607:CRMOTA¿2.0.CO;2, 2003.

Knutson, T. R., and S. Manabe, Time-Mean Response over the Tropical Pacific to Increased C02 in a Coupled Ocean-Atmosphere Model, *Journal of Climate*, *8*(9), 2181–2199, doi:10.1175/1520-0442(1995)008¡2181:TMROTT¿2.0.CO;2, 1995.

Kubar, T. L., and J. H. Jiang, Net Cloud Thinning, Low-Level Cloud Diminishment, and Hadley Circulation Weakening of Precipitating Clouds with Tropical West Pacific SST Using MISR and Other Satellite and Reanalysis Data, *Remote Sensing*, *11*(10), 1250, doi:10.3390/rs11101250, 2019.

Kubar, T. L., D. L. Hartmann, and R. Wood, Radiative and Convective Driving of Tropical High Clouds, *Journal of Climate*, *20*(22), 5510–5526, doi:10.1175/2007JCLI1628.1, 2007.

Latif, M., et al., Strengthening atmospheric circulation and trade winds slowed tropical Pacific surface warming, *Communications Earth & Environment*, *4*(1), 1–10, doi:10.1038/s43247-023-00912-4, 2023.

Lee, J.-Y., et al., Future Global Climate: Scenario-Based Projections and Near-Term Information, in *Climate Change 2021: The Physical Science Basis. Contribution of Working Group I to the Sixth Assessment Report of the Intergovernmental Panel on Climate Chang*, edited by V. Masson-Delmotte, P. Zhai, A. Pirani, S.L. Connors, C. Péan, S. Berger, N. Caud, Y. Chen, L. Goldfarb, M.I. Gomis, M. Huang, K. Leitzell, E. Lonnoy, J.B.R.

Matthews, T.K. Maycock, T. Waterfield, O. Yelekçi, R. Yu, and B. Zhou, pp. 553–672, Cambridge University Press, Cambridge, United Kingdom and New York, NY, USA, doi: 10.1017/9781009157896.006, 2021.

Li, R. L., T. Storelvmo, A. V. Fedorov, and Y.-S. Choi, A Positive Iris Feedback: Insights from Climate Simulations with Temperature-Sensitive Cloud–Rain Conversion, *Journal of Climate*, *32*(16), 5305–5324, doi:10.1175/JCLI-D-18-0845.1, publisher: American Meteorological Society, 2019.

Lilly, D. K., Cirrus outflow dynamics, *Journal of the Atmospheric Sciences*, *45*(10), 1594–1605, doi:10.1175/1520-0469(1988)045¡1594:COD¿2.0.CO;2, 1988.

Lin, B., B. A. Wielicki, L. H. Chambers, Y. Hu, and K.-M. Xu, The Iris Hypothesis: A Negative or Positive Cloud Feedback?, *Journal of Climate*, *15*(1), 3–7, doi:10.1175/1520-0442(2002)015¡0003:TIHANO¿2.0.CO;2, publisher: American Meteorological Society Section: Journal of Climate, 2002.

Lindzen, R. S., and S. Nigam, On the Role of Sea Surface Temperature Gradients in Forcing Low-Level Winds and Convergence in the Tropics, *Journal of the Atmospheric Sciences*, *44*(17), doi:10.1175/1520-0469(1987)044¡2418:otross¿2.0.co;2, 1987.

Lindzen, R. S., M. D. Chou, and A. Y. Hou, Does the Earth Have an Adaptive Infrared Iris?, *Bulletin of the American Meteorological Society*, *82*(3), doi:10.1175/1520-0477(2001)082¡0417:DTEHAA¿2.3.CO;2, 2001.

Liu, R., K.-N. Liou, H. Su, Y. Gu, B. Zhao, J. H. Jiang, and S. C. Liu, High cloud variations with surface temperature from 2002 to 2015: Contributions to atmospheric radiative cooling rate and precipitation changes, *Journal of Geophysical Research: Atmospheres*, *122*(10), 5457–5471, doi:10.1002/2016JD026303, 2017.

Lutsko, N. J., and T. W. Cronin, Increase in Precipitation Efficiency With Surface Warming

in Radiative-Convective Equilibrium, *Journal of Advances in Modeling Earth Systems*, *10*(11), 2992–3010, doi:10.1029/2018MS001482, 2018.

L'Heureux, M. L., S. Lee, and B. Lyon, Recent multidecadal strengthening of the Walker circulation across the tropical Pacific, *Nature Climate Change*, *3*(6), 571–576, doi:10.1038/nclimate1840, number: 6 Publisher: Nature Publishing Group, 2013.

Ma, J., S.-P. Xie, and Y. Kosaka, Mechanisms for Tropical Tropospheric Circulation Change in Response to Global Warming, *Journal of Climate*, *25*(8), 2979–2994, doi:10.1175/JCLI-D-11-00048.1, 2012.

Manabe, S., and R. J. Stouffer, Sensitivity of a global climate model to an increase of CO2 concentration in the atmosphere, *Journal of Geophysical Research: Oceans*, *85*(C10), 5529–5554, doi:10.1029/JC085iC10p05529, _eprint: https://onlinelibrary.wiley.com/doi/pdf/10.1029/JC085iC10p05529, 1980.

Manabe, S., and R. T. Wetherald, Thermal Equilibrium of the Atmosphere with a Given Distribution of Relative Humidity, *Journal of the Atmospheric Sciences*, *24*(3), 241–259, doi:10.1175/1520-0469(1967)024¡0241:TEOTAW¿2.0.CO;2, publisher: American Meteorological Society Section: Journal of the Atmospheric Sciences, 1967.

Mapes, B., and R. Neale, Parameterizing Convective Organization to Escape the Entrainment Dilemma, *Journal of Advances in Modeling Earth Systems*, *3*(2), doi:10.1029/2011MS000042, 2011.

Mapes, B. E., and R. A. Houze, Diabatic Divergence Profiles in Western Pacific Mesoscale Convective Systems, *Journal of the Atmospheric Sciences*, *52*(10), 1807–1828, doi:10.1175/1520-0469(1995)052¡1807:DDPIWP¿2.0.CO;2, 1995.

Mapes, B. E., and P. Zuidema, Radiative-Dynamical Consequences of Dry Tongues in the Tropical Troposphere, *Journal of the Atmospheric Sciences*, *53*(4), 620–638, doi:10.1175/1520-0469(1996)053¡0620:RDCODT¿2.0.CO;2, 1996.

Masunaga, H., and T. S. L'Ecuyer, A Mechanism of Tropical Convection Inferred from Observed Variability in the Moist Static Energy Budget, *Journal of the Atmospheric Sciences*, *71*(10), 3747–3766, doi:10.1175/JAS-D-14-0015.1, publisher: American Meteorological Society Section: Journal of the Atmospheric Sciences, 2014.

Mauritsen, T., and B. Stevens, Missing iris effect as a possible cause of muted hydrological change and high climate sensitivity in models, *Nature Geoscience*, *8*(5), 346–351, doi:10.1038/ngeo2414, number: 5 Publisher: Nature Publishing Group, 2015.

May, R., S. Arms, P. March, E. Bruning, and J. Leeman, MetPy: A Python Package for Meteorological Data, doi:10.5065/D6WW7G29, 2008.

McKim, B., S. Bony, and J.-L. Dufresne, Weak anvil cloud area feedback suggested by physical and observational constraints, *Nature Geoscience*, pp. 1–6, doi:10.1038/s41561-024-01414-4, 2024.

Mitchell, D. L., and A. J. Heymsfield, Refinements in the Treatment of Ice Particle Terminal Velocities, Highlighting Aggregates, *Journal of the Atmospheric Sciences*, *62*(5), 1637–1644, doi:10.1175/JAS3413.1, 2005.

Mitchell, D. L., P. Rasch, D. Ivanova, G. McFarquhar, and T. Nousiainen, Impact of small ice crystal assumptions on ice sedimentation rates in cirrus clouds and GCM simulations, *Geophysical Research Letters*, *35*(9), doi:https://doi.org/10.1029/2008GL033552, 2008.

Mitchell, J. F. B., and W. J. Ingram, Carbon Dioxide and Climate: Mechanisms of Changes in Cloud, *Journal of Climate*, *5*(1), 5–21, doi:10.1175/1520-0442(1992)005¡0005:CDACMO¿2.0.CO;2, publisher: American Meteorological Society Section: Journal of Climate, 1992.

Mlawer, E. J., S. J. Taubman, P. D. Brown, M. J. Iacono, and S. A. Clough, Radiative transfer for inhomogeneous atmospheres: RRTM, a validated correlated-k model for the

longwave, *Journal of Geophysical Research: Atmospheres*, *102*(D14), 16,663–16,682, doi: 10.1029/97JD00237, 1997.

Morrison, H., and J. A. Milbrandt, Parameterization of Cloud Microphysics Based on the Prediction of Bulk Ice Particle Properties. Part I: Scheme Description and Idealized Tests, *Journal of the Atmospheric Sciences*, *72*(1), 287–311, doi:10.1175/JAS-D-14-0065.1, 2015.

Morrison, H., J. A. Milbrandt, G. H. Bryan, K. Ikeda, S. A. Tessendorf, and G. Thompson, Parameterization of Cloud Microphysics Based on the Prediction of Bulk Ice Particle Properties. Part II: Case Study Comparisons with Observations and Other Schemes, *Journal of the Atmospheric Sciences*, *72*(1), 312–339, doi:10.1175/JAS-D-14-0066.1, 2015.

Muller, C., and S. Bony, What favors convective aggregation and why?, *Geophysical Research Letters*, *42*(13), 5626–5634, doi:10.1002/2015GL064260, 2015.

Muller, C. J., and I. M. Held, Detailed Investigation of the Self-Aggregation of Convection in Cloud-Resolving Simulations, *Journal of the Atmospheric Sciences*, *69*(8), 2551–2565, doi:10.1175/JAS-D-11-0257.1, 2012.

Naumann, A. K., B. Stevens, C. Hohenegger, and J. P. Mellado, A Conceptual Model of a Shallow Circulation Induced by Prescribed Low-Level Radiative Cooling, *Journal of the Atmospheric Sciences*, *74*(10), 3129–3144, doi:10.1175/JAS-D-17-0030.1, 2017.

Naumann, A. K., B. Stevens, and C. Hohenegger, A Moist Conceptual Model for the Boundary Layer Structure and Radiatively Driven Shallow Circulations in the Trades, *Journal of the Atmospheric Sciences*, *76*(5), 1289–1306, doi:10.1175/JAS-D-18-0226.1, 2019.

Nesbitt, S. W., R. Cifelli, and S. A. Rutledge, Storm Morphology and Rainfall Characteristics of TRMM Precipitation Features, *Monthly Weather Review*, *134*(10), 2702–2721, doi:10.1175/MWR3200.1, publisher: American Meteorological Society Section: Monthly Weather Review, 2006.

Nigam, S., The annual warm to cold phase transition in the eastern equatorial pacific: Diagnosis of the role of stratus cloud-top cooling, *Journal of Climate*, *10*(10), 2447–2467, doi:10.1175/1520-0442(1997)010¡2447:TAWTCP¿2.0.CO;2, 1997.

Nishant, N., S. C. Sherwood, and O. Geoffroy, Radiative driving of shallow return flows from the ITCZ, *Journal of Advances in Modeling Earth Systems*, *8*(2), 831–842, doi:10.1002/2015MS000606, 2016.

Nolan, D. S., C. Zhang, and S. H. Chen, Dynamics of the shallow meridional circulation around intertropical convergence zones, *Journal of the Atmospheric Sciences*, *64*(7), 2262–2285, doi:10.1175/JAS3964.1, 2007.

Nuijens, L., and K. Emanuel, Congestus modes in circulating equilibria of the tropical atmosphere in a two-column model, *Quarterly Journal of the Royal Meteorological Society*, *144*(717), 2676–2692, doi:10.1002/qj.3385, 2018.

Pendergrass, A. G., Changing Degree of Convective Organization as a Mechanism for Dynamic Changes in Extreme Precipitation, *Current Climate Change Reports*, *6*(2), 47–54, doi:10.1007/s40641-020-00157-9, 2020.

Pierrehumbert, R. T., Thermostats, Radiator Fins, and the Local Runaway Greenhouse, *Journal of the Atmospheric Sciences*, *52*(10), 1784–1806, doi:10.1175/1520-0469(1995)052¡1784:TRFATL¿2.0.CO;2, 1995.

Pope, K. N., C. E. Holloway, T. R. Jones, and T. H. M. Stein, Cloud-Radiation Interactions and Their Contributions to Convective Self-Aggregation, *Journal of Advances in Modeling Earth Systems*, *13*(9), e2021MS002,535, doi:10.1029/2021MS002535, 2021.

Popke, D., B. Stevens, and A. Voigt, Climate and climate change in a radiative-convective equilibrium version of ECHAM6, *Journal of Advances in Modeling Earth Systems*, *5*(1), 1–14, doi:10.1029/2012MS000191, 2013.

Posselt, D. J., S. C. v. d. Heever, and G. L. Stephens, Trimodal cloudiness and tropical stable layers in simulations of radiative convective equilibrium, *Geophysical Research Letters*, *35*(8), doi:https://doi.org/10.1029/2007GL033029, 2008.

Ramanathan, V., and W. Collins, Thermodynamic regulation of ocean warming by cirrus clouds deduced from observations of the 1987 El Niño, *Nature*, *351*(6321), 27–32, doi:10.1038/351027a0, number: 6321 Publisher: Nature Publishing Group, 1991.

Ramanathan, V., R. D. Cess, E. F. Harrison, P. Minnis, B. R. Barkstrom, E. Ahmad, and D. Hartmann, Cloud-radiative forcing and climate: Results from the earth radiation budget experiment, *Science*, *243*(4887), 57–63, doi:10.1126/science.243.4887.57, 1989.

Ramaswamy, V., and J. T. Kiehl, Sensitivities of the radiative forcing due to large loadings of smoke and dust aerosols, *Journal of Geophysical Research: Atmospheres*, *90*(D3), 5597–5613, doi:10.1029/JD090iD03p05597, _eprint: https://onlinelibrary.wiley.com/doi/pdf/10.1029/JD090iD03p05597, 1985.

Reed, K. A., B. Medeiros, J. T. Bacmeister, and P. H. Lauritzen, Global Radiative–Convective Equilibrium in the Community Atmosphere Model, Version 5, *Journal of the Atmospheric Sciences*, *72*(5), 2183–2197, doi:10.1175/JAS-D-14-0268.1, 2015.

Roe, G. H., and M. B. Baker, Why Is Climate Sensitivity So Unpredictable?, *Science*, *318*(5850), 629–632, doi:10.1126/science.1144735, publisher: American Association for the Advancement of Science, 2007.

Romps, D. M., Response of tropical precipitation to global warming, *Journal of the Atmospheric Sciences*, *68*(1), 123–138, doi:10.1175/2010JAS3542.1, publisher: American Meteorological Society, 2011.

Romps, D. M., Clausius–Clapeyron Scaling of CAPE from Analytical Solutions to RCE, *Journal of the Atmospheric Sciences*, *73*(9), 3719–3737, doi:10.1175/JAS-D-15-0327.1,

publisher: American Meteorological Society Section: Journal of the Atmospheric Sciences, 2016.

Saint-Lu, M., S. Bony, and J.-L. Dufresne, Observational Evidence for a Stability Iris Effect in the Tropics, *Geophysical Research Letters*, *47*(14), doi:10.1029/2020GL089059, 2020.

Saint-Lu, M., S. Bony, and J.-L. Dufresne, Clear-sky control of anvils in response to increased CO2 or surface warming or volcanic eruptions, *npj Climate and Atmospheric Science*, *5*(1), 1–8, doi:10.1038/s41612-022-00304-z, 2022.

Sanderson, B. M., C. Piani, W. J. Ingram, D. A. Stone, and M. R. Allen, Towards constraining climate sensitivity by linear analysis of feedback patterns in thousands of perturbed-physics GCM simulations, *Climate Dynamics*, *30*(2), 175–190, doi:10.1007/s00382-007-0280-7, 2008.

Schmidt, C. T., and T. J. Garrett, A Simple Framework for the Dynamic Response of Cirrus Clouds to Local Diabatic Radiative Heating, *Journal of the Atmospheric Sciences*, *70*(5), 1409–1422, doi:10.1175/JAS-D-12-056.1, 2013.

Schulz, H., and B. Stevens, Observing the tropical atmosphere in moisture space, *Journal of the Atmospheric Sciences*, *75*(10), 3313–3330, doi:10.1175/JAS-D-17-0375.1, 2018.

Seeley, J. T., N. Jeevanjee, and D. M. Romps, FAT or FiTT: Are Anvil Clouds or the Tropopause Temperature Invariant?, *Geophysical Research Letters*, *46*(3), 1842–1850, doi:https://doi.org/10.1029/2018GL080096, _eprint: https://agupubs.onlinelibrary.wiley.com/doi/pdf/10.1029/2018GL080096, 2019.

Seidel, S. D., and D. Yang, Temperatures of Anvil Clouds and Radiative Tropopause in a Wide Array of Cloud-Resolving Simulations, *Journal of Climate*, *35*(24), 4465–4478, doi:10.1175/JCLI-D-21-0962.1, publisher: American Meteorological Society Section: Journal of Climate, 2022.

Shamekh, S., C. Muller, J.-P. Duvel, and F. D'Andrea, How Do Ocean Warm Anomalies Favor the Aggregation of Deep Convective Clouds?, *Journal of the Atmospheric Sciences*, *77*(11), 3733–3745, doi:10.1175/JAS-D-18-0369.1, 2020.

Sherwood, S. C., et al., An Assessment of Earth's Climate Sensitivity Using Multiple Lines of Evidence, *Reviews of Geophysics*, *58*(4), doi:10.1029/2019RG000678, 2020.

Singh, M. S., and P. A. O'Gorman, Influence of entrainment on the thermal stratification in simulations of radiative-convective equilibrium, *Geophysical Research Letters*, *40*(16), 4398–4403, doi:https://doi.org/10.1002/grl.50796, 2013.

Singh, M. S., and P. A. O'Gorman, Increases in moist-convective updraught velocities with warming in radiative-convective equilibrium, *Quarterly Journal of the Royal Meteorological Society*, *141*(692), 2828–2838, doi:10.1002/qj.2567, _eprint: https://onlinelibrary.wiley.com/doi/pdf/10.1002/qj.2567, 2015.

Singh, M. S., Z. Kuang, E. D. Maloney, W. M. Hannah, and B. O. Wolding, Increasing potential for intense tropical and subtropical thunderstorms under global warming, *Proceedings of the National Academy of Sciences*, *114*(44), 11,657–11,662, doi:10.1073/pnas.1707603114, 2017.

Sobel, A. H., J. Nilsson, and L. M. Polvani, The Weak Temperature Gradient Approximation and Balanced Tropical Moisture Waves, *Journal of the Atmospheric Sciences*, *58*(23), 3650–3665, doi:10.1175/1520-0469(2001)058¡3650:TWTGAA¿2.0.CO;2, 2001.

Soden, B. J., A. J. Broccoli, and R. S. Hemler, On the Use of Cloud Forcing to Estimate Cloud Feedback, *Journal of Climate*, *17*(19), 3661–3665, doi:10.1175/1520-0442(2004)017¡3661:OTUOCF¿2.0.CO;2, publisher: American Meteorological Society Section: Journal of Climate, 2004.

Sohn, B.-J., S. Lee, E.-S. Chung, and H.-J. Song, The Role of the Dry Static Stability for the

Recent Change in the Pacific Walker Circulation, *Journal of Climate*, *29*(8), 2765–2779, doi:10.1175/JCLI-D-15-0374.1, 2016.

Sokol, A. B., and D. L. Hartmann, Tropical Anvil Clouds: Radiative Driving Toward a Preferred State, *Journal of Geophysical Research: Atmospheres*, *125*(21), e2020JD033,107, doi:https://doi.org/10.1029/2020JD033107, 2020.

Sokol, A. B., and D. L. Hartmann, Congestus Mode Invigoration by Convective Aggregation in Simulations of Radiative-Convective Equilibrium, *Journal of Advances in Modeling Earth Systems*, *14*(7), doi:10.1029/2022MS003045, 2022.

Stauffer, C. L., and A. A. Wing, Properties, Changes, and Controls of Deep-Convecting Clouds in Radiative-Convective Equilibrium, *Journal of Advances in Modeling Earth Systems*, *14*(6), e2021MS002,917, doi:10.1029/2021MS002917, _eprint: https://onlinelibrary.wiley.com/doi/pdf/10.1029/2021MS002917, 2022.

Stephens, G., D. Winker, J. Pelon, C. Trepte, D. Vane, C. Yuhas, T. L'Ecuyer, and M. Lebsock, CloudSat and CALIPSO within the A-Train: Ten Years of Actively Observing the Earth System, *Bulletin of the American Meteorological Society*, *99*(3), 569–581, doi:10.1175/BAMS-D-16-0324.1, 2018.

Stephens, G. L., et al., The cloudsat mission and the A-Train: A new dimension of space-based observations of clouds and precipitation, *Bulletin of the American Meteorological Society*, *83*(12), 1771–1790+1742, doi:10.1175/BAMS-83-12-1771, 2002.

Stubenrauch, C. J., G. Caria, S. E. Protopapadaki, and F. Hemmer, 3D radiative heating of tropical upper tropospheric cloud systems derived from synergistic A-Train observations and machine learning, *Atmospheric Chemistry and Physics*, *21*(2), 1015–1034, doi:10.5194/acp-21-1015-2021, 2021.

Su, H., et al., Variations of tropical upper tropospheric clouds with sea surface tempera-

ture and implications for radiative effects, *Journal of Geophysical Research: Atmospheres*, *113*(D10), doi:10.1029/2007JD009624, 2008.

Tompkins, A. M., and A. G. Semie, Impact of a Mixed Ocean Layer and the Diurnal Cycle on Convective Aggregation, *Journal of Advances in Modeling Earth Systems*, *13*(12), e2020MS002,186, doi:10.1029/2020MS002186, 2021.

Trenberth, K. E., D. P. Stepaniak, and J. M. Caron, The Global Monsoon as Seen through the Divergent Atmospheric Circulation, *Journal of Climate*, *13*(22), 3969–3993, doi:10.1175/1520-0442(2000)013¡3969:TGMAST¿2.0.CO;2, 2000.

Vecchi, G. A., and B. J. Soden, Global Warming and the Weakening of the Tropical Circulation, *Journal of Climate*, *20*(17), 4316–4340, doi:10.1175/JCLI4258.1, publisher: American Meteorological Society Section: Journal of Climate, 2007.

Voigt, A., N. Albern, and G. Papavasileiou, The Atmospheric Pathway of the Cloud-Radiative Impact on the Circulation Response to Global Warming: Important and Uncertain, *Journal of Climate*, *32*(10), 3051–3067, doi:10.1175/JCLI-D-18-0810.1, publisher: American Meteorological Society Section: Journal of Climate, 2019.

Voigt, A., N. Albern, P. Ceppi, K. Grise, Y. Li, and B. Medeiros, Clouds, radiation, and atmospheric circulation in the present-day climate and under climate change, *WIREs Climate Change*, *12*(2), e694, doi:10.1002/wcc.694, _eprint: https://wires.onlinelibrary.wiley.com/doi/pdf/10.1002/wcc.694, 2021.

Wall, C. J., J. R. Norris, B. Gasparini, W. L. Smith, M. M. Thieman, and O. Sourdeval, Observational Evidence that Radiative Heating Modifies the Life Cycle of Tropical Anvil Clouds, *Journal of Climate*, *33*(20), 8621–8640, doi:10.1175/JCLI-D-20-0204.1, 2020.

Williams, I. N., and R. T. Pierrehumbert, Observational evidence against strongly stabilizing tropical cloud feedbacks, *Geophysical Research Letters*, *44*(3), 1503–1510, doi:10.1002/2016GL072202, 2017.

Wills, R. C. J., Y. Dong, C. Proistosecu, K. C. Armour, and D. S. Battisti, Systematic Climate Model Biases in the Large-Scale Patterns of Recent Sea-Surface Temperature and Sea-Level Pressure Change, *Geophysical Research Letters*, *49*(17), e2022GL100,011, doi:10.1029/2022GL100011, 2022.

Wing, A. A., and T. W. Cronin, Self-aggregation of convection in long channel geometry, *Quarterly Journal of the Royal Meteorological Society*, doi:10.1002/qj.2628, 2016.

Wing, A. A., and M. S. Singh, Control of Stability and Relative Humidity in the Radiative-Convective Equilibrium Model Intercomparison Project, *Journal of Advances in Modeling Earth Systems*, *16*(1), e2023MS003,914, doi:10.1029/2023MS003914, _eprint: https://onlinelibrary.wiley.com/doi/pdf/10.1029/2023MS003914, 2024.

Wing, A. A., K. Emanuel, C. E. Holloway, and C. Muller, Convective Self-Aggregation in Numerical Simulations: A Review, *Surveys in Geophysics*, *38*(6), 1173–1197, doi: https://doi.org/10.1007/s1071201794084, 2017.

Wing, A. A., K. A. Reed, M. Satoh, B. Stevens, S. Bony, and T. Ohno, Radiative–convective equilibrium model intercomparison project, *Geoscientific Model Development*, *11*(2), 793–813, doi:10.5194/gmd-11-793-2018, 2018.

Wing, A. A., et al., Clouds and Convective Self-Aggregation in a Multi-Model Ensemble of Radiative-Convective Equilibrium Simulations, *Journal of Advances in Modeling Earth Systems*, doi:10.1029/2020MS002138, 2020.

Winker, D. M., M. A. Vaughan, A. Omar, Y. Hu, K. A. Powell, Z. Liu, W. H. Hunt, and S. A. Young, Overview of the CALIPSO Mission and CALIOP Data Processing Algorithms, *Journal of Atmospheric and Oceanic Technology*, *26*(11), 2310–2323, doi: 10.1175/2009JTECHA1281.1, 2009.

Wu, Z., A Shallow CISK, Deep Equilibrium Mechanism for the Interaction between Large-Scale Convection and Large-Scale Circulations in the Tropics, *Journal of the Atmospheric*

Sciences, *60*(2), 377–392, doi:10.1175/1520-0469(2003)060¡0377:ASCDEM¿2.0.CO;2, 2003.

Xu, K.-M., and K. A. Emanuel, Is the Tropical Atmosphere Conditionally Unstable?, *Monthly Weather Review*, *117*(7), 1471–1479, doi:10.1175/1520-0493(1989)117¡1471:ITTACU¿2.0.CO;2, publisher: American Meteorological Society Section: Monthly Weather Review, 1989.

Yano, J.-I., M. W. Moncrieff, and W. W. Grabowski, Walker-Type Mean Circulations and Convectively Coupled Tropical Waves as an Interacting System, *Journal of the Atmospheric Sciences*, *59*(9), 1566–1577, doi:10.1175/1520-0469(2002)059¡1566:WTMCAC¿2.0.CO;2, 2002.

Yao, L., and D. Yang, Convective Self-Aggregation Occurs Without Radiative Feedbacks in Warm Climates, *Geophysical Research Letters*, *50*(16), e2023GL104,624, doi:10.1029/2023GL104624, _eprint: https://onlinelibrary.wiley.com/doi/pdf/10.1029/2023GL104624, 2023.

Yasunaga, K., K. Yoneyama, H. Kubota, H. Okamoto, A. Shimizu, H. Kumagai, M. Katsumata, N. Sugimoto, and I. Matsui, Melting Layer Cloud Observed during R/V Mirai Cruise MR01-K05, *Journal of the Atmospheric Sciences*, *63*(11), 3020–3032, doi:10.1175/JAS3779.1, 2006.

Zelinka, M. D., and D. L. Hartmann, Why is longwave cloud feedback positive?, *Journal of Geophysical Research Atmospheres*, *115*(16), doi:10.1029/2010JD013817, 2010.

Zelinka, M. D., and D. L. Hartmann, The observed sensitivity of high clouds to mean surface temperature anomalies in the tropics, *Journal of Geophysical Research: Atmospheres*, *116*(D23), doi:10.1029/2011JD016459, 2011.

Zelinka, M. D., S. A. Klein, and D. L. Hartmann, Computing and Partitioning Cloud Feedbacks Using Cloud Property Histograms. Part II: Attribution to Changes in Cloud Amount,

Altitude, and Optical Depth, *Journal of Climate*, *25*(11), 3736–3754, doi:10.1175/JCLI-D-11-00249.1, 2012.

Zelinka, M. D., D. A. Randall, M. J. Webb, and S. A. Klein, Clearing clouds of uncertainty, *Nature Climate Change*, *7*(10), 674–678, doi:10.1038/nclimate3402, 2017.

Zhang, C., M. McGauley, and N. A. Bond, Shallow meridional circulation in the tropical eastern Pacific, *Journal of Climate*, *17*(1), 133–139, doi:10.1175/1520-0442(2004)017¡0133:SMCITT¿2.0.CO;2, 2004.

Zhang, C., D. S. Nolan, C. D. Thorncroft, and H. Nguyen, Shallow Meridional Circulations in the Tropical Atmosphere, *Journal of Climate*, *21*(14), 3453–3470, doi:10.1175/2007JCLI1870.1, 2008.

Zhou, C., M. D. Zelinka, and S. A. Klein, Impact of decadal cloud variations on the Earth's energy budget, *Nature Geoscience*, *9*(12), 871–874, doi:10.1038/ngeo2828, number: 12 Publisher: Nature Publishing Group, 2016.

Zhou, W., and S.-P. Xie, A Conceptual Spectral Plume Model for Understanding Tropical Temperature Profile and Convective Updraft Velocities, *Journal of the Atmospheric Sciences*, *76*(9), 2801–2814, doi:10.1175/JAS-D-18-0330.1, 2019.

Zuidema, P., B. Mapes, J. Lin, C. Fairall, and G. Wick, The Interaction of Clouds and Dry Air in the Eastern Tropical Pacific, *Journal of Climate*, *19*(18), 4531–4544, doi:10.1175/JCLI3836.1, 2006.